POLITECNICO DI TORINO

Master Thesis In Biomedical Engineering

Hydraulic Losses In Fontan Procedure For The Treatment Of The Univentricular Heart In Infants. A Numeric Study.

Master Student:
Roberta Giunta

Supervisor:
Prof. Diego Gallo
Prof. Umberto Morbiducci
Prof. Luca Ridolfi
Prof.ssa Stefania Scarsoglio

ACADEMIC YEAR 2015-2016

A Joy,
al primo istante in cui
l'ho tenuta in braccio
e nell'aria c'era il profumo
della felicità.

ABSTRACT

This master thesis work is focused on a Computational Fluid Dynamic analysis of the TECPC (extracardiac total cavopulmonary connection) model for the treatment of the single ventricle heart defect which is important to evaluate blood patterns during surgery yet also the hydraulic losses that help us determinating the hemodynamic influence on the outcome of the operation. The geometrical model, with particularly characteristics, was created with the software SolidWorks. To realise this model, that presents two sections of inlet (the superior and inferior venas cava) and two sections of outlet (the right and left pulmonary artery), a flow rate distribution of 60/40 was assumed at the entrance of the model for a total flow rate of 3 *L/min*. Furthermore, the length of the vessel permits to have a model in which the flow is fully developed. After the construction of the model, a sensitivity analysis was performed to find which spatial resolution is needed in this case of study in order to have results that are independent from the number of elements of the mesh. Seven meshes were created with ICEM (ANSYS), each one with a radial spatial gradient for the element size to properly resolve the higher velocity gradients near the wall. The sensitivity analysis was based on steady simulations using FLUENT (ANSYS). Blood fluid was assumed to have a rheological Newtonian behaviour, with typical values for density and viscosity of a hematocrit of 43%. The velocity magnitude was set for the inlets and an outflow, with a flow rate weight 0,5, for both outlets as boundary conditions, and at the end, no-slip condition and the rigid behaviour for the wall were set. Second order Navier-Stokes equations and the continuity equation were solved. The results were analyzed through the comparison, between the seven tested meshes, of both the average and the maximum values of a field variable, the velocity magnitude, and of an hemodynamic variable, the WSS, in the areas of interest. Also, the meshes were tested on the hydraulic performance. It was found

that the necessary grid size for this hemodynamic application was of the order of $3 \cdot 10^6$ elements, because it allows to achieve the right balance between *accuracy solution*, *computational costs* and *hydraulic losses*. Then the fluid domain was studied under unsteady flow conditions, using a time dependent flow rate profile for the inlet boundary condition: an inflow velocity. Four transient cycles were performed and, at the end of each cycle, WSS and velocity magnitude were evaluated to establish whether a sufficient accuracy was reached by calculating their percentage or not. After these cycles, data were collected and post-processed. The data were subjected to both an Eulerian and Lagrangian analysis to evaluate the interaction of the blood flow with the arterial wall and the forces acting on it in this new vessel conformation. The Lagrangian analysis was developed to evaluate how intravascular flow features within the graft could unfavourably affect shear induced activation of platelets, which promote thrombus formation. The Eulerian analysis was developed to identify regions of low wall shear stress, corresponding to a low/stagnating flow, which plays a primary role in thrombus formation. Also, the hydraulic losses were evaluated in a new steady simulation (that has the same flow rate as the boundary condition of the unsteady model) and in the unsteady simulation. The values were compared in order to evaluate the percentage of error that is made when a simplified steady model is used rather than the more physiological unsteady model.

CHAPTER 1
ANATOMY OF THE HEART, BLOOD PROPERTIES, CARDIAC DEFECTS AND AIM OF STUDY

The aim of this first chapter is to define the Single Ventricle Heart Defect (SVHD) a cardiovascular pathology that occurs in approximately 1–2% of infants, to summarize the available surgical techniques for its treatment, to report the experienced complications during the follow-up, and finally, to give some examples of some CFD studies focused on blood fluid mechanical behaviour in the geometrical model that was created for our research. This chapter is divided into four sections: the first one is a general introduction of the physiological cardiovascular system with definitions and descriptions of its components. The second paragraph describes the characteristics, the functions and the properties of the blood, giving great attention to blood rheological properties which determine the hemodynamic behaviour. The third one characterises the SVHD pathology: starting from its definition and then proceeding to its causes and associated risks. This section is focused on surgical procedures that are divided into 3 steps: the Norwood procedure, the Glenn procedure and with particular emphasis on the last procedure, the Fontan procedure. In fact the text shows the 3 variations of the Fontan procedure: the atriopulmonary connection (APA), the intracardiac later tunnel total cavopulmonary connection (TCPC) and the extracardiac total cavopulmonary connection TECPC, explaining how the *extracardiac conduit* approach has several important theoretical advantages and how it has been shown to improve hydrodynamic efficiency.

The last section shows the primary aim of this study, that is, the calculation of the energy losses in the cardiac cycle, because when the heart experiences supernormal hemodynamic pressures or volume loads, the myocardium can become hypertrophied and/or dilate. Descriptions of the source of mechanical energy in the circulation and the type of mechanical energy loss are also given.

1.1 **Heart**

The heart is a muscular organ about the size of a closed fist that functions as the body's circulatory pump. It takes in deoxygenated blood through the veins and delivers it to the lungs for oxygenation before pumping it into the various arteries (which provide oxygen and nutrients to body tissues by transporting the blood throughout the body). The heart is located in the thoracic cavity medial to the lungs and posterior to the sternum. The inferior tip of the heart, known as the apex, rests just superior to the diaphragm. The base of the heart is located along the body's midline with the apex pointing toward the left side. Because the heart points to the left, about 2/3 of the heart's mass is found on the left side of the body and the other 1/3 is on the right [**1**].

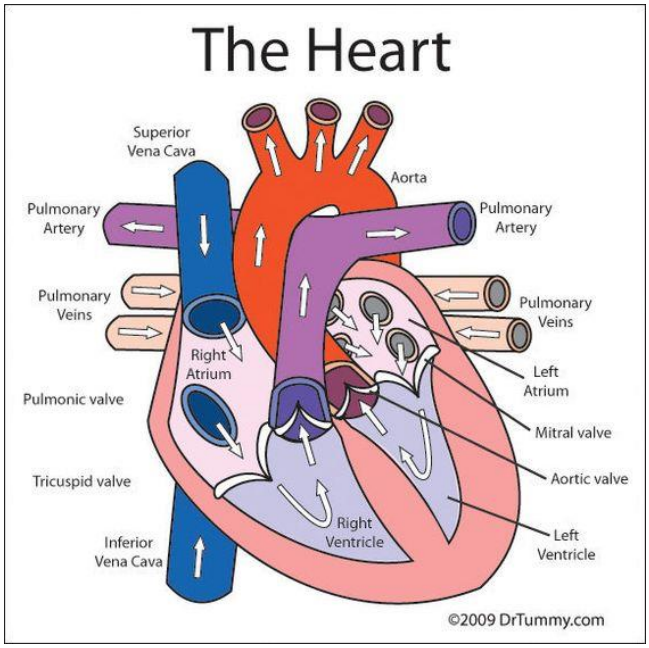

Figure 1.1 The heart

1.1.1 *Anatomy of the heart*

Pericardium

The heart sits within a fluid-filled cavity called the pericardial cavity. The walls and lining of the pericardial cavity are a special membrane known as the pericardium. Pericardium is a type of serous membrane that produces serous fluid to lubricate the heart and prevent friction between the ever beating heart and its

surrounding organs. Besides lubrication, the pericardium serves to hold the heart in position and maintain a hollow space for the heart to expand into when it is full. The pericardium has 2 layers: a visceral layer that covers the outside of the heart and a parietal layer that forms a sac around the outside of the pericardial cavity.

Structure of the Heart Wall

The heart wall is made of 3 layers: epicardium, myocardium and endocardium.

1. The epicardium is the outermost layer of the heart wall and is just another name for the visceral layer of the pericardium. Thus, the epicardium is a thin layer of serous membrane that helps to lubricate and protect the outside of the heart. Below the epicardium is the second, thicker layer of the heart wall: the myocardium.
2. The myocardium is the muscular middle layer of the heart wall that contains the cardiac muscle tissue. Myocardium makes up the majority of the thickness and mass of the heart wall and is the part of the heart responsible for pumping blood. Below the myocardium is the thin endocardium layer.
3. Endocardium is the simple squamous endothelium layer that lines the inside of the heart. The endocardium is very smooth and is responsible for keeping blood from sticking to the inside of the heart and forming potentially deadly blood clots.

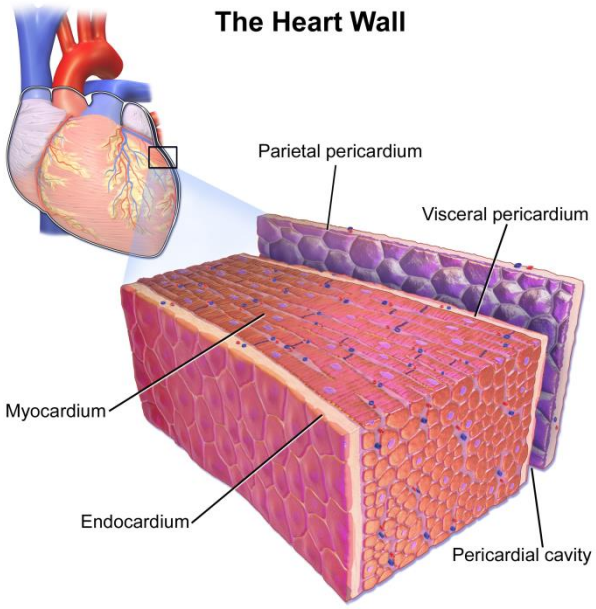

Figure 1.2 The heart wall

Chamber of the Heart

The heart contains 4 chambers: the right atrium, left atrium, right ventricle, and left ventricle. The atria are smaller than the ventricles and have thinner, less muscular walls than the ventricles. The atria act is received chambers for blood, so they are connected to the veins that carry blood to the heart. The ventricles are the larger, stronger pumping chambers that send blood out of the heart. The ventricles are connected to the arteries that carry blood away from the heart.

The chambers on the right side of the heart are smaller and have less myocardium in their heart wall when compared to the left side of the heart. This difference in size between the sides of the heart is related to their functions and the size of the 2 circulatory loops. The right side of the heart maintains pulmonary circulation to the nearby lungs while the left side of the heart pumps blood all the way to the extremities of the body in the systemic circulatory loop.

Valves of the Heart

To prevent blood from flowing backwards or "regurgitating" back into the heart, a system of one-way valves are present in the heart. The heart valves can be broken down into two types: atrioventricular and semilunar valves.

- The atrioventricular (AV) valves are located in the middle of the heart between the atria and ventricles and only allow blood to flow from the atria into the ventricles. The AV valve on the right side of the heart is called the tricuspid valve because it is made of three cusps (flaps) that separate to allow blood to pass through and connect to block regurgitation of blood. The AV valve on the left side of the heart is called the mitral valve or the bicuspid valve because it has two cusps. The AV valves are attached on the ventricular side to tough strings called chordae tendineae. The chordae tendineae pull on the AV valves to keep them from folding backwards and allowing blood to regurgitate past them.
- The semilunar valves, so named for the crescent moon shape of their cusps, are located between the ventricles and the arteries that carry blood away from the heart. The semilunar valve on the right side of the heart is the pulmonary valve, so named because it prevents the backflow of blood

from the pulmonary trunk into the right ventricle. The semilunar valve on the left side of the heart is the aortic valve, named for the fact that it prevents the aorta from regurgitating blood back into the left ventricle. The semilunar valves are smaller than the AV valves and do not have chordae tendineae to hold them in place. Instead, the cusps of the semilunar valves are cup shaped to catch regurgitating blood and use the blood's pressure to snap shut.

Conduction System of the Heart

The heart is able to both set its own rhythm and to conduct the signals necessary to maintain and coordinate this rhythm throughout its structures. About 1% of the cardiac muscle cells in the heart are responsible for forming the conduction system that sets the pace for the rest of the cardiac muscle cells.

The conduction system starts with the pacemaker of the heart a small bundle of cells known as the sinoatrial (SA) node. The SA node is located in the wall of the right atrium inferior to the superior vena cava. The SA node is responsible for setting the pace of the heart as a whole and directly signals the atria to contract. The signal from the SA node is picked up by another mass of conductive tissue known as the atrioventricular (AV) node.

The AV node is located in the right atrium in the inferior portion of the interatrial septum. The AV node picks up the signal sent by the SA node and transmits it through the atrioventricular (AV) bundle. The AV bundle is a strand of conductive tissue that runs through the interatrial septum and into the interventricular septum. The AV bundle splits into left and right branches in the interventricular septum and continues running through the septum until they reach the apex of the heart. Branching off from the left and right bundle branches are many Purkinje fibers that carry the signal to the walls of the ventricles, stimulating the cardiac muscle cells to contract in a coordinated manner to efficiently pump blood out of the heart.

1.1.2 *Physiology of the Heart*

Coronary Systole and Diastole

At any given time the chambers of the heart may found in one of two states: systole and diastole. During systole, cardiac muscle tissue is contracting to push blood out of the chamber. Whereas during diastole, the cardiac muscle cells relax to allow the chamber to fill with blood. Blood pressure increases in the major arteries during ventricular systole and decreases during ventricular diastole. This leads to the 2 numbers associated with blood pressure: systolic blood pressure is the higher number and diastolic blood pressure is the lower number. For example, a blood pressure of 120/80 describes the systolic pressure (120) and the diastolic pressure (80).

Cardiac Cycle

The cardiac cycle includes all of the events that take place during one heartbeat. There are 3 phases to the cardiac cycle: atrial systole, ventricular systole, and relaxation. During the atrial systole phase of the cardiac cycle, the atria contract and push blood into the ventricles. To facilitate this filling, the AV valves stay open and the semilunar valves stay closed to keep arterial blood from re-entering the heart. The atria are much smaller than the ventricles, so they only fill about 25% of the ventricles during this phase. The ventricles remain in diastole during this phase.

During ventricular systole, the ventricles contract to push blood into the aorta and pulmonary trunk. The pressure of the ventricles forces the semilunar valves to open and the AV valves to close. This arrangement of valves allows for blood flow from the ventricles into the arteries. The cardiac muscles of the atria repolarize and enter the state of diastole during this phase. Whereas during the relaxation phase, all 4 chambers of the heart are in diastole as blood pours into the heart from the veins. The ventricles fill to about 75% capacity during this phase and will be completely filled only after the atria enter systole. The cardiac muscle cells of the ventricles repolarize during this phase to prepare for the next round of depolarization and contraction. During this phase, the AV valves open to allow blood to flow freely into the ventricles while the semilunar valves close to prevent the regurgitation of blood from the great arteries into the ventricles.

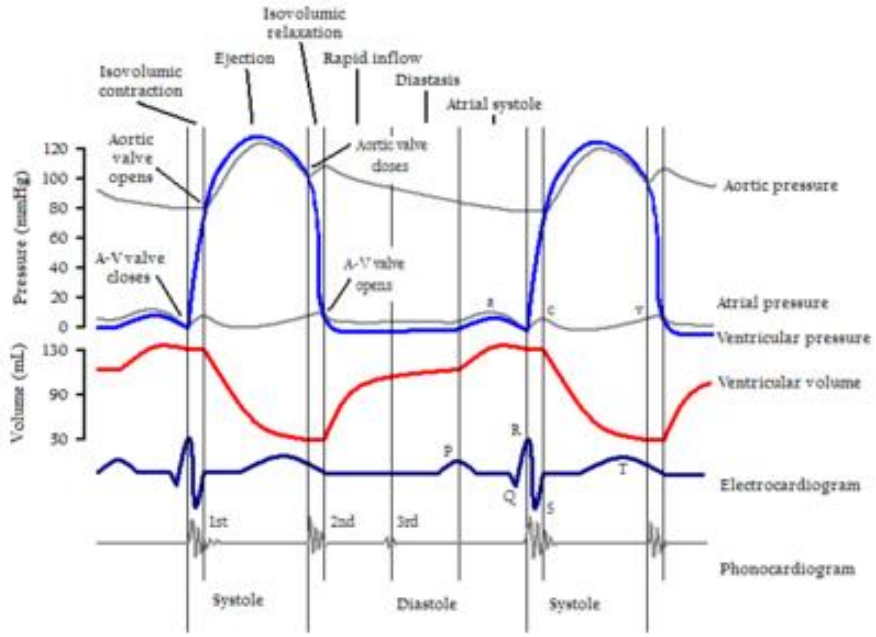

Figure 1.3 Cardiac cycle

1.1.3 *Blood Circulation*

The human circulatory system is really a two-part system whose purpose is to bring oxygen-bearing blood to all the tissues of the body. When the heart contracts it pushes the blood out into two major loops or cycles. In the systemic loop, the blood circulates into the body's systems, bringing oxygen to all its organs, structures and tissues and collecting carbon dioxide waste. In the pulmonary loop, the blood circulates to and from the lungs, to release the carbon dioxide and pick up new oxygen. The systemic cycle is controlled by the left side of the heart, the pulmonary cycle by the right side of the heart. During each cycle, the systemic loop begins when the oxygen-rich blood coming from the lungs enters the upper left chamber of the heart, the left atrium. As the chamber fills, it presses open the mitral valve and the blood flows down into the left ventricle. When the ventricles contract during a heartbeat, the blood on the left side is forced into the aorta. This largest artery of the body is an inch wide. The blood leaving the aorta brings oxygen to all the body's cells through the network of ever smaller arteries and capillaries. The used blood from the body returns to the heart through the network of veins. All of the blood from the body is eventually collected into the two largest veins: the superior vena cava, which receives blood from the upper body, and the inferior vena cava, which

receives blood from the lower body region. Both venae cavae empty the blood into the right atrium of the heart. From here the blood begins its journey through the pulmonary cycle. From the right atrium the blood descends into the right ventricle through the tricuspid valve. When the ventricle contracts, the blood is pushed into the pulmonary artery that branches into two main parts: one going to the left lung, one to the right lung. The fresh, oxygen-rich blood returns to the left atrium of the heart through the pulmonary veins. Although the circulatory system is made up of two cycles, both happen at the same time. The contraction of the heart muscle starts in the two atria, which push the blood into the ventricles. Then the walls of the ventricles squeeze together and force the blood out into the arteries: the aorta to the body and the pulmonary artery to the lungs. Afterwards, the heart muscle relaxes, allowing blood to flow in from the veins and fill the atria again. In healthy people the normal (resting) heart rate is about 72 beats per minute, but it can go much higher during strenuous exercise. Scientists have estimated that it take about 30 seconds for a given portion of the blood to complete the entire cycle: from lungs to heart to body, back to the heart and out to the lungs [**2**].

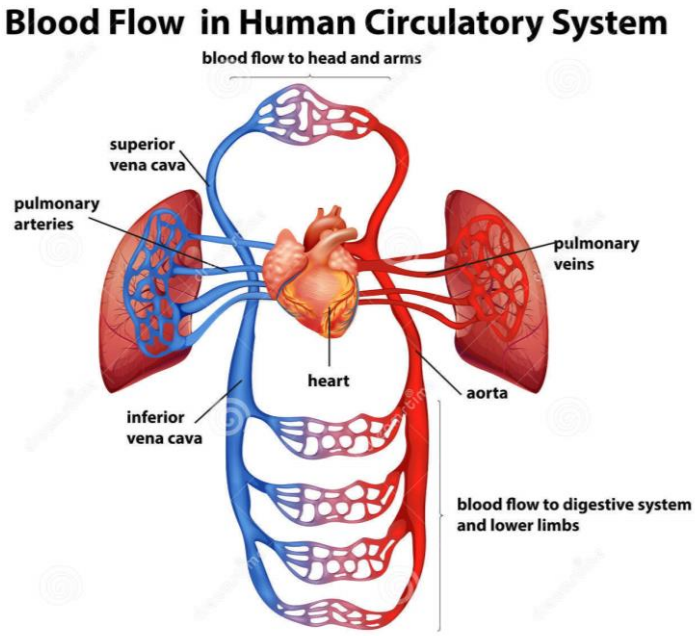

Figure 1.4 Blood Flow in Human Circulatory System

Arteries and Veins Structure

The structure of the different types of blood vessels reflects their function or layers. There are three distinct layers, or *tunics*, that form the walls of blood vessels (arteries and veins). The inner, *tunica intima* is a smooth, inner lining of endothelial cells that are in contact with the red blood cells. This tunic is continuous with the endocardium of the heart. Two further tunics surround the endothelium: the middle, *tunica media* is composed of smooth muscle, while the outer *tunica externa* is connective tissue (collagen and elastic fibres). The elastic, connective tissue stretches and supports the blood vessels, while the smooth muscle layer helps regulate blood flow by altering vascular resistance through vasoconstriction and vasodilation. The arteries have thicker smooth muscle and connective tissue than the veins to accommodate the higher pressure and speed of freshly-pumped blood. The veins are thinner walled as the pressure and rate of flow are much lower. In addition, veins are structurally different from arteries in that veins have valves to prevent the backflow of blood. Because veins have to work against gravity to get blood back to the heart, contraction of skeletal muscle assists with the flow of blood back to the heart [**3**].

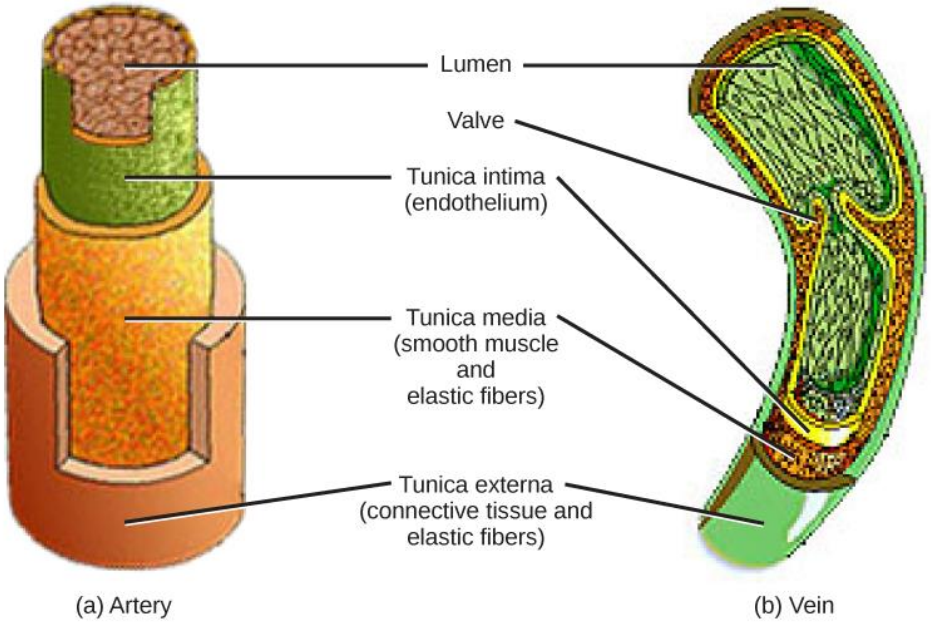

Figure 1.5 Structure of arteries and veins

1.2 **Blood**

Blood is a body fluid in humans and other animals that delivers necessary substances such as nutrients and oxygen to the cells and transports metabolic waste products away from those same cells.

In vertebrates, it is composed of blood cells suspended in blood plasma. Plasma, which constitutes 55% of blood fluid, is mostly water (92% by volume), and contains dissipated proteins, glucose, mineral ions, hormones, carbon dioxide (plasma being the main medium for excretory product transportation), and blood cells themselves. Albumin is the main protein in plasma, and it functions to regulate the colloidal osmotic pressure of blood. The blood cells are mainly *red blood cells* (also called RBCs or erythrocytes), *white blood cells* (also called WBCs or leukocytes) and *platelets* (also called thrombocytes). The most abundant cells in vertebrate blood are red blood cells. These contain hemoglobin, an iron-containing protein, which facilitates oxygen transport by reversibly binding to this respiratory gas and greatly increasing its solubility in blood. In contrast, carbon dioxide is mostly transported extracellularly as bicarbonate ion transported in plasma.

Vertebrate blood is bright red when its haemoglobin is oxygenated and dark red when it is deoxygenated. Blood is circulated around the body through blood vessels by the pumping action of the heart.

Medical terms related to blood often begin with hemo- or hemato- from the Greek word αἷμα (haima) for "blood". In terms of anatomy and histology, blood is considered a specialized form of connective tissue, given its origin in the bones and the presence of potential molecular fibres in the form of fibrinogen [**4**].

Blood has lots of important functions:

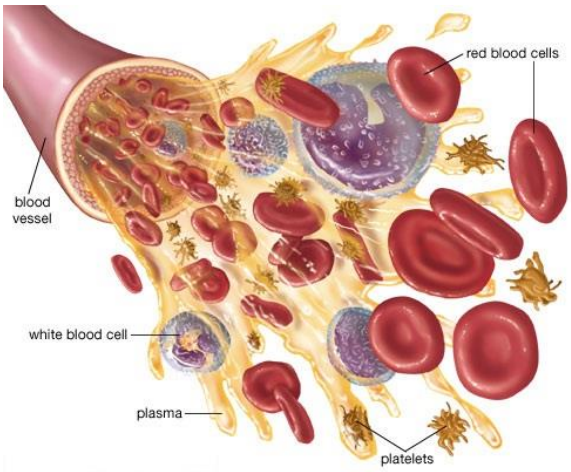

Figure 1.6 Blood components

- it brings oxygen(O2) to any tissue thanks to the haemoglobin, and it takes away the carbon dioxide (CO2), which is generated by cells;
- it vehicles some nutrients, like amino acids, sugars, mineral salts and it eliminates all the waste products of cells;
- it has an important role in the control of the bodily temperature;
- it carries some chemical substances, which are involved in the processes of cellular signalling, like growth factors, enzymes, hormones;
- it contributes to the defence of the human organism, thanks to white cells and antibodies;
- it repairs immediately any lesion, owing to the efficient coagulation process, and it promotes the self-renewal and the regeneration of the damaged (or old) tissue.

1.2.1 *Blood Rheology: Definition*

Rheology is a discipline whose purpose is to study the sliding properties of different materials: some substances have intermediate flow properties between those of solid materials and fluid materials, which are for example emulsions, suspensions and dough.

From a mechanical point of view, blood is a suspension of corpuscular elements in a saline solution, which is called plasma, but more precisely, blood is a biphasic

fluid, constituted by a fluid phase (plasma), whose most important function is to carry particles through the whole human body, and a solid phase, composed by red blood cells, platelets and white blood cells.

Blood can be approximated as an **homogeneous fluid**, so that it is characterized by two quantities: *density and viscosity*, which both are functions of the temperature, at which the fluid is kept. Nevertheless, the viscosity may also be function of the state of motion, which can be mainly defined as the set of all the velocity vectors of each element of the fluid domain, taken into account [**5**].

Blood viscosity

Viscosity is an intrinsic property of fluid related to the internal friction of adjacent fluid layers sliding past one another. This internal friction contributes to the resistance to flow. The interactions between fluid layers depend on the chemical nature of the fluid, and whether it is homogeneous or heterogeneous in composition [**6**]. It can be defined through the idealized situation known as a Couette flow, where a layer of fluid is trapped between two horizontal plates, one fixed and one moving horizontally at constant speed '*u'*. This fluid has to be homogeneous in the layer and at different shear stresses. If the speed of the top plate is small enough, the fluid particles will move parallel to it, and their speed will vary linearly from zero at the bottom to *u* at the top. Each layer of fluid will move faster than the one just below it, and friction between them will give rise to a force resisting their relative motion. In particular, the fluid will apply on the top plate a force in the direction opposite to its motion, and an equal but opposite one to the bottom plate. An external force is therefore required in order to keep the top plate moving at constant speed.

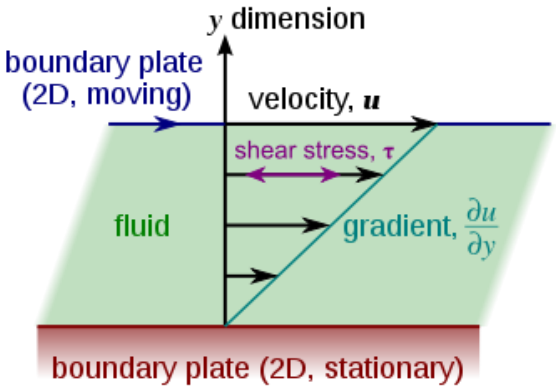

Figure 1.7 Shear stress

Isaac Newton expressed the viscous forces by the differential equation [**7**]:

$$\tau = \mu \frac{\partial u}{\partial y} \tag{1.1}$$

Where:

- $\tau = {}^{F}/_{A}$, where F is the force and A is the area of each plate,
- ${}^{\partial u}/_{\partial y}$ is the local shear velocity,
- μ is the dynamic viscosity of the fluid (proportionality factor).

This formula assumes that the flow is moving along parallel lines and the y axis, perpendicular to the flow, points in the direction of maximum shear velocity. This equation can be used where the velocity does not vary linearly with y, such as in fluid flowing through a pipe.

The unit of measurement for the viscosity is:

$$\mu = \left[\frac{Kg}{s * m}\right] = \left[\frac{N}{m^2} s\right] \tag{1.2}$$

Blood density

Density is defined as mass per unit volume. Blood density is proportional to haematocrit (*Hct*) or, more exactly, to the total protein concentration of blood. Only to a minor extent is blood density influenced by other plasma solutes [**8**].

The average value for *Hct* for an adult human being is assumed 45%, according to some experimental studies.

Therefore, the experimental expression for blood density is:

$$\rho_s = (1 - Hct)\rho_p + Hct\ \rho_{gr} \tag{1.3}$$

Where ρ_p represents plasma density and ρ_{gr} is the density of the corpuscular fraction of blood sample. This weighted average gives the relationship between the two values of density of the two main components of the blood: in normal condition it can be assumed that $\rho_p = 1035\ {}^{Kg}/_{m^3}$ and $\rho_{gr} = 1090\ {}^{Kg}/_{m^3}$, so that the value for blood density becomes equal to =1060 , which will be set in the CFD simulations in this thesis. Moreover for such application, it can be assumed that blood density is not dependent on either temperature or pressure of the blood [**9**].

1.2.2 *Rheological Newtonian model*

Blood cannot be considered as an homogeneous fluid, due to its composition made by parts with different nature. Actually blood rheology is very complex, owing to different constitutive properties of its components, like density, viscosity, size, superficial electrical charge and deformability. A fluid has a Newtonian behaviour when the shear stress depends only on the velocity gradients, through a constant, which is the dynamic viscosity, as stated in the previous paragraph.

After some experimental studies , it can be said that in vascular vessels with a diameter of nearly 0,3 mm or greater, considering blood as a Newtonian fluid would be a valid simplification, whereas in vessels with diameter smaller than 0,3 mm this hypothesis would not be acceptable anymore. This threshold is assumed according to the average size of a red blood cell, which is nearly two orders of magnitude lower

than this value, which represents the characteristic length of the vessel. As regards blood viscosity, it can be assumed that it is independent from both temperature and velocity gradients, in most part of the cases, hence blood can be considered as a Newtonian fluid. However there are some cases in which viscosity depends on more parameters: for example in vascular vessels with a diameter greater than 0,3 mm but with low values of shear rate and in vascular vessels with a diameter lower than 0,3 mm but with high values of shear rate (**10**).

1.3 **Pathology: Single Ventricle Heart Defect (SVHD)**

Congenital cardiovascular defects are the most common congenital defect, occurring in approximately 1–2% of infants.

Single ventricle heart defects, such as tricuspid atresia, is referred to cases where the heart has only one effective or functional pumping chamber, so oxygenated and deoxygenated blood are mixed in a single ventricle. Without surgical interventions this set of lesion is generally lethal, resulting in 95% mortality within the first month of life. From this complicated pathology, the concept of a total right ventricular bypass appears, first introduced by Fontan and Baudet in 1971 [**11**]. It is a palliative surgical procedure aimed at separating the systemic and pulmonary circulation thus eliminating venous blood mixing. These patients usually require a staged surgical approach culminating with a Fontan procedure.

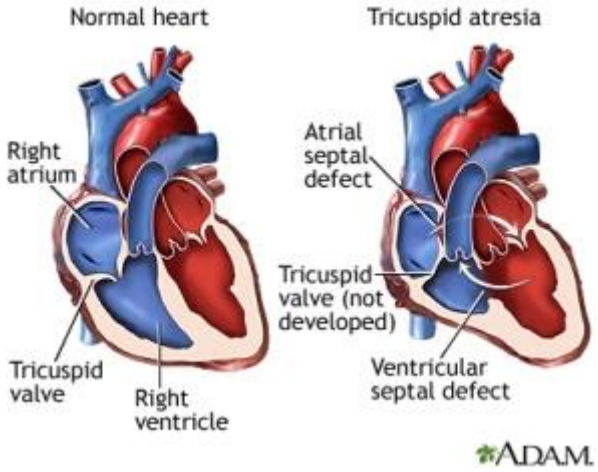

Figure 1.9 SVHD: Tricuspid atresia

1.3.1 *Surgical procedure*

The surgeries are staged such that at each stage the circulation provides adequate systemic oxygen delivery without severe, long-term volume overloading of the ventricle. The final goal is to bypass the heart by connecting the entire systemic venous return directly to the pulmonary arterial system, resulting in an series circulation driven by a single ventricle.

Stage 1 surgery is performed within the first few days of life, with the patency of the ductus arteriosus ensured by infusion of prostaglandin E2 until the operation. A systemic-topulmonary shunt by *Norwood procedure* provides balanced flow to the pulmonary circulation while maintaining an unrestricted aortic outflow and systemic venous return.

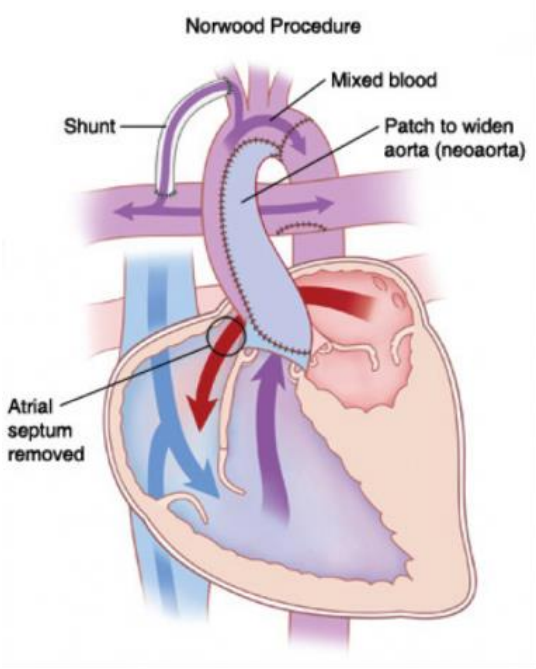

Figure 1.10 Stage 1: Norwood procedure.

Stage 2 surgery is performed at about six months of age, after the pulmonary vascular resistance has decreased due to lung growth [**12**]. The surgery removes the systemic-to-pulmonary shunt, or disconnects the pulmonary artery from the systemic arterial circulation (depending on stage 1 anatomy), and attaches the superior vena cava (SVC) to the pulmonary artery to provide pulmonary flow. This second stage is called *Bidirectional Glenn procedure* or *Hemi-Fontan* .

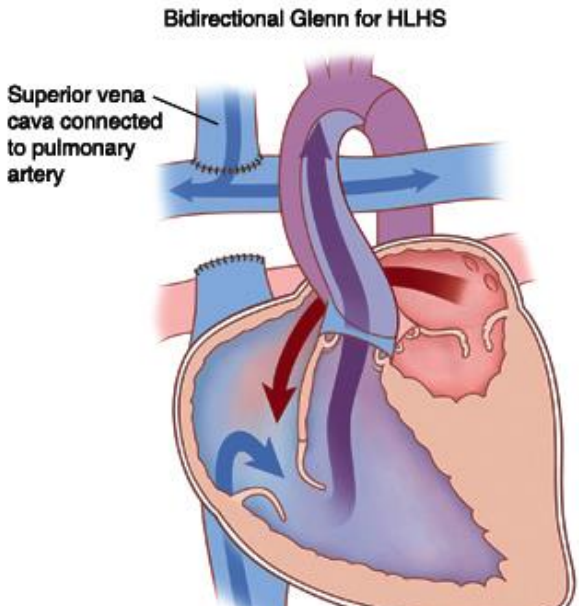

Figure 1.11 Stage 2: Bidirectional Glenn anastomoses

After a few years of age as the proportion of systemic venous return from the lower body increases.

Stage 3 surgery take place: the Fontan procedure is performed, during which the inferior vena cava (IVC) is also connected to the pulmonary artery, completing the conversion to single ventricle circulation.

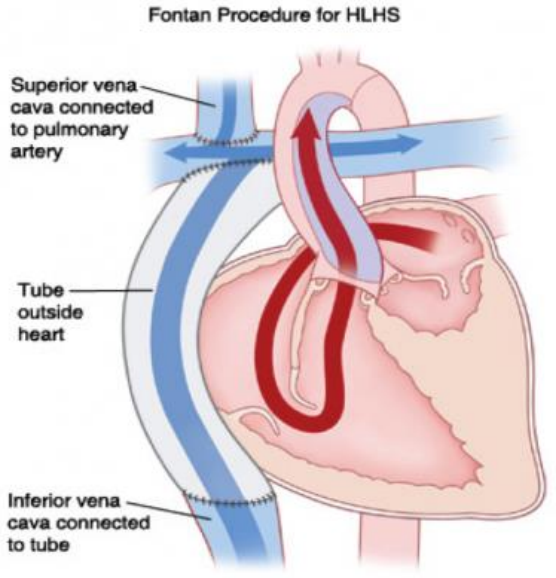

Figure 1.12 Stage 2: Fontan procedure

The transition from Stage 1 to Stage 2 circulation is particularly important as the single ventricle is relieved of the workload of providing pulmonary blood flow, which is then solely derived from the superior vena cava (SVC). In addition to requiring low pulmonary vascular resistance to allow for effective Stage 2 circulation, the surgical reconstruction required to provide a pulmonary blood flow devoid of a ventricular power source must be one that extracts little power or energy.

There are three variation of the *Fontan procedure*:

1. Atriopulmonary connection (APA)
2. Intracardiac later tunnel total cavopulmonary connection (TCPC)
3. Extracardiac total cavopulmonary connection (TECPC)

The first Fontan procedure was the atriopulmonary anastomosis (APA) technique. It is based on the principle that the right atrium only functions as a pathway rather than a pump (reason why no inferior vena cava valves were ever used), and the diastolic properties of the systemic ventricle regulate the only real "pump" of this system. The first successful total right heart bypass via atriopulmonary anastomosis (APA) were reported in 1971 for patients with tricuspid atresia [**11**]. While first fenestrated right heart by-pass was performed, with the interposition of a homograft between the right atrial appendage and the main pulmonary artery, and later, instead of placing a homograft, the APA was achieved with the patient's own pulmonary root harvested from the outflow tract of the right ventricle. These techniques were soon replaced in 1978 with the development of the direct valveless posterior APA.

In spite of the improvement in prognosis and quality of life, after the procedure of 'right atrium-right ventricle conduit' or atriopulmonary anastomosis (APA), some patients had progressive exercise intolerance, atrial arrhythmias, chronic effusions, or protein-losing enteropathy. The non-laminar venous blood flow that resulted from the postsurgical anatomy caused energy loss, as suggested by experimental studies, and it resulted in low cardiac output and development of symptoms. In addition, markedly enlarged right atria also compressed the pulmonary veins, causing elevated resistance to pulmonary blood flow [**13**].

The hemodynamic problems inherent of the APA diminished with modern surgical techniques like the lateral tunnel (LT) or the extracardiac conduit (EC).

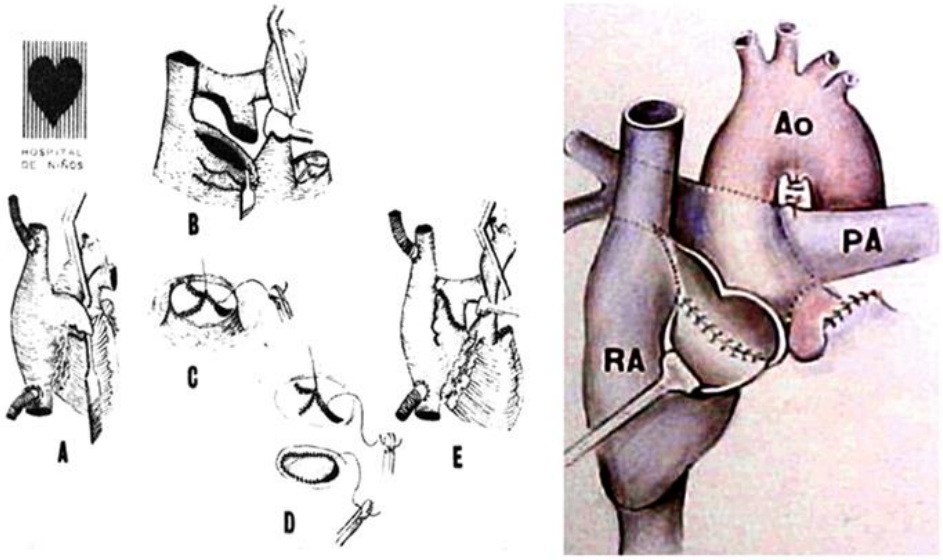

Figure 1.13 Illustrations demonstrate the steps of the technique used for the posterior APA developed in 1978 presented in London, 1980.

Leval et al. in 1988 [**14**] introduced the concept of total cavopulmonary connection. In this, a bidirectional Glenn anastomosis is performed while the inferior caval blood flow is directed towards the pulmonary arteries through an intra-atrial tunnel. The great enthusiasm for the use of this procedure was driven by the contention that elimination of the right atrial chamber would result in improved hemodynamic efficiency and might also reduce the incidence of right atrium–related complications encountered in the atriopulmonary connection (supraventricular arrhythmias and atrial thrombus formation).

Although TCPC may reduce the incidence of these complications in the early postoperative course, this issue is controversial, and moderate to late outcome remains complicated in many patients by rhythm disturbances, thrombus formation, low-output states, protein-losing enteropathy, and chronic effusions. Since some of these complications are related to extensive intra-atrial suture lines and the placement of intracardiac prosthetic material, exploration of alternative means for achieving the TCPC circulation is warranted.

Extracardiac procedures have received recent attention because they are technically simpler, do not require intra-atrial suture lines, and eliminate potentially thrombogenic intra-atrial material. Within the extracardiac approach, an epicardial tunnel or a conduit can be used to divert inferior vena cava flow to the pulmonary arteries [**15**]. The extracardiac conduit approach has several important theoretical advantages, including simplicity of offsetting superior and inferior vena cava flow streams, which has been shown to improve hydrodynamic efficiency.

The extracardiac approach was first successfully implemented by Humes and associates in a patient with complex heterotaxy. Today, it has become the procedure of choice for most single ventricle variants in many centres.

All procedures were performed through a median sternotomy with standard aortic and bicaval cannulation. For total cavo-pulmonary connection (TCPC) with an intracardiac lateral PTFE tunnel, a lateral intra-atrial channel draining the inferior vena cava (IVC) was constructed in patients. A PTFE baffle was implanted during aortic cross-clamping with cardioplegic arrest using cardiopulmonary by-pass (CPB) with moderate hypothermia. The coronary sinus was left on the “left” side of the baffle. For extracardiac total cavo-pulmonary connection (TECPC), extracardiac PTFE conduits were implanted to patients under CPB without aortic cross-clamping on a warm, beating heart [**14**].

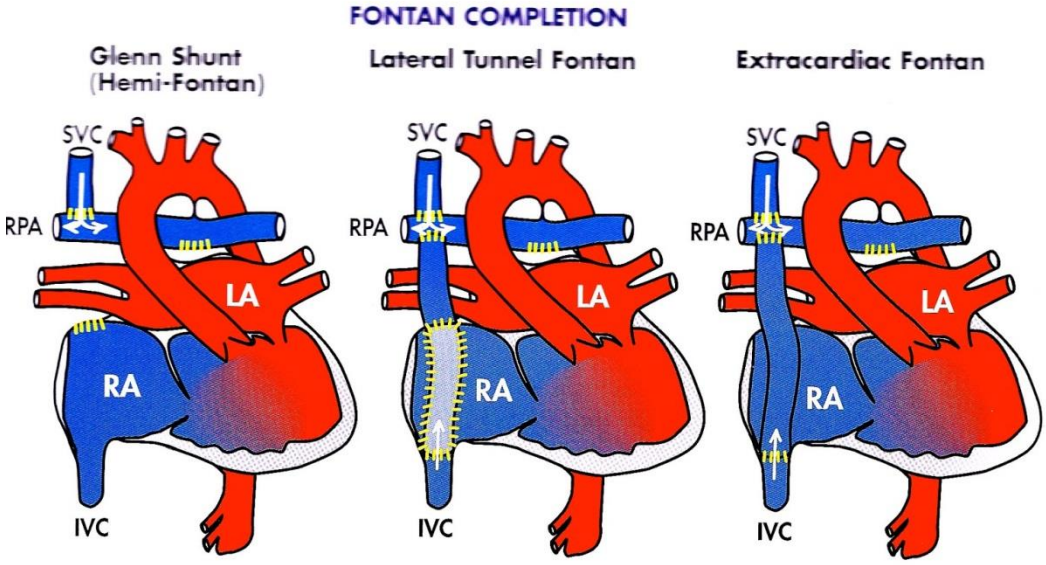

Figure 1.14 Comparison between Lateral Tunnel Fontan and Extracardiac Fontan

Clinical observations together with recent modeling, imaging, and in vitro experiments have shown that the geometry of the Fontan connection plays a key role in energy losses, hepatic flow distribution, associated strain on the cardiovascular system, and Fontan outcomes.

1.3.2 *Long-term outcome & problems*

The modifications to the original Fontan procedure, as well as improved management and care, have steadily improved surgical outcomes, reducing post-operative mortality. However, Fontan patients are still susceptible to numerous, long-term complications, such as progressive ventricular dysfunction, atrial arrhythmias, atrioventricular valve regurgitation, pulmonary arteriovenous malformations (PAVMs), diminished exercise capacity, protein losing enteropathy (PLE), somatic growth retardation, thrombotic complications, and poor neurodevelopmental outcomes [**16**], but most institutions now report 95% post-operative survival rates, the 10-year survival rate has dropped to 60–80% [**16, 17**]. The fact remains that the Fontan procedure results in a non-physiologic cardiovascular configuration where the single ventricle has to pump blood through both the systemic and pulmonary vascular beds in series. As a result, the single ventricle experiences an increased

afterload (including both systemic and pulmonary vascular resistances) and decreased preload (ventricular filling). In addition, there is a significant increase in central venous pressure due to the lack of pressure step-up typically provided by the right ventricle [**18**].

1.3.3 *Failure mechanisms*

The vascular resistance imposed by the systemic, TCPC and pulmonary circuits in series is another key component of the abnormal Fontan circulation. PLE and liver dysfunction have been correlated with the high central venous pressures observed in Fontan patients [**19**]. In absence of a right pumping chamber, the pressure difference between the IVC and the left atrium is the only force left to drive blood through the TCPC and lungs. Therefore, the higher the vascular resistance downstream of the liver, the higher the pressure difference required to achieve a given cardiac output. This observation falls back to Guyton's isolated venous theory [**20**], which states that the cardiac output in single ventricle patients is highly sensitive to the vascular resistance downstream of the venous compliance. Even though Guyton's theory focused on the effect of *pulmonary vascular resistance* (PVR), the vascular segment of interest in practice includes both the TCPC and lungs, both of which lie in series downstream of the venous compliance. Vasodilating agents have been utilized successfully to lower PVR. However, in Fontan patients all blood flow has to first travel through the TCPC, such that if the effective resistance of the connection is high, improvements in PVR alone may be insufficient to improve preload and cardiac output, especially under the increased demands of exercise or other high output states (e.g., illness, pregnancy). Even when cardiac output is not measurably affected, lowering TCPC resistance might allow for reduced medication and small but important decreases in central venous pressure such that long-term outcome and quality of life are improved.

Another major complication that results in Fontan failure and that depends on the TCPC design is progressive hypoxia due to the development of unilateral PAVMS. PAVMs are intrapulmonary shunts, connecting the pulmonary arteries directly to the pulmonary veins, thus allowing the de-oxygenated blood from the systemic circulation to return to the left atrium without flowing through the gas exchange

units. The primary consequence of PAVMS is decreased oxygen saturation. Furthermore, the intrapulmonary shunts lead to a drop in pulmonary vascular resistance, which tends to direct more flow to the diseased lung creating a positive feedback loop of increasing hypoxia. Although the underlying mechanism leading to PAVMs is unknown, studies have shown that liver derived factors present in the hepatic venous blood prevent their formation [**20**]. While it is not known what concentration of this hepatic factor is required for normal lung development, it is clear that an unbalanced hepatic flow distribution to the left and right lungs due to an inadequate design of the IVC-to-PA conduit during the 3rd stage of the TCPC surgery puts patients at risk for PAVMs. Clinically, once the extent of PAVMs is such that oxygen saturation is critically low, the only palliative option is to re-operate and re-orient the IVC conduit to achieve a better hepatic flow distribution [**21**].

1.3.4 *In vivo investigation of TCPC hemodynamics*

A number of studies have sought to assess the geometrical characteristics of different options used to perform the TCPC surgery and characterize their impact on TCPC hemodynamics, the single ventricle performance, and overall patient outcome. Magnetic resonance imaging (MRI) has emerged as an attractive non-invasive and low-risk imaging technology to assess TCPC hemodynamics in vivo as it allows for the acquisition of both anatomy and flow. With the advent of image segmentation, interpolation, surface fitting and visualization methods, raw magnitude and phase contrast MRI (PC MRI) techniques can be used to reconstruct the 3D in vivo anatomies and velocity fields, respectively.

MRI has been used by several groups to reconstruct Fontan anatomies and obtain time-varying flow information. In particular, Dr Yoganathan's laboratory at the Georgia Institute of Technology has collected a large database of Fontan anatomies and flows, which now includes data of over 250 patients recruited at the Children's Healthcare of Atlanta (CHOA), the Children's Hospital of Philadelphia (CHOP), and the Children's Hospital of Boston (CHB). This wealth of in vivo data has provided a unique opportunity to look at the geometrical characteristics of a wide range of TCPC implementations. Variations in the geometry of the completed TCPCs depend on the surgical options retained at each one of the TCPC stages (e.g. intra-atrial vs.

extra-cardiac) as well as on the native patient anatomy. It is highly unlikely that there would be one single surgical implementation that will be optimal for all patients.

1.3.5 *State of art in experimental and computational modelling of TCPC hemodynamics*

As the TCPC connection is the parameter over which surgeons have some degree of control, it is critical that its design be optimized for a minimal contribution to the overall pressure drops and power losses across the circulatory system. Previous in vivo, in vitro and numerical studies have all demonstrated a direct relationship between TCPC design and efficiency. Early in vitro or numerical studies have investigated the impact of different geometric parameters. While these studies illustrated simple clinically applicable design concepts, optimizing the TCPC geometry therefore requires a thorough understanding of the complete in vivo picture, including anatomically-accurate TCPC geometries, inflow conditions, wall material properties or wall motion, respiration and lung resistance, as well as an exhaustive characterization of the end-points of interest.

The need for more realistic modelling is illustrated by one of the most debated clinical questions regarding TCPC implementation: whether to use an *intra-atrial tunnel* or an *extra-cardiac conduit* to perform the 3rd and final stage of the TCPC procedure. Differences between the two procedures include the baffle geometry, wall properties and wall motion, pulsatibility levels, growth potential, and impact on cardiac electrophysiology.

1.3.6 *Vessel wall deformation*

The majority of TCPC simulations to date have employed a rigid wall approximation.

Orlando et al. (2002) [**22**] were the first to look into the impact of wall compliance on the TCPC hemodynamics, reporting a 10% increase in power losses when compared to the same simulations conducted using rigid walls. However, this study used an idealized TCPC geometry and a uniform approximation of TCPC vessel wall elasticity.

Recent advances in fluid structure interaction (FSI) capabilities have enabled simulation in complex patient-specific geometries with realistic vessel wall

deformation. Efficient algorithms for FSI have been developed and tailored for cardiovascular applications. Bazilevs and Marsden (2009) [**23**] demonstrated significant over prediction of wall shear stress using rigid deformable walls in a patient specific TCPC simulation, particularly under exercise flow conditions.

1.3.7 *Prediction of hepatic flow distribution*

Simulations offer the capability to quantify distribution of hepatic flow to the pulmonary arteries, which is known to have direct clinical implications in the formation of PAVM's (pulmonary arteriovenous malformation). While it is not known what concentration of hepatic flow is required for normal lung development. It is a reasonable assumption that hepatic flow should be distributed as equally as possible, taking into account the possibility of postoperative pulmonary artery remodelling.

1.3.8 *Recent progress towards clinical application*

Although, most CFD studies to date have been limited to retrospective theoretical investigations, the potential benefit of CFD techniques for improved diagnostics and surgical planning for single ventricle patients is gaining interest in the clinical community. Well resolved, image-based CFD simulations offer the opportunity to complement clinical in vivo data, allowing clinicians to access wall shear stress, flow distribution, energy dissipation or pressure data that would otherwise not be available. More importantly, numerical tools offer a unique opportunity to consider multiple "What if?" scenarios, at no risk to the patient. Of particular interest is the ability to predict the patient's response under exercise conditions and to virtually plan and optimize the surgery for a specific patient prior to entering the operating room. In this section we outline the major areas of potential clinical application of simulations and discuss issues of clinical validation.

1.3.9 *Virtual Exercise Testing*

Simulations of exercise flow conditions have the potential to be valuable as a clinical tool, particularly since measurements of exercise pressures and flow are challenging to perform in vivo. Exercise is a complex physiologic state, and

comprehensive modelling of exercise conditions is challenging. However, recent simulation work has emphasized the need to consider exercise conditions in the evaluation of TCPC designs. In particular, results have demonstrated that designs optimal at rest may not be optimal at exercise and vice versa.

Simulating exercise conditions across multiple Fontan patients, both Marsden et al. (2010) [**24**] demonstrated that hemodynamic quantities, including pressure and energy efficiency, vary dramatically with exercise. Marsden emphasized that pressures can rise to alarming levels during exercise for some patients, with pressures in the range of 25–35 mmHg at maximum exercise, yet remain at more moderate levels for other patients. A clinical study of Shachar et al. (2010) [**25**] confirms the dramatic pressure rise during exercise on the order of values predicted by this work, but surgical techniques have evolved significantly since then, and further clinical study focusing on exercise pressures in the current patient population with ECC- and LT-type Fontans is needed. The lumped-parameter study of Sundareswaran et al. (2008) [**26**] also points out that above a certain TCPC resistance patients may simply be unable to achieve the desired cardiac output, thereby limiting their exercise capacity. Exercise flow conditions may thus prove to be an essential component to clinical decision-making and surgical planning for particular patients.

1.3.10 *Summary*

From the above clinical follow-up studies, which demonstrate the morbidity and decreased functional status of Fontan patients, it is clear that improvements are needed. Several palliative options have been discussed in the literature, but clearly the wide variety of patient anatomies makes it difficult to design a general “one-size-fits-all” procedure for Fontan patients. In parallel, the complexity and variability of in vivo anatomies pose significant clinical challenges to identify the surgical option for a given patient, i.e. the one that will optimally distribute hepatic flow to the lungs and offer the lowest vascular resistance.

1.4 **Aim of the study: Calculation of Hydraulic Losses**

The main goal of this thesis is to study and find an easily applicable model during surgery, which minimizes the **dissipation of energy** through a computational study.

In the normal circulatory system there is the hydrodynamic energy dissipation, which occurs due to friction imposed by the viscosity of blood. Mechanical power produced by the contraction of the heart is continuously dissipated into heat via viscous friction as evident by the loss of total pressure from the arterial to the venous sides of the systemic and pulmonary circulations.

But, in certain pathological situations such as unfavourable vessel geometries causing flow separation and/or collision, energy dissipation may far exceed tolerable levels. Independent of the disease type, high energy dissipation always impacts the pumping ventricle that, together with the peripheral vasculature, adapts itself to work harder to overcome the added drag in order to meet the functions [**27**].

1.4.1 *Mechanical energy*

Basically, mechanical energy is the ability to accelerate a mass of material over a certain distance. Although energy can also be reported in calories or kilowatt-hours, in the setting of evaluating cardiac performance, energy is measured in joules. In its simplest form the definition of 1 joule is as follows [**28**]:

$$1 \cdot J = 1 \cdot N \cdot m = 1 \cdot Pa \cdot m^3 = 1 \cdot \frac{Kg \cdot m^2}{s^2} \tag{1.4}$$

where J represents joules (units of energy), N Newtons (units of force), m meters (units of distance), Pa Pascals (units of pressure), kg kilograms (units of mass), and s seconds (units of time).

Equation 1.4 shows that energy per unit distance has the same dimensions as force, and energy per unit volume the same dimension as pressure. In evaluating cardiac performance, pressure measurement is most commonly used, and because of this, the clearest way to report energy in medicine is on a per unit of volume basis. Hence, the energy per unit volume of blood will be reported.

In the circulatory system, mechanical energy can exist in three forms:

1. static pressure,
2. acceleration resulting from gravity,
3. kinetic energy.

Pressure

Pressure (*p*) is a form of mechanical energy per unit volume that represents a force (*Fp*) per unit area (*A*). If a force moves a mass over a distance (*d*), it performs work, expending pressure energy (*Ep*). The area that the force acts on multiplied by the same distance represents a volume (*V*):

$$F = \frac{F_p}{A} = \frac{F_p d}{Ad} = \frac{E_p}{V}$$

1.5

Acceleration due to gravity

Acceleration due to gravity (*g*) creates another form of mechanical energy per unit volume. A mass (*m*) accelerating due to gravity creates a force (*Fg*). If this force moves the mass over a vertical distance (*h*), it too performs work and expends gravitational energy (*Eg*). The energy per unit volume is obtained by substituting density (ρ) for mass per unit volume [**29**].

$$\rho g h = \frac{mgh}{V} = \frac{F_g\, h}{V} = \frac{E_g}{V}$$

1.6

Kinetic energy

Mechanical energy per unit volume also can exist in the form of kinetic energy, or energy of movement. If a mass (*m*) is moving at a velocity (*v*), it contains kinetic energy, equivalent to half the product of the mass and the square of the velocity:

$$\frac{1}{2}\rho v^2 = \frac{{}^1\!/_2\, mv^2}{V} = \frac{E_K}{V}$$

1.7

Again, the energy per unit volume is obtained by substituting density for mass per unit volume.

Pressure, gravitational, and kinetic energies in the circulation can be freely converted from one form to another without energy loss. This concept is illustrated by Bernoulli's equation, which relates the relative amounts of pressure, gravitational, and kinetic energy per unit volume between two spatial locations along a path in the flow, **assuming no energy is lost** [**30**]**.**

$$\frac{1}{2}\rho v_1^2 + \rho g h_1 + p_1 = \frac{1}{2}\rho v_2^2 + \rho g h_2 + p_2$$

1.8

This is the Equation of Bernoulli, where:

- $\frac{1}{2}\rho v^2$ is kinetic energy,
- ρgh is acceleration owing to gravity.

Bernoulli's equation for *steady flow* states the total mechanical energy per unit volume at two spatial locations is the same but can exist in different forms. For example, a decrease in pressure from one location to another may be balanced by an increase in either fluid velocity or height without loss of total energy. A pressure drop measured between two locations is, therefore, not mechanical energy loss if it is accompanied by increases in either gravitational or kinetic energy. These energies can be converted back to pressure energy later.

1.4.2 *Source of Mechanical Energy in the circulation*

The primary source of mechanical energy in the circulation is work performed by the left ventricle. Ventricular contraction generates mechanical energy in blood in the form of static pressure. Conversion of pressure to kinetic energy leads to movement of a volume of blood. The cycle begins with the period of diastolic filling, when the

mitral valve is open and the ventricle fills (figure 1.15-curve between points 1 and 2). When the mitral valve closes, the period of isovolumic contraction begins. For a period of time the volume in the ventricle remains constant, but the pressure rises rapidly (figure 1.15-curve between points 2 and 3). When the aortic valve opens, starting the period of systolic ejection, blood moves out of the ventricle into the ascending aorta (figure 1.15-curve between points 3 and 4). When the aortic valve closes, the period of isovolumic relaxation begins (figure 1.15-curve between points 4 and 1). During this period before the mitral valve opens, the ventricular volume again remains constant, but the pressure falls, returning to the start of the next cycle.

The energy generated by the ventricle during one cardiac cycle is equivalent to the integral of the pressure-volume diagram (figure 1.15-shaded area). The energy per unit volume generated by the ventricle is equivalent to the integral of the pressure diagram divided by the stroke volume. This is roughly equivalent to the average increase in left ventricular pressure from diastole to systole. *The ventricle thus creates energy in the form of static pressure, and this energy is converted to gravitational and kinetic energy elsewhere in the circulation* [**31**].

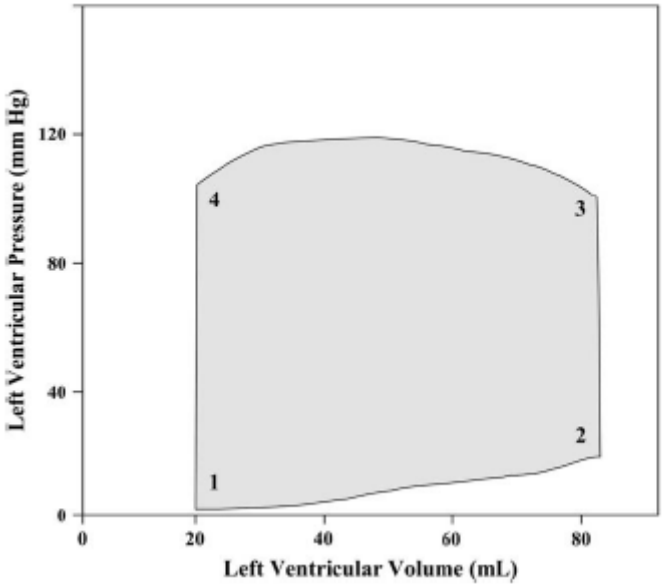

Figure 1.15 Pressure-volume diagram of one cardiac cycle

1.4.3 *Mechanical Energy Loss*

In addition to its conversion between pressure, gravitational, and kinetic forms, mechanical energy can be converted to heat through friction between moving blood and the stationary vessel walls. Such heat cannot be reconverted to mechanical energy, and thus energy is said to be lost.

Frictional energy losses take one of three forms: *viscous losses, turbulence losses, and flow separation losses*. All such losses are the result of the fluid interaction with the solid boundary of the vessel wall.

Viscous losses

As a result of frictional forces, fluid immediately adjacent to a solid boundary moves with the same velocity as the boundary. In the case of a *stationary vessel*, fluid immediately adjacent to the vessel wall does not move, no matter how fast the more central flow is moving. As one moves away from the solid boundary, the velocity of the fluid increases with respect to the radial distance within the vessel (figure 1.16). Fluid viscosity, the tendency of fluid components or molecules to ‘‘stick’’ to each other, creates friction between the fluid components in close proximity if they move at different velocities. This is the mechanism of viscous energy loss. Viscous energy losses are proportional to flow rate.

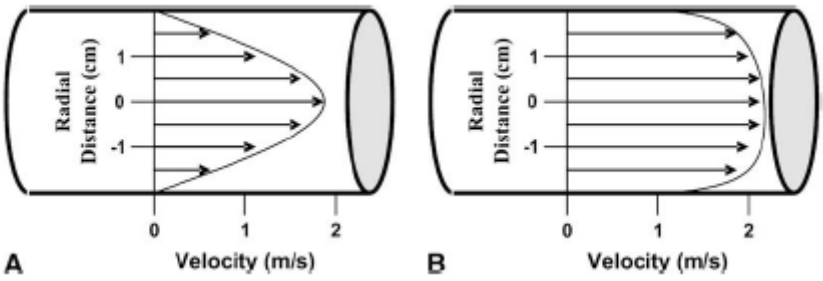

Figure 1.16 Flow velocity profile under laminar conditions (A) and turbulent conditions.

Turbulent losses

Turbulent losses usually do not occur in the healthy circulation, but when they do, they can be of greater magnitude than viscous losses. Turbulence is characterized by random spatial and temporal differences in direction and magnitude of fluid velocity and is the result of the inertia of flow being too great for frictional forces to stabilize

fluid movement. The tendency for turbulence in fluid flow depends on the geometry of the path that the fluid must travel and the ratio of inertial to frictional forces in the flow, (in blood flow this ratio is approximated by the Reynolds number) [**31**].

Flow separation losses

Flow separation occurs when slow moving flow near a solid boundary reverses its direction. In the circulation, such reversal occurs either after the passage of the pressure wave from the heart or after the flow has experienced a sudden expansion.

In both situations flow experiences deceleration, or decrease in kinetic energy. Bernoulli's equation shows that in the absence of differences in gravitational energy, a decrease in kinetic energy is accompanied by a rise in downstream pressure. If such a rise in pressure occurs, it can overcome the inertia of the slow moving flow near the vessel wall, reversing its direction. Substantial energy may be required to reinitiate the forward movement of the fluid. This is energy loss resulting from flow separation. Like turbulence, flow separation originates from changes in fluid momentum, and energy loss from separation is generally proportional to the square of the flow rate [**31**].

Implications of Pathologic Energy Loss

Energy loss is a normal feature of the circulation. The left ventricle is designed to generate the amount of energy needed to overcome these losses in the healthy circulation while moving blood at a rate necessary for normal cellular metabolism.

However, pathologic conditions, such as *single ventricle heart defect* create **additional sources of energy loss**. To supply blood at the necessary rate, the ventricle must perform additional work to overcome the added energy loss. To do this the ventricle must raise its systolic pressure and/or volumetric capacity. Both of these changes result in an increase in stress on the myocardium.

When the heart experiences supernormal hemodynamic pressures or volume loads, the myocardium suffer of **hypertrophy** and/or **dilatation**. These compensatory remodelling mechanisms attempt to provide the additional work required to overcome energy losses. Increased load induction can affect the regulation of myocyte gene expression and lead to molecular, cellular, and interstitial

changes within the myocardium. This biochemical cellular response to mechanical stimuli, known as mechano-transduction, is not well understood [**32**].

The additional flow impedance along the outflow tract causes ventricular pressure overload. Peak systolic pressure increases result in the myocardium experiencing higher peak systolic stresses, which act as the trigger for concentric hypertrophy, in which the ventricular wall thickens with the addition of myofibrils in parallel.

The ventricle alters its shape to a more prolate spheroid, with a decrease in the short axis with respect to the long axis.

Myocardial hypertrophy can occur within hours from the onset of a new stimulus and can double ventricular mass within a week. In gradually worsening systolic or diastolic stresses, the hypertrophy can be insidious. In general, hypertrophy compensates for altered stresses; the additional thickness and altered geometry of concentric hypertrophy reduce peak systolic myofiber stresses, while additional capacitance and the more spherical shape of the ventricle from eccentric hypertrophy reduce diastolic fiber stresses. Hypertrophy proceeds until fiber stresses are normalized in a negative feedback system. The feedback mechanisms for the two kinds of hypertrophy operate largely independently. With eccentric hypertrophy, a certain degree of concentric hypertrophy is also activated due to the increase in ventricular volume to mass ratio, which demands additional ventricular work [**33**].

The point at which remodelling transitions from beneficial to detrimental has not been well described clinically, mechanically or biochemically.

Current Limitations of the Use of Energy Loss

Direct calculation of energy loss is both invasive and complex. Mechanical energy losses are usually determined by measuring static pressure, velocity, and height differentials at two locations in the bloodstream. Such a calculation requires simultaneous temporal knowledge of the velocity and pressure profiles at these locations. Pressure gradient and effective orifice area, in contrast, are correlated with total energy loss and can be estimated noninvasively by Doppler echocardiography. Nonetheless, there are known parameters that can be easily and noninvasively measured and correlate better with energy loss than do pressure gradient and effective orifice area.

CHAPTER 2
GEOMETRICAL MODEL

This chapter describes the process for preparing geometrical model for CFD simulations.

The first part of the chapter explains a series of features that must be present on the TECPC model regarding energy preservation and safe clinical applicability, reason for which, in vitro quantitative and qualitative analyses of the flow fields are carried out.

In particular, the position of the venas cava are studied in relation to the pulmonary arteries. The inferior vena cava (IVC) conduit is positioned to the left by bidirectional Glenn anastomis. The elements that can alter potential energy loss, for example, the presence of offset, the flow ratio that represents the distribution of pulmonary resistance, and the total flow rate to the entrance of the venas cava conduits. Thanks to MRI, the determination of realistic size is also studied.

The central part shows the section of the geometrical model that was chosen according to the studies where all the steps are explained in order

to obtain the lengths of both the venas cava and pulmonary artery. The lengths were calculated by evaluating the regime of the flow, through the Reynolds number, ensuring to have a fully developed flow at its end, thereby allowing to reliable results.

The final part explains how the software SolidWorks was used in order to create the geometrical model for the CFD simulation.

2.1 **Introduction**

To date, the majority of surgical planning studies have examined a small number of geometry variations using a "trial-and-error" approach to surgical design [**34**]. In contrast, many engineering fields such as aeronautics and automotive design commonly rely on automated optimal shape design in their design process. The potential benefits of optimization for patient specific surgical planning compared to trial and error methods include: 1) systematic and efficient exploration of the design space, 2) potential identification of non-intuitive designs, and 3) a guarantee that the best design has been identified. However, the application of automated optimization tools to surgical planning presents several significant challenges. First, appropriate measures of performance (cost functions and constraints) for cardiovascular designs must be defined based on physiologic information and hemodynamics. Second, the choice of optimization method must be appropriate for expensive, pulsatile, 3D fluid mechanics problems. Third, efficient parameterization of patient-specific geometries poses a formidable challenge and expense. And finally, the cost of evaluating the cost function and, if needed, the cost function gradient, may become extremely expensive as the problem complexity increases and the number of design parameters becomes large.

2.2 **TECPC model**

Total extracardiac cavopulmonary connection is an established procedure in the sector of surgical procedure. In fact, many institutions have achieved good, early and midterm results with both intracardiac TCPC and TECPC. Nonetheless the best spatial arrangement remains controversial.

Several studies were done to determine the best TECPC model, in terms of both energy preservation and safe clinical applicability. These studies are based on a 12-year experience with TECPC and deals with in vitro quantitative and qualitative analyses of the flow fields.

TECPC is a spatially complex system that demands a high-performance method for the flow field analysis. In particular an application of velocity fields generated by particle imaging velocimetry (PIV) was used that provides a highly accurate flow mapping, both spatially and temporally. A finite-element numeric model was also

built on the basis of in vitro measurements, of which the results were compared with the PIV results [**35**].

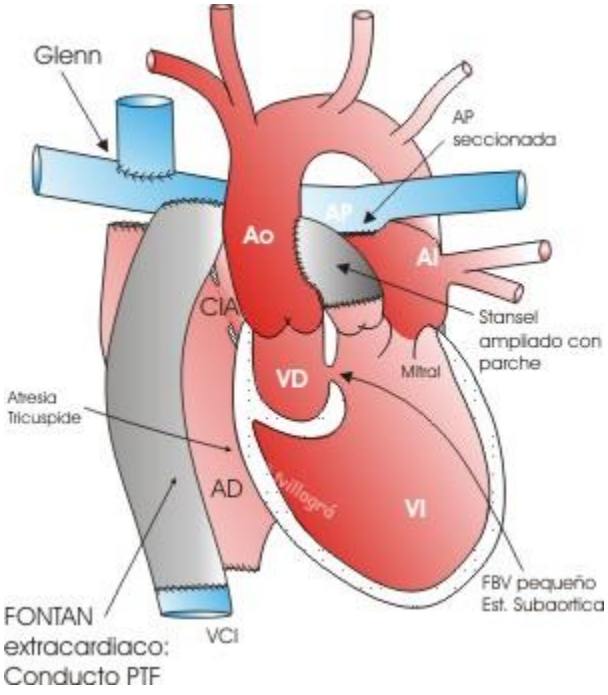

Figure 2.1 TECPC Model

2.2.1 *Spatial arrangements of TECPC*

In recent years, increasingly sophisticated in vitro, in vivo, and computational studies on the best fluid dynamics among different spatial arrangements of TECPC have concurred and come to the conclusion that the two cavopulmonary anastomoses should not be placed in a face to face configuration but rather should be deflected to opposite sides.

Particularly, in the model of TECPC, the IVC inflow is usually directed on the left by the bidirectional *Glenn anastomosis*, because with the IVC inflow on the right of the bidirectional Glenn anastomosis, the IVC conduit may fall too close to or, nearly always, on the right lower lobar artery, and this in turn may be deleterious for a series of reasons. First, the right lower lobar artery extends in different plane and orientation than the IVC conduit RPA anastomosis, and this may cause kinking of the artery itself, with impairment of right lung perfusion. Second, a relatively rigid

structure, such as the prosthetic IVC conduit, may easily impinge on a thin vessel, such as a lobar artery. Third, the IVC connection to a zone of bifurcation and partition of flows is characterized by a worse hydrodynamic pattern than in the case of connection to a main vessel. Another advantage of the left-sided position of the IVC conduit could be a reduced shear stress at the anastomotic level.

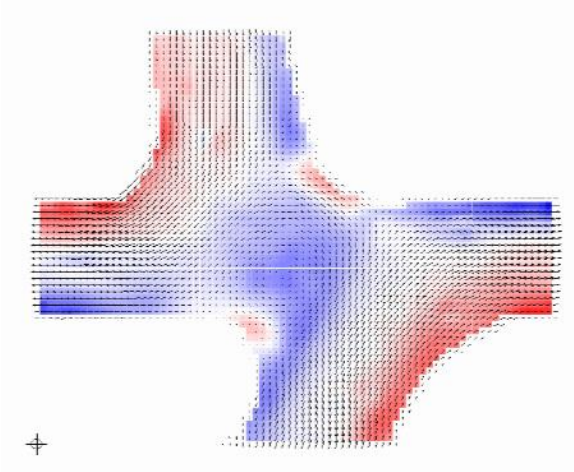

Figure 2.2 Bifurcation of the conduit

2.2.2 *The potential energy losses of the models*

An interesting aspect is that the power loss measurements did not follow a simple Poiseullian flow scheme: the values were higher than those obtainable with the simple calculation relative to a steady Poiseullian state. The reason for the higher dissipation may be found in the particular flow field generated by each caval connection topology.

The potential energy losses of the models varied with *offset*, *flow ratio* and *flow rate*.

Offset

The offset is defined as the horizontal distance between the caval midpoints. The presence of an offset, in the TECPC model, which increased from 0.0 to 0.5 superior

vena caval diameters, showed a substantial decrease of power losses. When the offset was increased further from 0.5 to 1.0 superior vena caval diameters, there was an additional decrease in the power losses but less marked than the initial decrease. Thereafter, further increases in offset resulted in no significant change in power

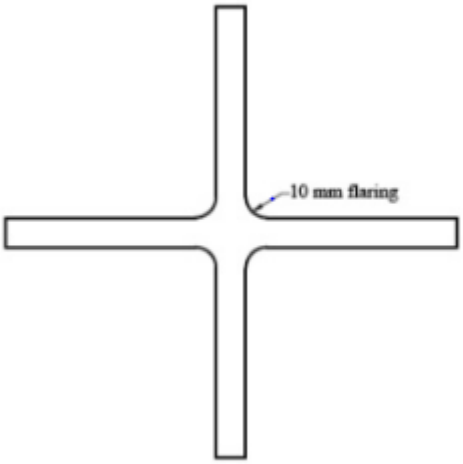

Figure 2.4 Model with zero diameters offset

losses, and the losses for 1.0, 1.5 and 2.0 diameter offsets did not appear to be significantly different from one another.

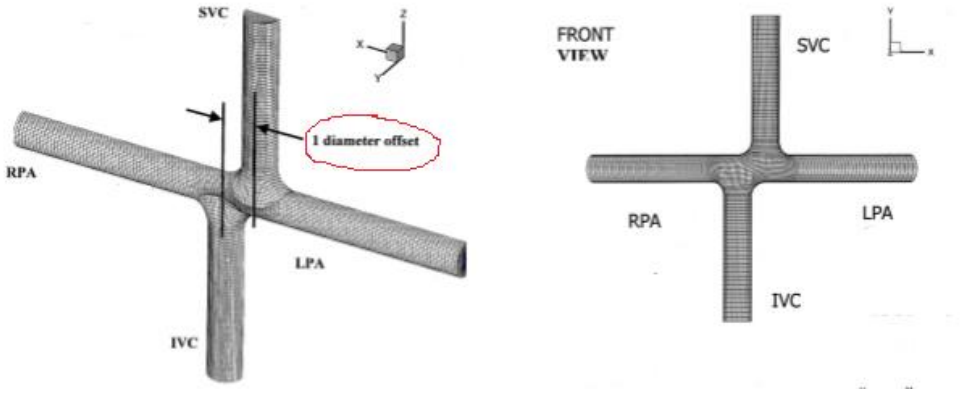

Figure 2.5 Model with 1 diameter offset

Furthermore, the zero diameter offset case demonstrates that the relatively parallel path lines of flow in the two cavae turned into a disorganized pattern of path lines at the site of collision of flow. The 0.5 diameter offset case demonstrates a vortex at the offset site of the cavae, that seemed to play a beneficial role as a flow division structure. This apparent vortex was not a true vortex (a place of accumulation of vorticity), but more correctly, it was a circulation zone, because such a rotation would not necessarily be associated with an accumulation of vorticity at its center. Moreover, the left-sided position of the IVC conduit, in addition to offering a higher

simplicity of offsetting and flaring, is potentially less compressive on the right pulmonary veins.

The higher offsets also demonstrated a vortex, but it was less well defined and less vigorous than the 0.5 diameter offset.

Flow ratio of the pulmonary arteries

At the same time, the power losses of variable pulmonary *flow ratio* were evaluated. The different RPA/LPA flow proportions were applied, varying from 50/50 to 70/30 and 30/70 but the position of the vortex shifted from the central position to the upper right or lower left part of the cross, away from the pulmonary artery, until it vanished. Therefore, when the pulmonary resistance was equally distributed (50/50 pulmonary flow ratio), the power losses associated with the offset were lowest.

Flow ratio of the venas cava

The flow ratios for the inferior and superior cavae were fixed at 60/40, respectively, which was used to reflect the higher superior vena caval flow seen in infants and young children.

Flow rate

All these parameters were obtained considering a *flow rate* between 2 and 6 litres/min [**36**].

2.2.3 *Determination model size*

To obtain realistic sizes of the inferior and superior vena cavae and right and left pulmonary arteries, an 8-year old boy with a Fontan operation was put through magnetic resonance imaging (MRI). The magnetic resonance images were then transferred to a workstation for image segmentation and three-dimensional reconstruction. From the computer reconstruction, the sizes of inferior and superior vena cavae and right and left pulmonary arteries were measured.

2.3 **Approximate Geometrical Model Applied**

The geometrical model, for our CFD investigation, was chosen according to the studies mentioned in the previous paragraph (TECPC model).

The model presents the diameter of the superior vena cava (SVC) that of the inferior vena cava (IVC), which is equal to 11.5 mm, whereas to the left pulmonary artery (RPA) is equal to 8.6 mm. Moreover, an offset of 0.6 mm was imposed, between IVC and SVC axis and an anastomosis was realized by means of an extracardiac conduit, inclined toward LPA, at an angle of 22°, between IVC and LPA [**37**].

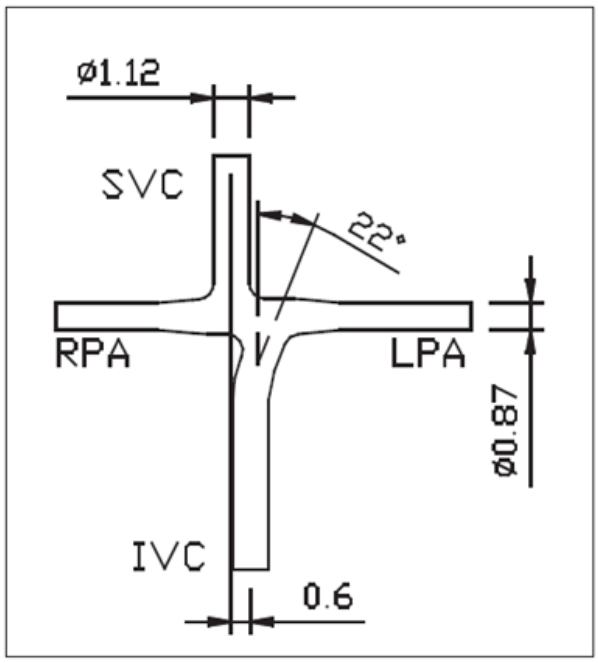

Figure 2.2.6 Sketch of the longitudinal section of TCPC configuration investigated. The dimensions are in cm.

This geometry was evaluated in terms of hydraulic performance, under different fluid dynamic condition (related to the whole three-dimensional fluid dynamic domain), adopting two energetic indices: the *power dissipation* and the *pressure loss coefficient*.

Power dissipation was calculated as follows:

$$W = W_{venae\ Cavae} - W_{pulmonary\ Arteries} \quad \textbf{2.2.1}$$

$$W = \sum_{i=IVC,SVC} \left(\frac{1}{2}\rho V_i^2 + P_i\right) Q_i - \sum_{j=LPA,RPA} \left(\frac{1}{2}\rho V_j^2 + P_j\right) Q_j \quad \textbf{2.2.2}$$

Where $V_{i,j}$ is the average velocity (defined as *Q/A*, where *A* represent the area), and $P_{i,j}$ the pressure in the considered vessel, the subscripts *i*, *j* refer to the venae cavae end to the pulmonary arteries.

The pressure loss coefficient K_p is defined as:

$$K_e = \frac{\sum_{i=IVC,SVC} \left(\frac{1}{2}\rho V_i^2 + P_i\right) + \sum_{j=LPA,RPA} \left(\frac{1}{2}\rho V_j^2 + P_j\right)}{\sum_{i=IVC,SVC} \left(\frac{1}{2}\rho V_i^2\right)} \quad \textbf{2.2.3}$$

$$K_p = K_e + \frac{\sum_{j=LPA,RPA} V_j^2 - \sum_{i=IVC,SVC} V_i^2}{\sum_{i=IVC,SVC} V_i^2} \quad \textbf{2.2.4}$$

Where K_e is the energy loss coefficient.

In fact, in basic flow dynamic terms, a TCPC represents two T-junctions with flow velocities going in opposite directions, from SVC and IVC into the pulmonary arteries. For those abrupt changes in geometry and velocity inevitably the energy losses is generated (topic already discussed in the introduction). This problem creates compensatory remodelling mechanisms, that attempt to provide the additional work, required to overcome energy losses. But, with this work the heart experiences supernormal hemodynamic pressures or volume loads, that cause **hypertrophy** and/or **dilation** of the heart.

Hence, the main objective in this field is to find a geometrical model that minimizes the power losses. Under this point of view, this geometry that is considered today in this thesis attempts to present a more efficient solution to reach this objective. Nonetheless, it must be said that many improvements have yet to be made.

2.3.1 *Geometric Model Parameters*

The design software CAD 3D SolidWorks was user in order to prepare for meshing: the first step consists in calculating the length of venas cava and pulmonary arteries, which must ensure a fully developed flow at their end, meaning that the velocity profile does not change towards the downstream coordinate, or towards the stream-wise directions.

Therefore, these 'length' is evaluated thanks to another size: the *entrance length*.

Entrance length

If we take into consideration a flow entering a pipe that is uniform and inviscid, as soon as the flow 'hits' the pipe many changes take place. The most important of these is that viscosity imposes itself on the flow and the *No Slip* condition on the wall of the pipe comes into effect. Consequently the velocity components are all zero on the wall ($u = v = 0$). The flow adjacent to the wall decelerates continuously. As to the layer close to the body, the velocity builds up slowly from zero on the wall to a uniform velocity towards the centre of the pipe. This layer is what is called the *boundary layer*. Viscous effects are dominant within the boundary layer. Outside of this layer is the inviscid core where viscous effects are scarce or absent.

The boundary layer is not a static phenomenon: it is dynamic, growing significantly as its thickness increases as it moves downstream. The boundary layers from the walls grow to such an extent that they all merge on the centreline of the pipe. Once this takes place, the inviscid core stops and the flow becomes entirely/completely viscous. The flow is now called a Fully Developed Flow. The velocity profile becomes parabolic.

The section of the pipe between the start and the point where the fully developed flow begins is called the *Entrance Length* (denoted by L_e) [**38**].

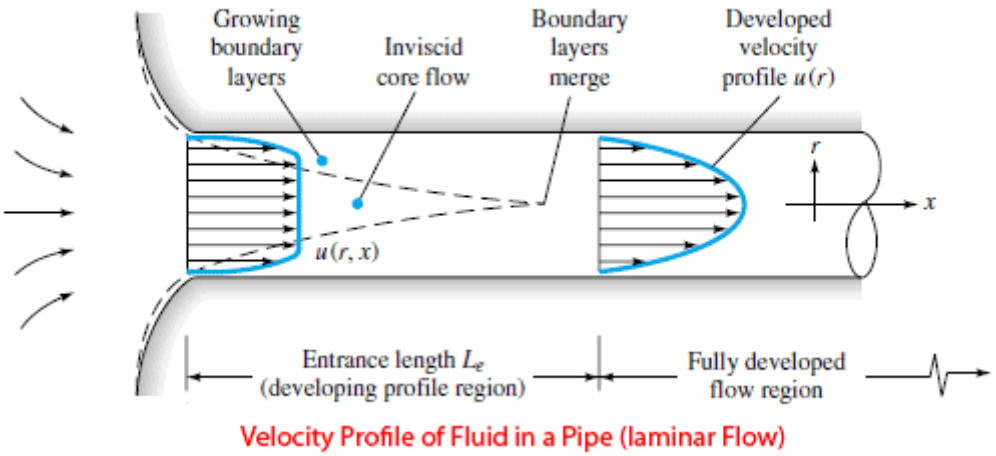

Figure 2.7 Entrance length: developing profile region.

Therefore, the value of the *entrance length* , if each vascular vessel is supposed to be like a pipe and approximately with a constant diameter, is given by the following formula [**39**]:

$$L_{e,laminare} = 0.05 * Re * D \qquad \textbf{2.2.5}$$

This formula is valid in case of laminar flow, and it is in function of *Reynolds Number* of the flow and of the diameter's vessel (confirmed information).

In fluid mechanics, the Reynolds number (Re) is a dimensionless quantity that is used to help predict similar flow patterns in different fluid flow situations, it is defined as the ratio of inertial forces to viscous forces and consequently quantifies the relative importance of these two types of forces for given flow conditions.

It is used to characterize different flow regimes within a similar fluid, such as laminar or turbulent flow [**40**]:

- laminar flow occurs at low Reynolds numbers, where viscous forces are dominant, and is characterized by smooth, constant fluid motion;
- turbulent flow occurs at high Reynolds numbers and is dominated by inertial forces, which tend to produce chaotic eddies, vortices and other flow instabilities.

The critical value, to change from one regime to another, varies according to the kind of geometry: for flows in rough pipes, the critical Reynolds number is usually taken to be 2000, in case of flow between parallel plates the critical number is 1500, using the average velocity of the flow and if the wall is smooth, free of vibrations and the entering flow is free of disturbances [**41**].

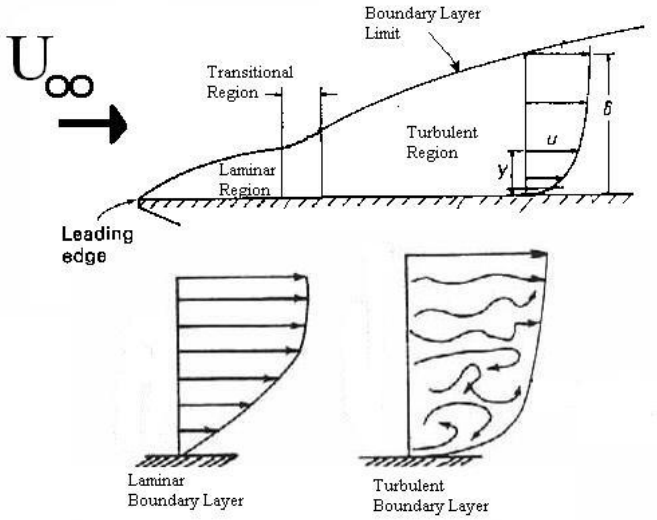

Figure 2.8 From laminar boundary layer to turbulent boundary layer.

The second step is to calculate the Reynolds number and to verify that in the geometric model, the regime is laminar.

The Reynolds number is given by the following formula:

$$Re = \frac{inertial\ forces}{viscous\ forces} = \frac{(mass)(acceleration)}{(dynamic\ viscosity)(velocity/distance)(area)} \quad \textbf{2.2.6}$$

$$Re = \frac{(\rho L^3)(v^2/L)}{\mu(v/L)L^2} = \frac{\rho v L}{\mu} = \frac{vL}{\upsilon} \quad \textbf{2.2.7}$$

Where:

- 'v', [m/s] is the characteristic velocity (here considered as the average velocity);
- 'L', [m] is the characteristic length of the system (here considered as the equivalent diameter of the cross-section);
- 'υ', [$^{m^2}/_{s}$] is the kinematic viscosity of the fluid in motion, which is defined as: $\upsilon = \frac{\mu}{\rho}$;
- 'μ', [$^{N * s}/_{m^2}$] is the viscosity of the fluid;
- 'ρ', [$^{Kg}/_{m^3}$] is the density of the fluid.

The definition include the fluid properties of density and viscosity, plus a velocity and a characteristic dimension. The values for density end for the viscosity of the blood to be respectively 1060 $^{Kg}/_{m^2}$ and 0,0035 $^{N * s}/_{m^2}$ which both correspond to an average haematocrit (Ht) of 43%.

Assuming that the flow rate distribution is 60/40 at the entrance of the model for a total flow rate of 3 *L/m*, the velocity magnitude is set to be 0.192 $^{m}/_{s}$ and 0.29 $^{m}/_{s}$ respectively in the superior vena cava and in the inferior vena cava.

Instead, assuming that the flow rate distribution is 50/50 at the bifurcation of the model, the velocity magnitude is 0.43 $^{m}/_{s}$ in the pulmonary arteries.

The following table shows the Reynolds number evaluated for all the section of inlet and outlet of the model.

	Diameter, $[m]$	Flow rate, $[m^3/s]$	Area, $[m^2]$	Velocity, $[m/s]$	Re
Inlet_SVC	0.0115	$2 * 10^{-5}$	$1.038 * 10^{-4}$	0.192	668.70
Inlet_IVC	0.0115	$3 * 10^{-5}$	$1.038 * 10^{-4}$	0.29	1010.02
Outlet_RPA	0.0086	$2{,}5 * 10^{-5}$	$5.805 * 10^{-5}$	0.43	1119.96
Outlet_LPA	0.0086	$2{,}5 * 10^{-5}$	$5.805 * 10^{-5}$	0.43	1119.96

Table 2.1

It has been noted that the Reynolds number is below the critical value of 2000, hence the regime of the flow is laminar. This is very important for the blood flow, because turbulence can cause damage or endothelial dysfunction, counter-current flow, or stagnation zones (where blood stasis in turn is the most important cause of thrombus). For example, the presence of a turbulent flow damages the fragile platelets, provoking them to aggregate and break and release into the surrounding blood the content of their granules, favouring the formation of the clot.

Therefore, there are all dates in order to calculate the entrance length thanks to the equation 2.2.5 , as the table below shows.

	Re	Diameter, $[m]$	Entrance length, $[m]$
Inlet_SVC	668.70	0.0115	384
Inlet_IVC	1010.02	0.0115	580
Outlet_RPA	1119.96	0.0086	481
Outlet_LPA	1119.96	0.0086	481

Table 2.2

This length, expressed in meters, permits to have a model of vessels in which the flow is fully developed, meaning that the velocity profile does not vary in the flow direction. In fact, in this region the pressure gradient and the shear stress in the **flow are in balance.**

Every application decides whether a long enough entrance length is required or a shorter one is required: in this kind of application a long enough entrance length is required, as the value in the table 2.2 demonstrates.

2.4 **The model construction**

The geometrical model was created with the design software CAD 3D SolidWorks.

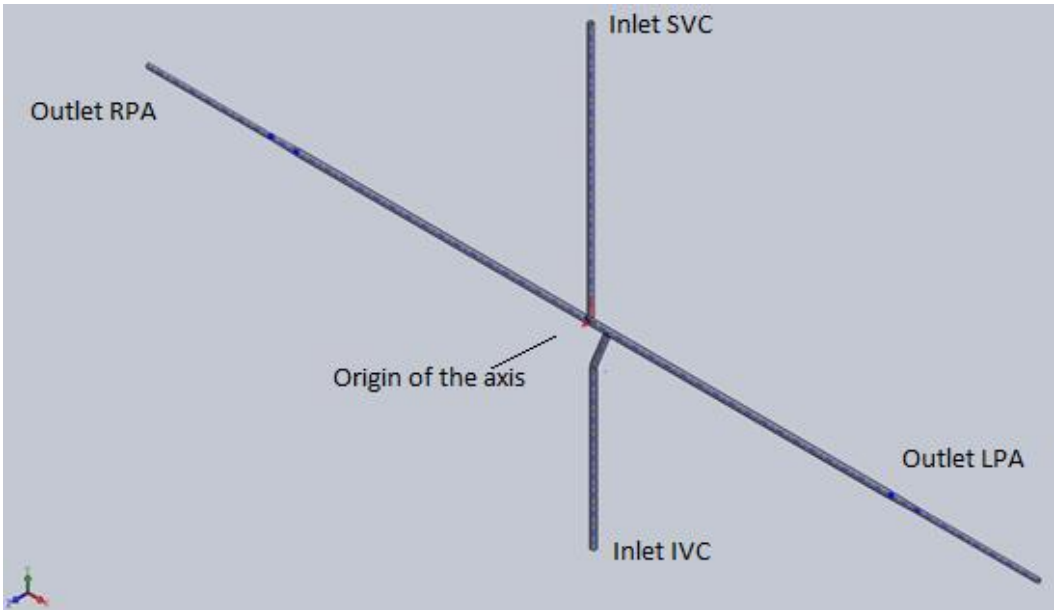

Figure 2.9 Origin of axis

In the CAD model, the origin of the axis was positioned in order that: the x-axis coincided with the axis of symmetry of the superior vena cava, while the y-axis corresponded with the axis of symmetry of pulmonary artery.

During the construction, in addition to being using as a reference for the frontal plane, the superior plane and the right plane, others three plane were used : plane 1 and plane 3 were used to create the IVC conduit, whereas plane 2 was used to create the SVC conduit.

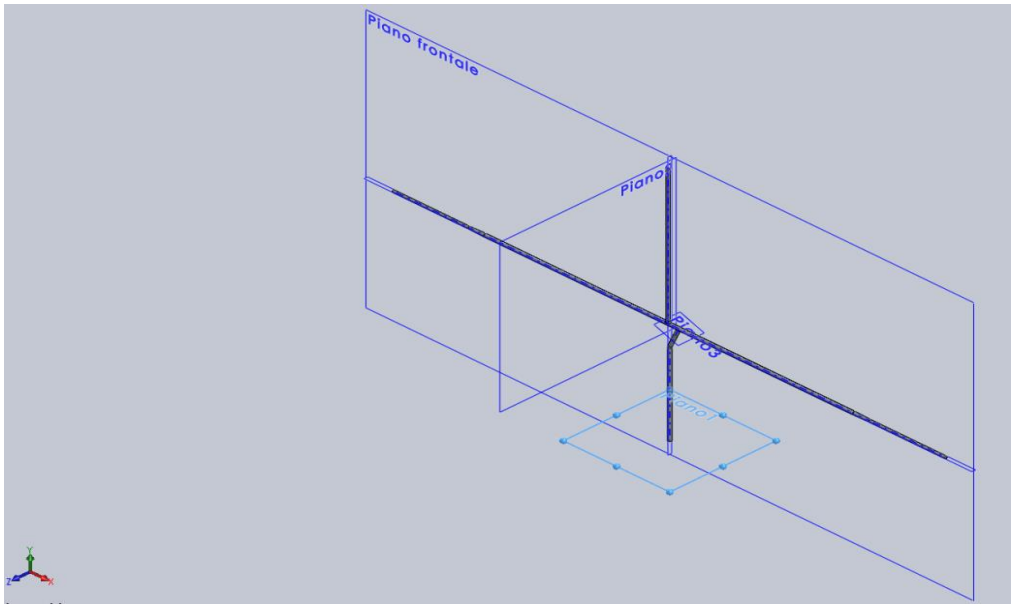

Figure 2.10 Plane of the geometrical model

Plane 1 was created in correspondence with the entrance of the inferior vena cava, a circumference of 11,5 mm was realized on it, whereas on plane 3, an inclination of 22° respect to the symmetry axis of pulmonary artery was applied.

Between the two planes, it was applied the *sweep* function, allowing the creation of IVC inclined duct.

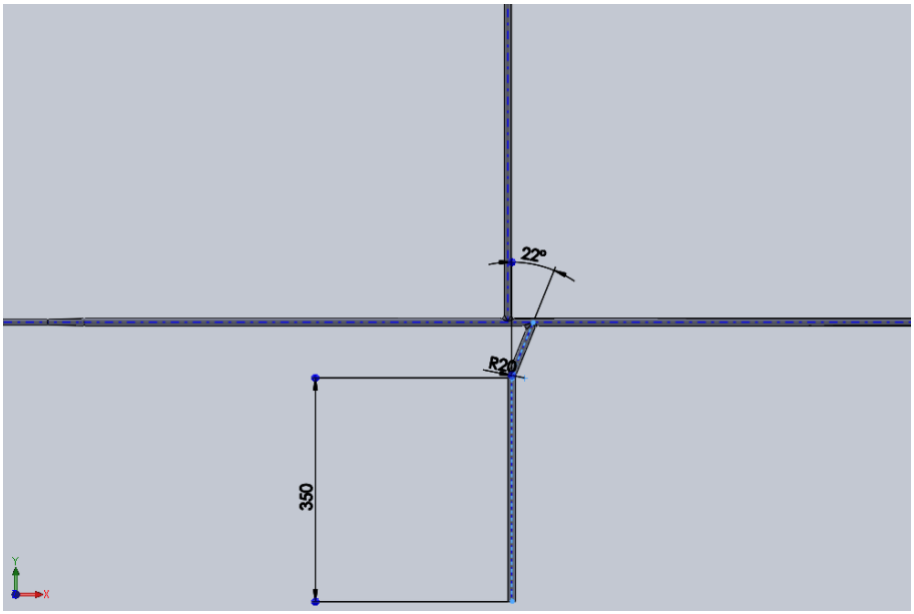

Figure 2.11 IVC Inclination of 22°

The superior vena cava was also created with the *sweep* function, whereas the pulmonary artery was created thanks to the *revolution* function around its axis of symmetry.

The construction of the latter was more complex, due to a variation of diameter along the pulmonary arteries. It has a diameter of 12 mm where the connection with the venas is located, and a diameter of 8,6 mm along the duct toward the outlets, for geometrical constraints.

The offset was created by setting a distance of 0.6 mm between the axis of symmetry of the superior vena cava and inferior vena cava.

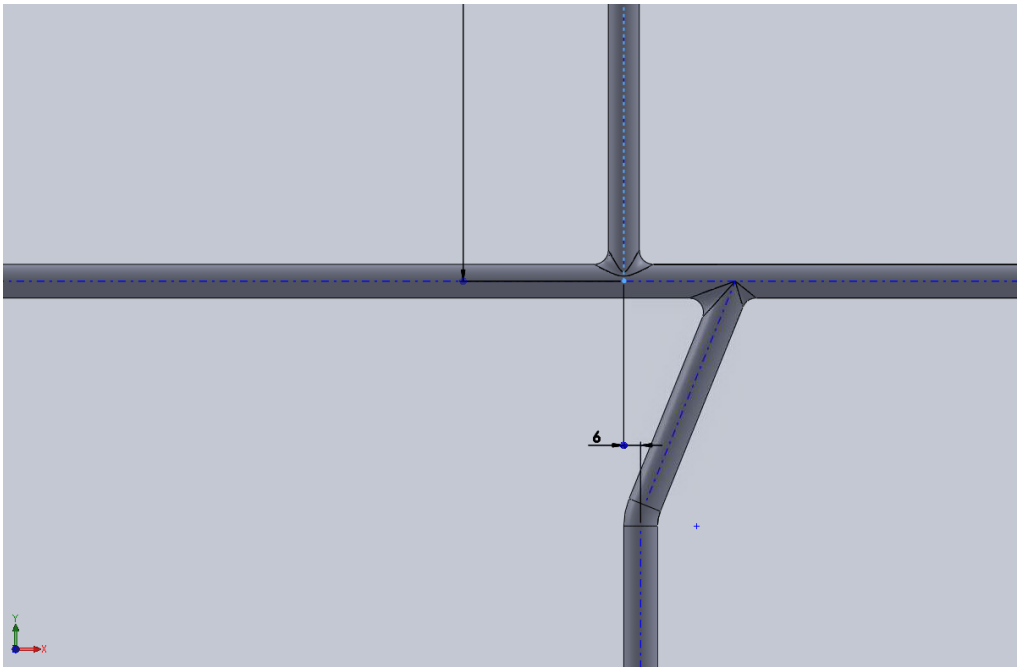

Figure 2.12 Offset of 0.6 mm

In the region where the veins are joined to arteries, the *cut-extruded* function has been applied in order to eliminate parts of the duct that occupied the interior of the model.

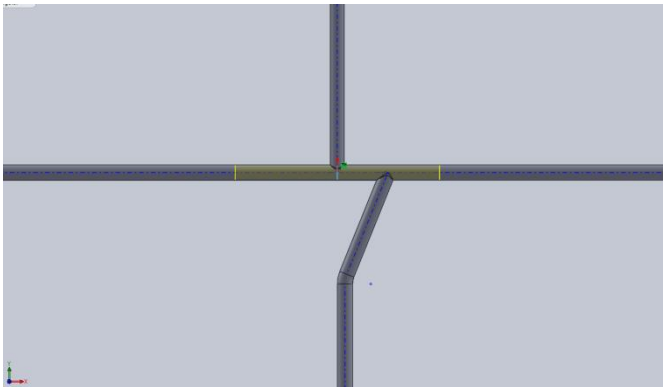

Figure 2.13 a) Cut-extruded function in pulmonary arteries.

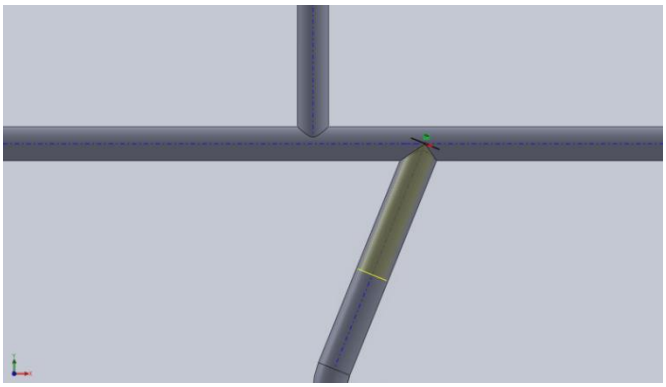

Figure 2.14 b) Cut-extruded function in inferior vena cava.

Moreover, the model does not have sharp edges in order to reduce the losses of energy.

CHAPTER 3
SENSITIVITY ANALYSIS

This chapter describes the pre-processing steps in order to prepare the geometrical models for the CFD simulations. In the first part of the chapter, the study of sensitivity in our geometrical model is explained. The aim of this study was to find which grid spatial resolution is needed for this kind of fluid dynamic application, in order to have results that are independent from the size of the mesh. Several meshes were generated having two main features: a spatial radial gradient with more elements at the wall and fewer in the core, and different grid sizes. These meshes were compared by performing steady state simulations and collecting data of two variables of interest: one field variable, the velocity magnitude, and one hemodynamic wall index, the wall shear stress (WSS). The steady state simulations had the following setting parameters: blood properties typical of an average hematocrit (*Ht*) of 43%, rheological Newtonian behaviour, average velocity inlet boundary condition, outflow with a flow rate weighting of 50% between the two outlet sections.

The second part of the chapter is dedicated to the calculation of hydraulic losses to observe which type of mesh has the lowest dissipation of energy, in order to preserve the functionality of the heart.

In the end, the mesh showing a good compromise between the computational cost, the needed spatial resolution and the hydraulic losses was chosen.

3.1 **Introduction to sensitivity analysis**

After the new geometrical model was built, a *sensitivity analysis* was performed. It is considered as: *the study of how uncertainty in the output of a model (numerical or otherwise) can be apportioned to different sources of uncertainty in the model input* [**42**] .

It is important to determinate which spatial resolution is needed in this case of study in order to have results that are independent from the number of elements of the mesh.

3.1.1 *Discretization of the model: mesh*

An important step of the sensitivity analysis is the fragmentation of the computational domain, changing from a continuous model to a discretized model, to solve the equations that describe the model. Hence, a complex problem is broken down into many simple problems and the solution of all the sub-problems leading to the solution of the general problem. In other words, it consists in switching from an infinite number of degrees of freedom: the continuous, to a finite number of degrees of freedom: the mesh [**43**].

The mesh or grid is composed of geometric primitives (finite element) of mathematically defined shapes, that are mainly triangles and quadrilaterals for 2D domains, hexahedrons and tetrahedrons for 3D domains.

Each mesh was created with the software ICEM 14.5 of ANSYS where the geometrical model was imported as a parasolid file, setting the millimetre as dimension.

After the importation, the model was divided into six parts:

- The WALL (violet)
- The fluid zone: BLOOD
- Two entrance: INLET_SVC / INLET_IVC
- Two exit: OUTLET_RPA / OUTLET_LPA

This was useful in order to be able to mesh each part with specific parameters, which can vary according to the site of the model.

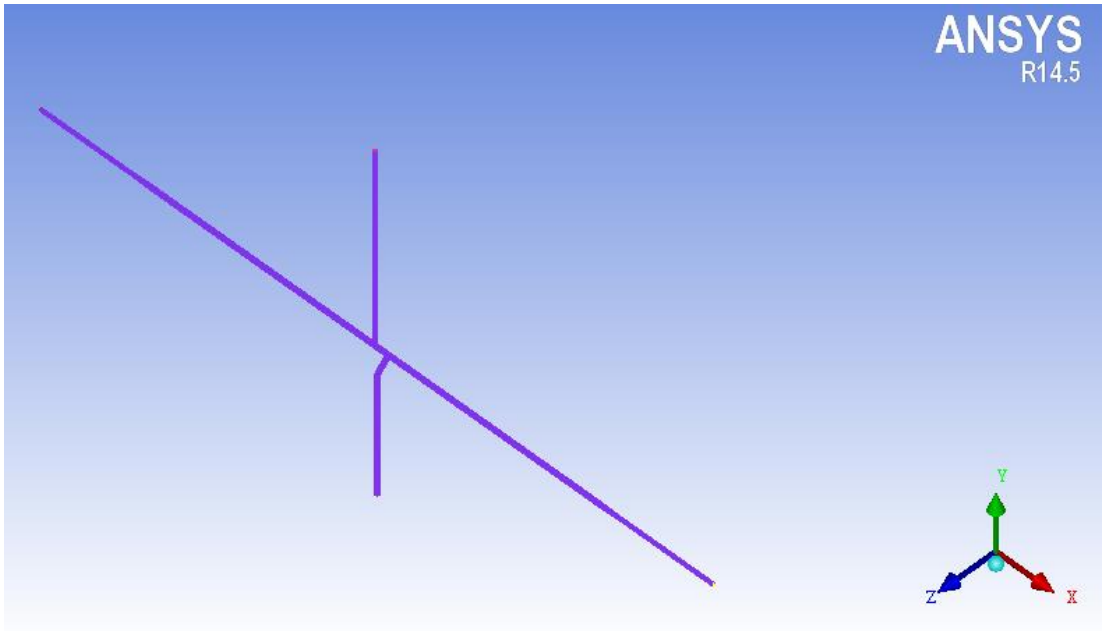

Figure 3.1 Model divides in six parts in ICEM

The mesh divided the geometrical model into many small elements that reproduce in detail the fluid dynamic behavior. Each element was measured in order to define the global element size of the volume mesh. They were not the same: their dimension and shape varied depending on the position that they assume within the model, in fact it is called unstructured Cartesian grid.

A value equal to 2 was chosen to indicate the size of the largest element. The *size limit* for the smallest element was also specified, hence the mesh elements were limited from being subdivided into a smaller element than this value.

The meshes were defined in order to have the larger elements on flat planar surfaces and smaller elements in areas of high curvature or within small gaps.

Furthermore, some different meshing parameters were defined for the surface element size in order to better reproduce the structure of the vascular graft. In this way, a spatial gradient was created, meaning that the mesh at the surface, where the spatial gradients are higher, had more elements, and where the velocity profile does not change so much, the mesh was less thick.

To avoid many elements along a given curve or surface was applied an option of *refinement* was applied, that defines the number of edges that would fit along a radius of curvature, if that radius extended out to 360 degrees.

A value was set to ignored surfaces smaller than the specified value, by merging the smaller loop with the adjacent loop (that is the closed region).

Each mesh was created using the Robust (Octree) method, that generates a tetra mesh, using a top-down meshing approach, and a pure triangular mesh was used to mesh.

At a later time, the prism layers were created on existing mesh, that give an efficient way to achieve better resolution (more calculations per unit distance) of the solution normal to the surface, without increasing the number of elements along the surface, thus giving a quicker and more accurate solution.

For all meshes a number of layer equal to 5 was set, with an initial height of layer equal to 0.2, and a height ratio, which is the expansion ratio from the first layer of elements on the surface, equal to 1.2.

When the creation of the mesh was completed, a diagnostic check of individual element quality was made. Anyhow, they were smoothened according to a particular quality criterion and with a specified number of iterations, to improve their quality. Every mesh contains tetras, pyramids, prisms, triangular and quad surface elements.

Seven meshes for sensitivity analysis were generated by varying the global element size (refinement) in order to create a spatial grid even denser.

The images below give an idea of the mesh that was made, considering as reference the outlet of the right pulmonary artery.

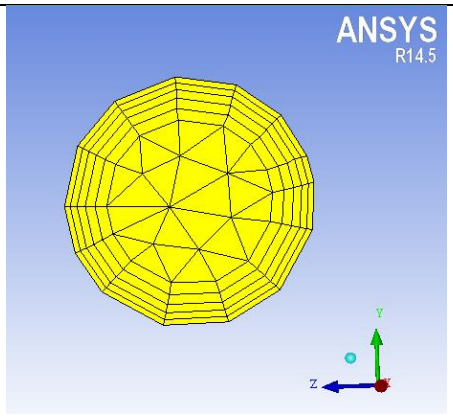

Figure 3.2 Mesh A

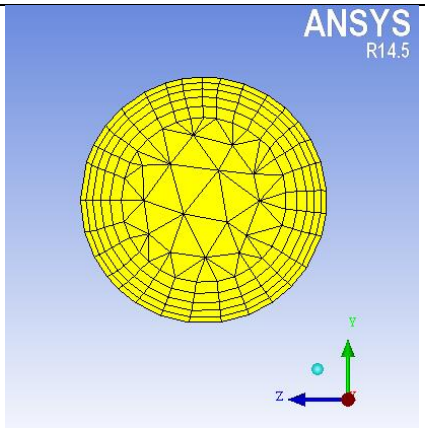

Figure 3.3 Mesh B

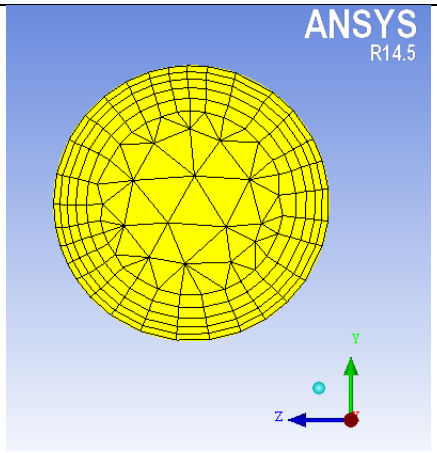

Figure 3.4 Mesh C

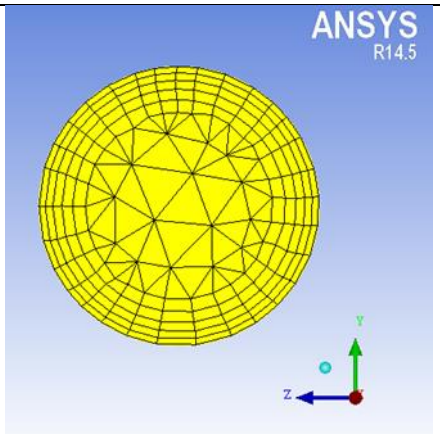

Figure 3.5 Mesh D

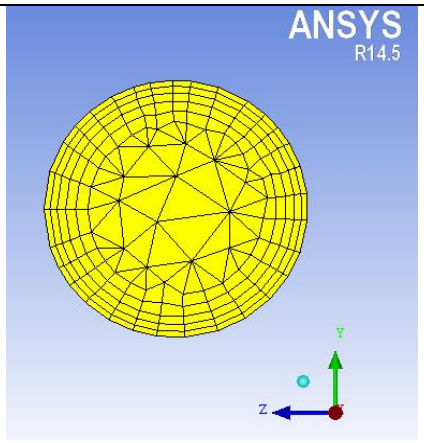

Figure 3.6 Mesh E

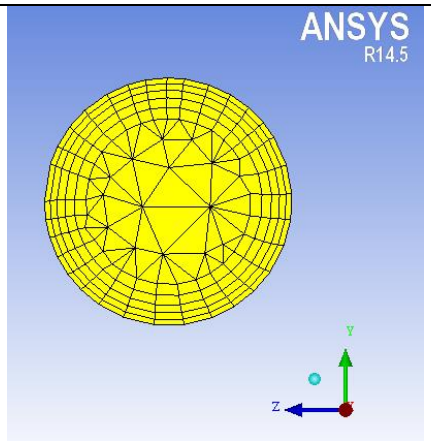

Figure 3.7 Mesh F

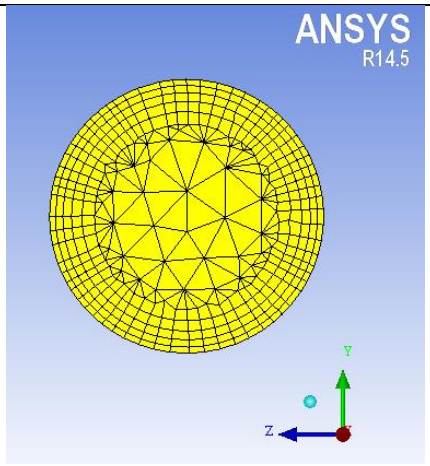

Figure 3.8 Mesh G

Table 3.1 The seven mesh creates by ANSYS

This seven mesh simulation was ordered according to the total number of elements (see chart 3.1), and the quality parameters were in the suitable range for this application (see chart 3.2-3.3).

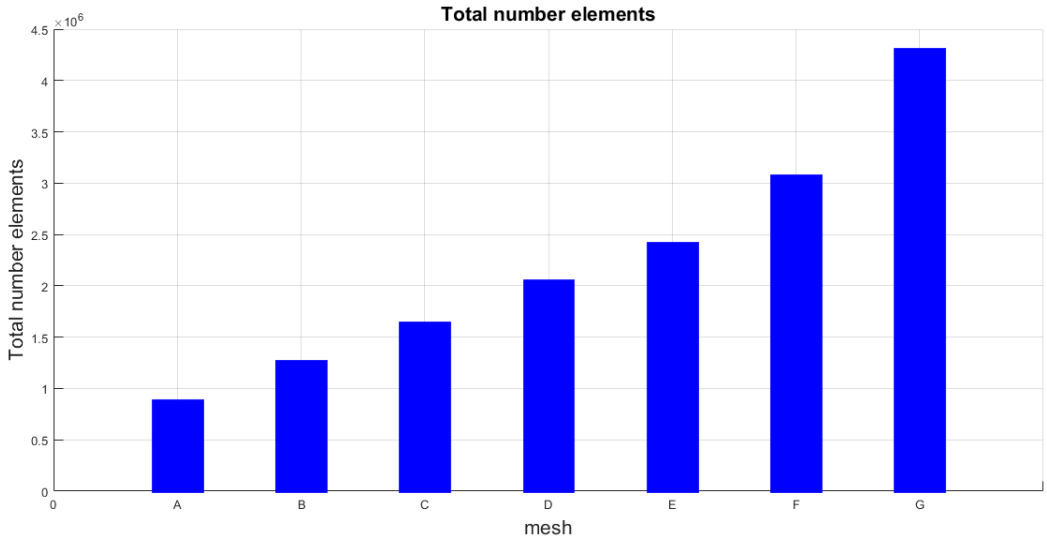

Chart 3.1 Total number elements

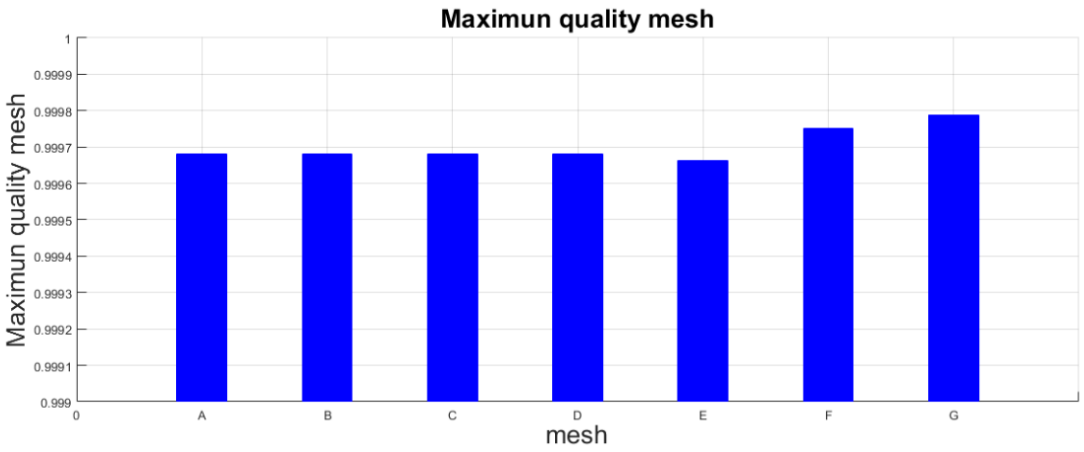

Chart 3.2 Maximum quality mesh

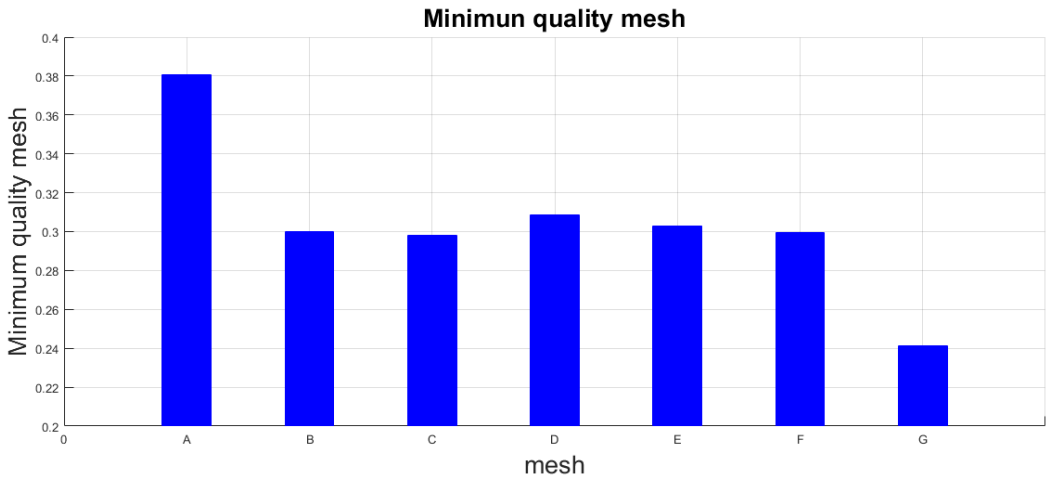

Chart 3.3 Minimum quality mesh

3.2 **Computational Fluid Dynamic steady simulation**

The computation analysis was performed by making a Computational Fluid Dynamics steady simulation for each mesh with the software FLUENT 14.5 of ANSYS.

The set parameters for each simulation are the following ones:

- a steady flow conditions,
- a Newtonian blood rheological model,
- a viscous laminar model for the flow motion field,
- blood as material for the fluid, with a value for its density of 1060 $^{Kg}/_{m^3}$ and a value for its viscosity of 0.0035 $^{N*s}/_{m^3}$, as happens in the case of Ht of 43%,
- the boundary conditions for each part were: velocity type for the inlet, whose magnitude was taken to be 0.29 $^{m}/_{s}$ for inferior vena cava and 0.192 $^{m}/_{s}$ for the superior vena cava. Whereas to simulated the effect of the pulmonary arterial load, a pressure difference equal to 0 mmHg for RPA and LPA was imposed.
- no-slip condition and rigid behaviour for the wall,
- the solution methods were second order for pressure and second order upwind for the momentum,
- the solution controls were set to 0.7 for the pressure and 0.3 for the moment,
- the residuals for reaching the convergence criterion were set to be 10^{-4},
- the motion field and its variables were initialized at 0.

For each mesh, the *computational time* (also called "running time") was evaluated; that is the length of time required to perform a computational process, and in this case, to measure the time that each mesh takes to get the convergence.

The bar chart below demonstrates it for each mesh.

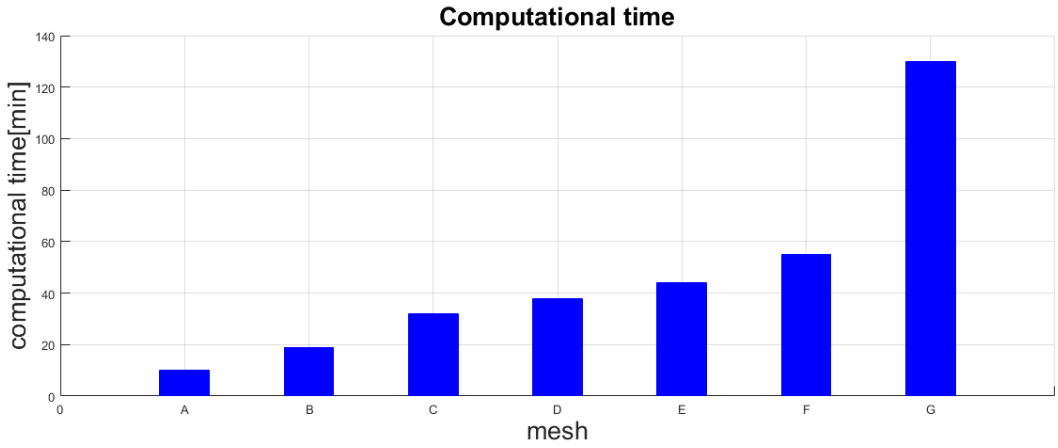

Chart 3.4 Computational time

3.2.1 *Pre-processing*

After the steady simulation is made, it is necessary to calculate some parameters to understand how the flow develops through the vessels, in particular the mid and maximum value of velocity magnitude and the maximum, mid and minimum value of WSS (wall shear stress).

The average velocity magnitude was calculated through an area-weighted method in four different iso-surfaces that are situated at a distance of approximately ten diameters from the origin of the geometrical model, in correspondence to the arteries and venas. The maximum velocity was evaluated on facets which are part of this iso-surface. Whereas the WSS was evaluated at the central zone of the wall that includes the bifurcation area that extends for about 10 diameters.

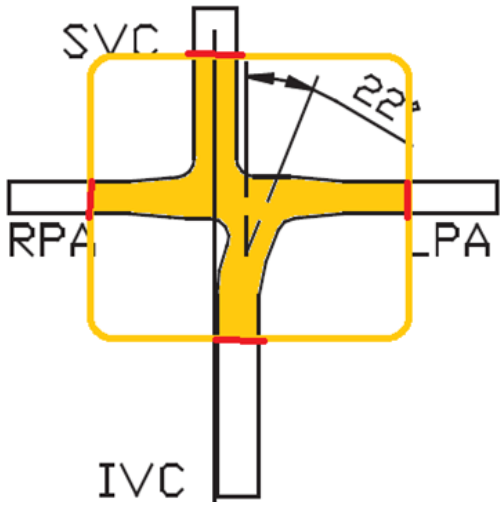

Figure 3.2 Visualisation of iso-surface and wall

In the figure 3.2 one can observe the yellow part that indicates where the WSS was calculated, and the small red segment that indicate where the velocity magnitude was calculated.

To select the part of the wall - where the WSS was calculated, it must satisfy the following ranges of coordinates (that were found on FLUENT). The x-coordinate must include a range of value between -0.12 and 0.12. The y-coordinate must also follow this range parameter,, whereas the z-coordinate must be within -0.006 and 0.006.

The coordinates of the velocity were calculated in the same manner: for the SVC iso-surface and IVC iso-surface, the y-coordinates must be equal respectively to 0.12 and -0.12 respectively, while for RPA and LPA iso-surfaces, the x-coordinates must be equal respectively to -0.12 and 0.12 respectively.

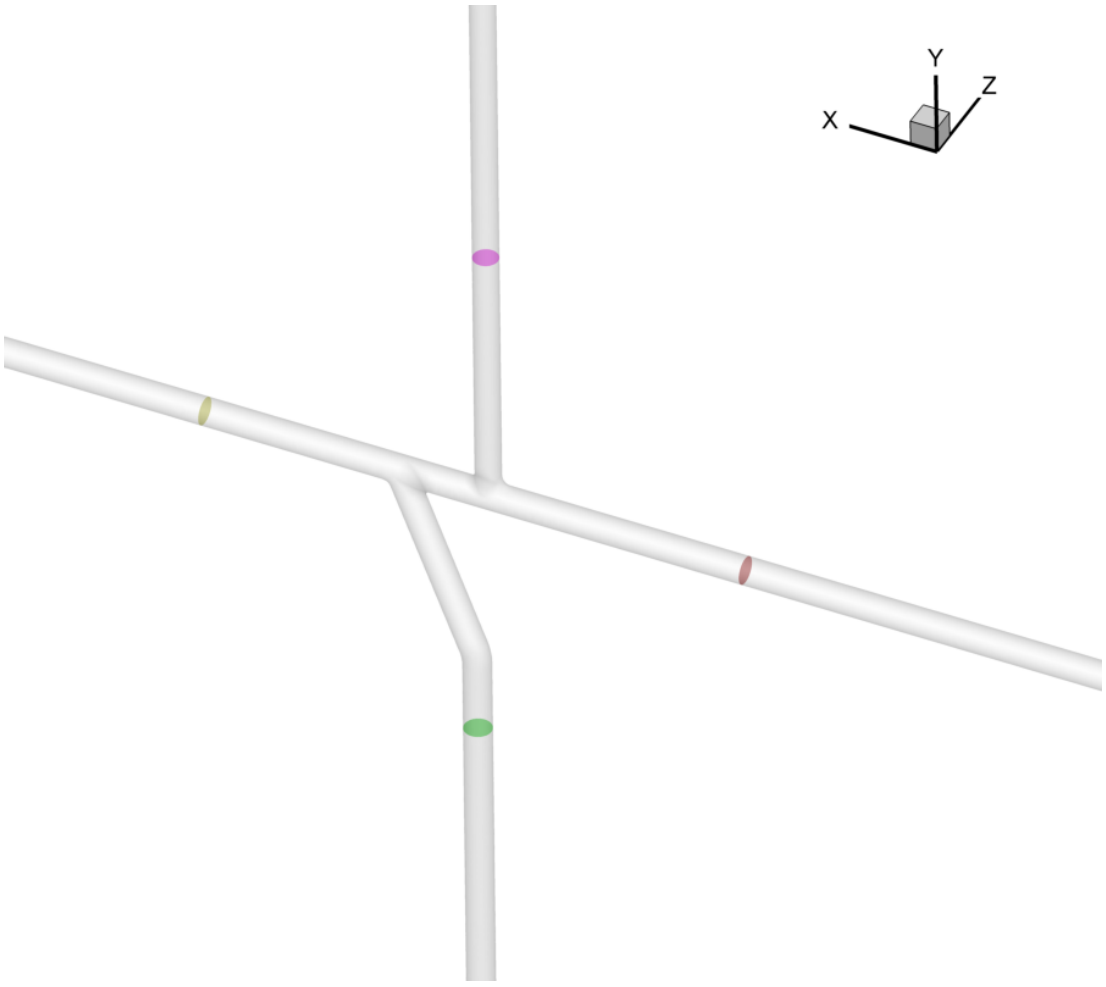

Figure 3.3 Image Model with TecPlot

In order to analyse the results of the sensitivity analysis, all values obtained for each mesh were compared to their percentage differences, as showed in the follows graphics where the curves are presented. Whereas, the bar charts present the maximum, minimum and mid values of velocity and WSS for each mesh.

- Maximum WSS

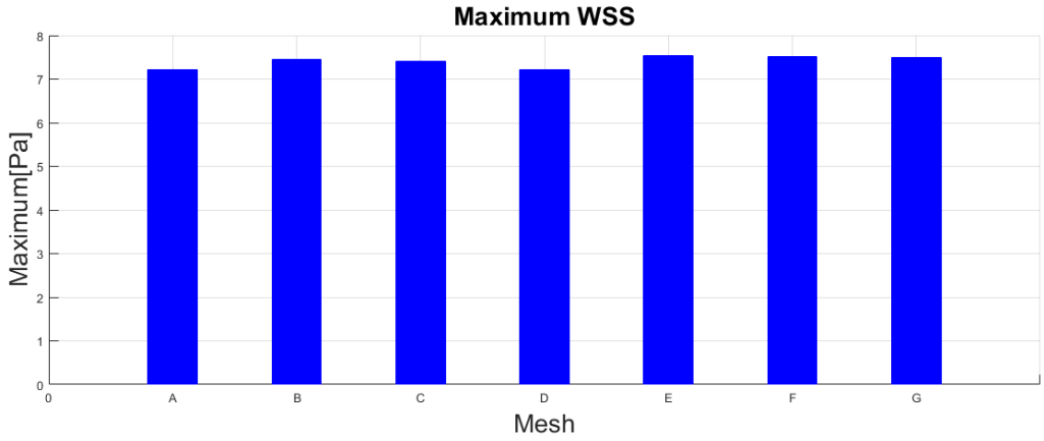

Chart 3.5 Maximum WSS

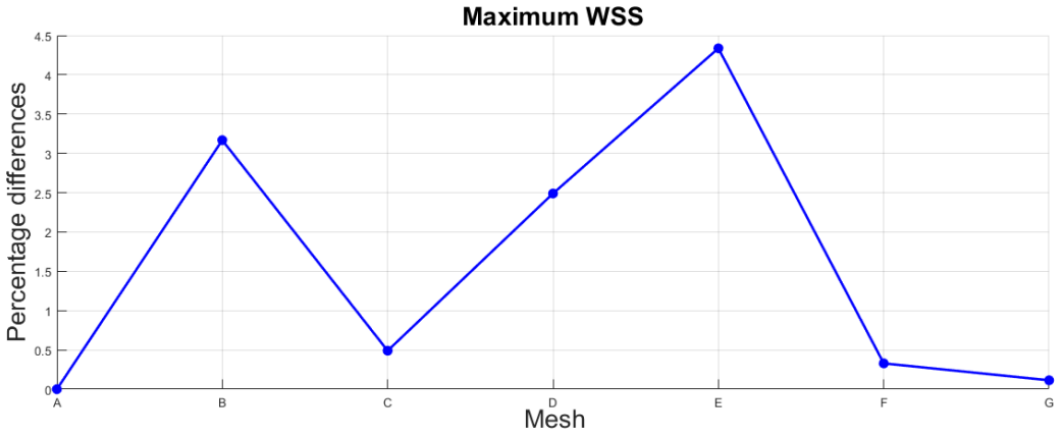

Chart 3.6 Maximum WSS

For example, one can note that the percentage difference between the mesh G and the mesh F is less than 1%, hence one can deduce that the mesh F gives accurate results as those given by the mesh G.

- Minimum WSS

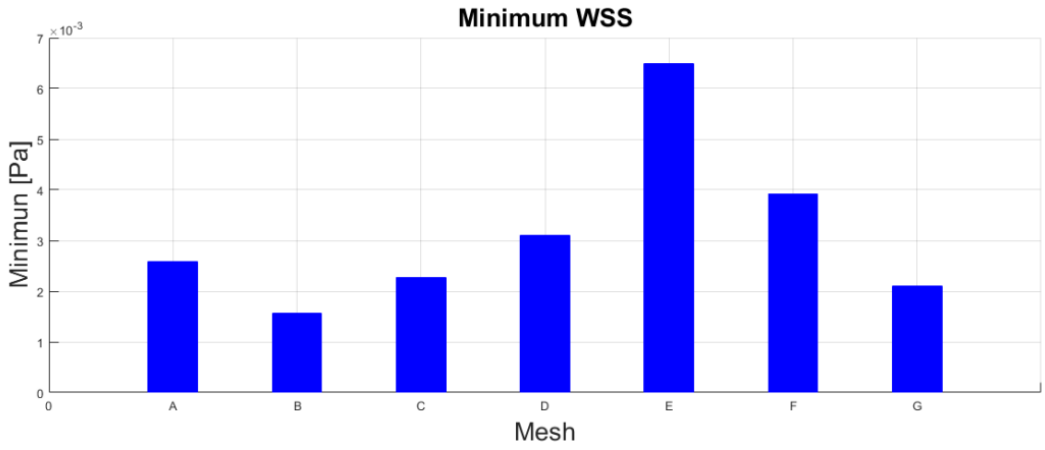

Chart 3.7 Minimum WSS

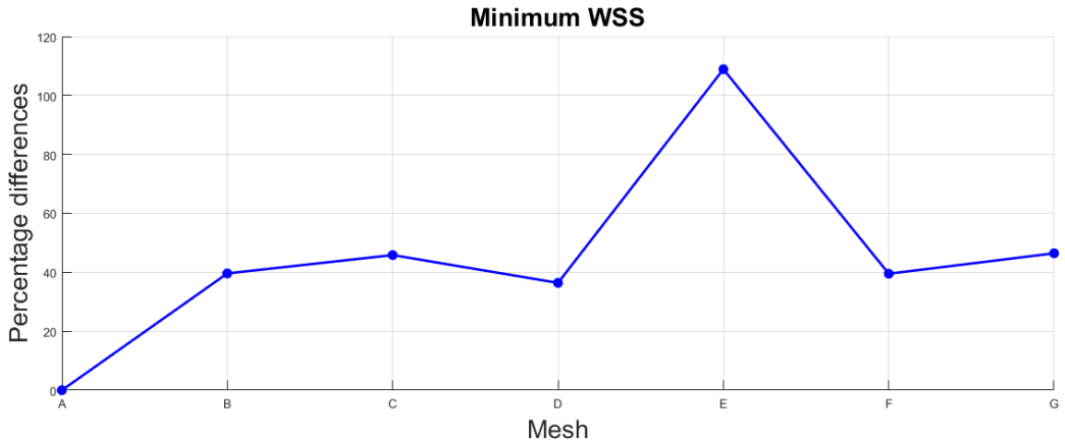

Chart 3.8 Minimum WSS

- Average WSS

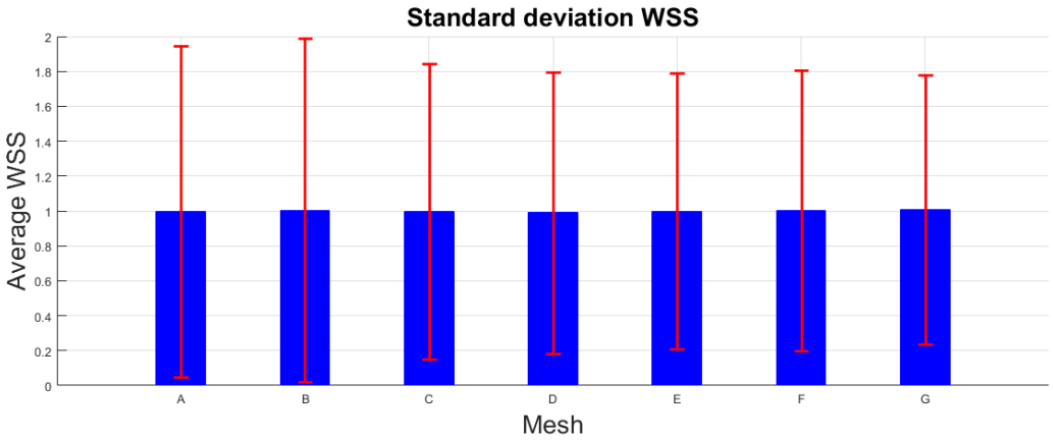

Chart 3.9 Standard deviation WSS

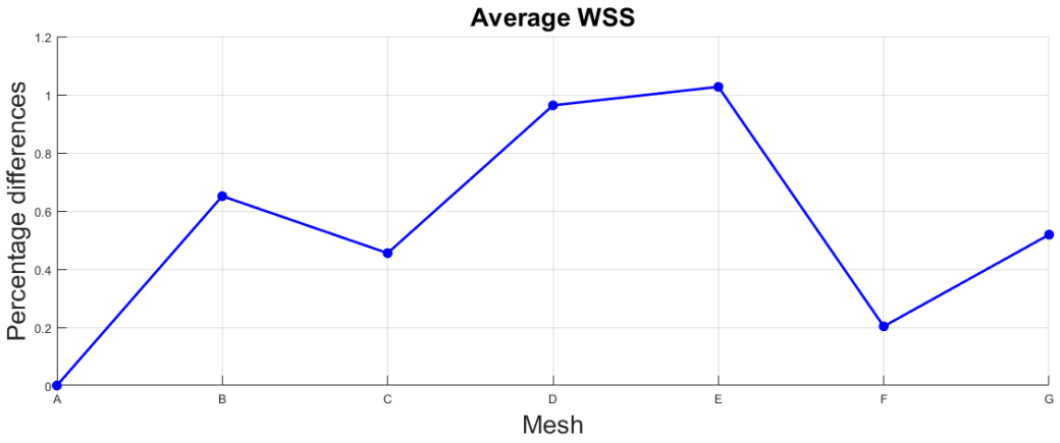

Chart 3.10 Average WSS

- Maximum velocity in inferior vena cava (IVC)

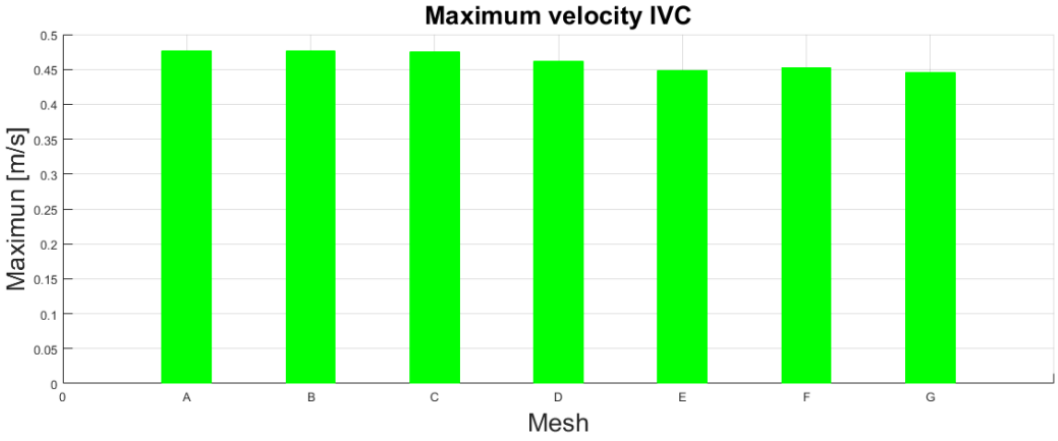

Chart 3.11 Maximum velocity IVC

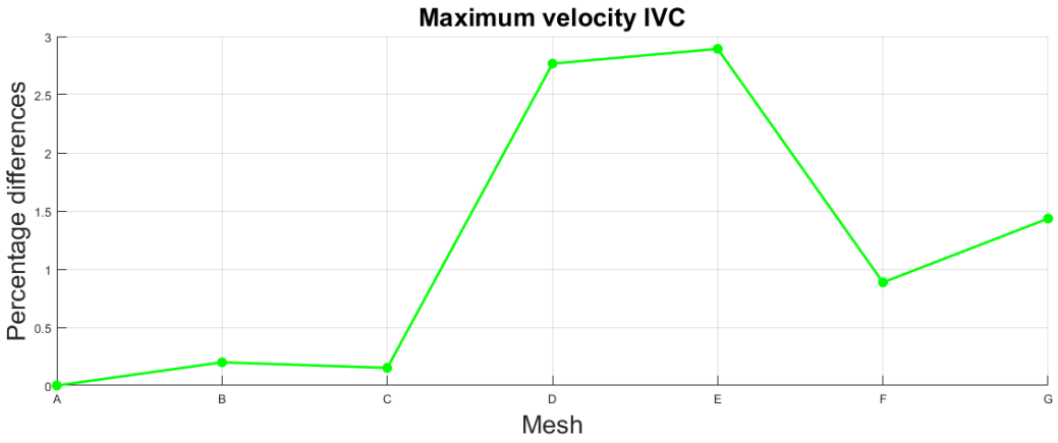

Chart 3.12 Maximum velocity IVC

- Average velocity in inferior vena cava (IVC)

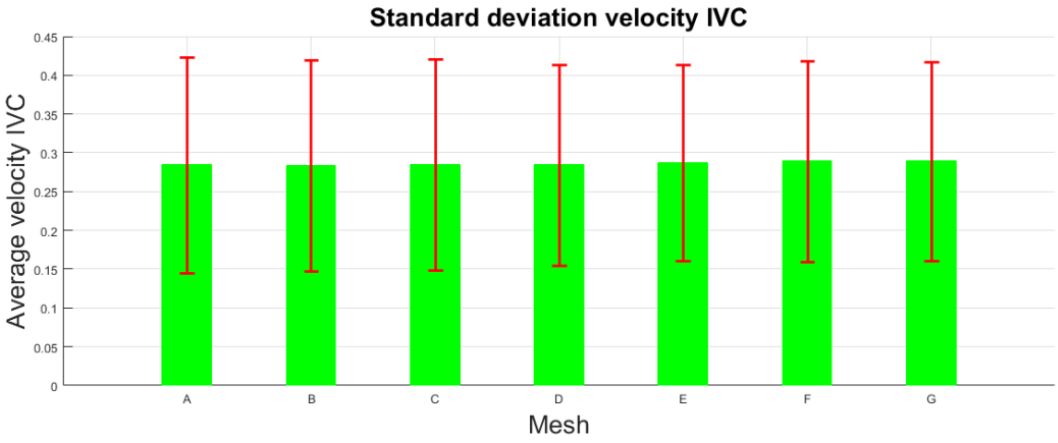

Chart 3.13 Standard deviation velocity IVC

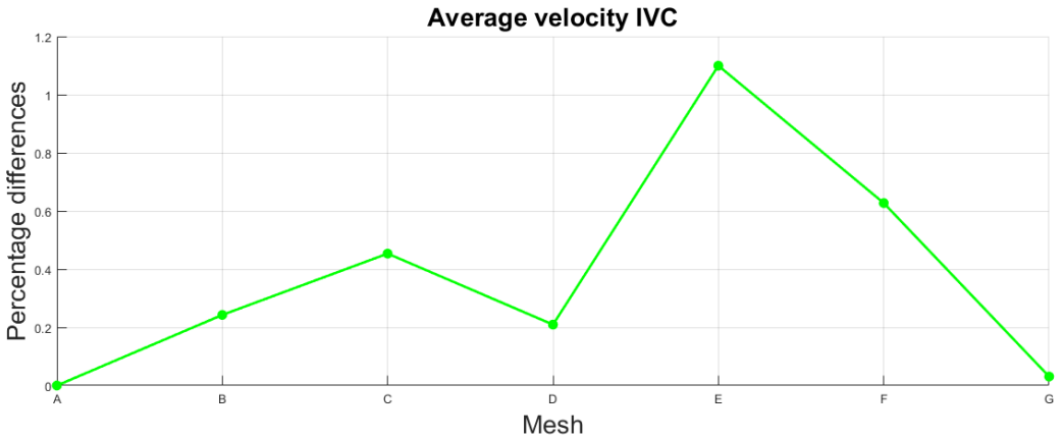

Chart 3.14 Average velocity IVC

- Maximun velocity in superior vena cava (SVC)

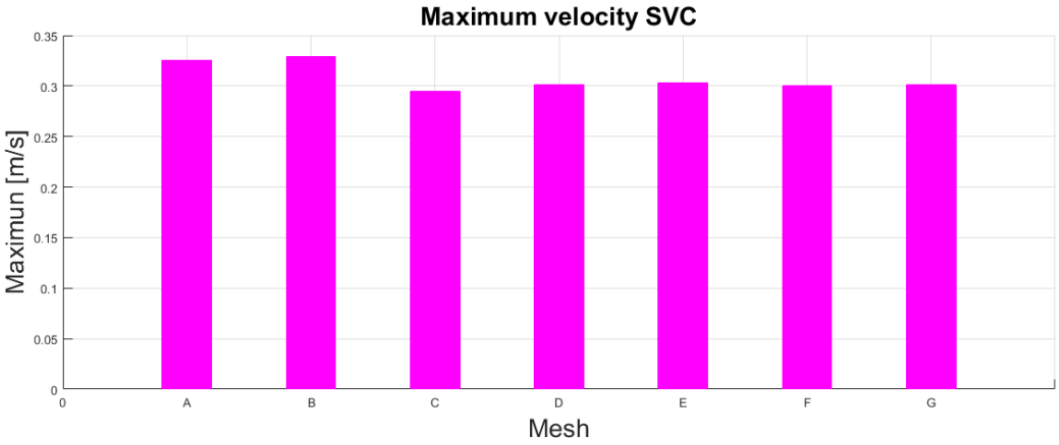

Chart 3.15 Maximum velocity SVC

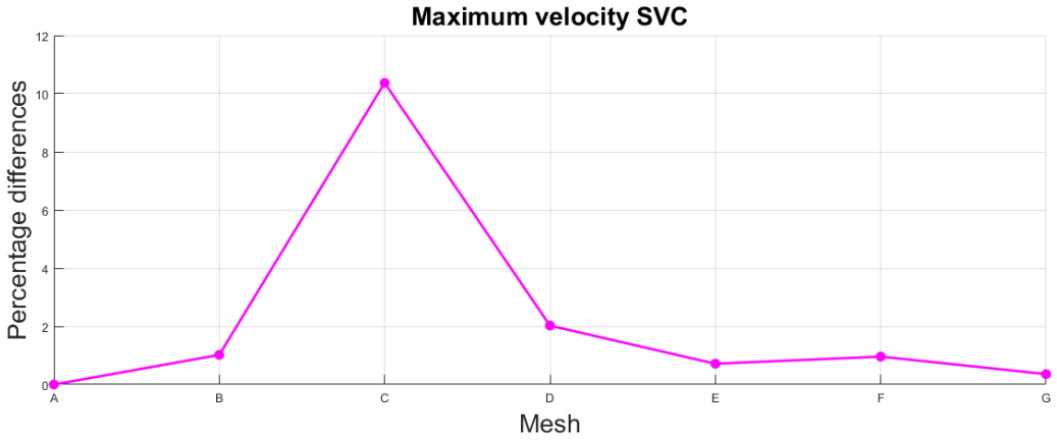

Chart 3.16 Maximum velocity SVC

- Average velocity in superior vena cava (SVC)

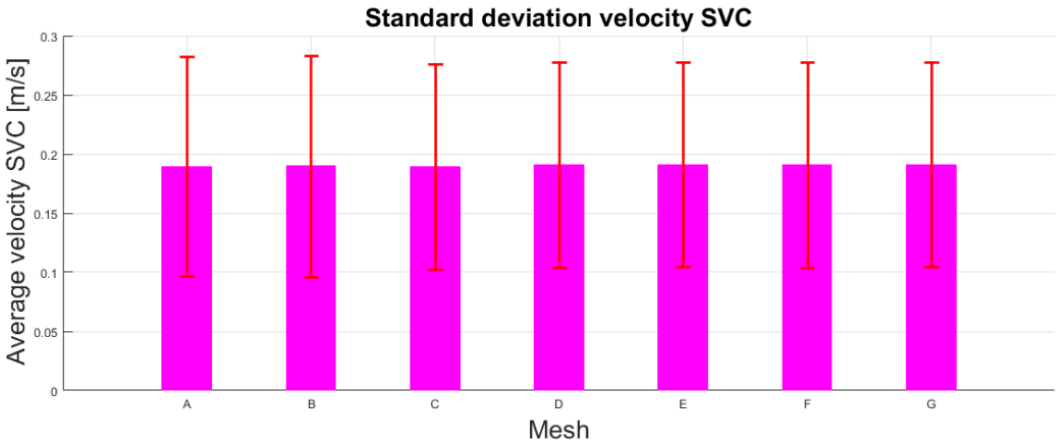

Chart 3.17Standard deviation velocity SVC

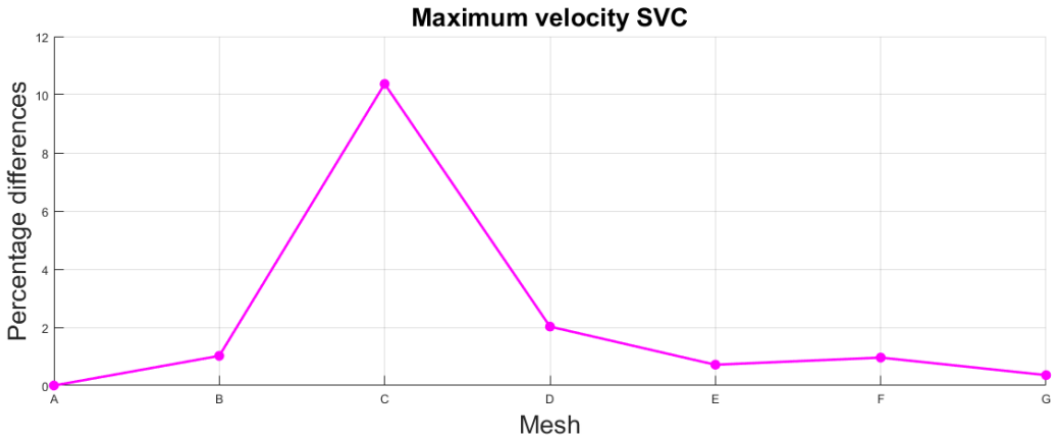

Chart 3.18 Maximum velocity SVC

- Maximum velocity in right pulmonary artery (RPA)

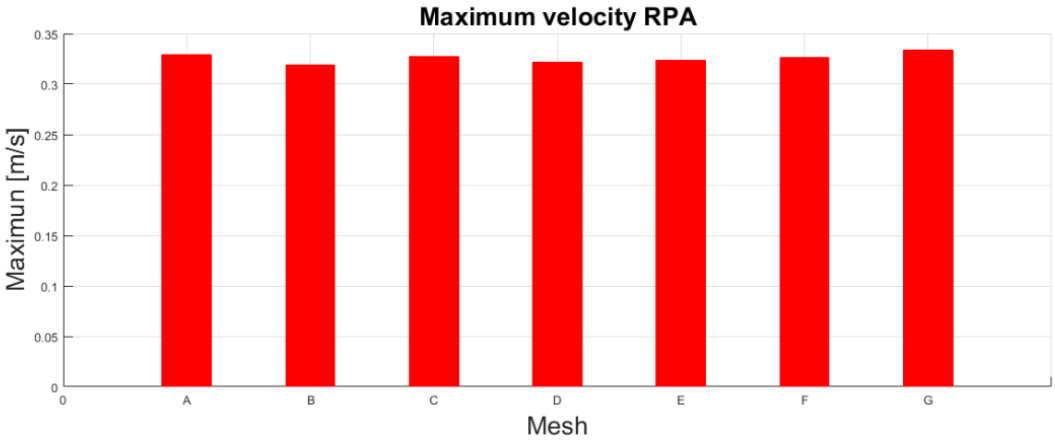

Chart 3.19 Maximum velocity RPA

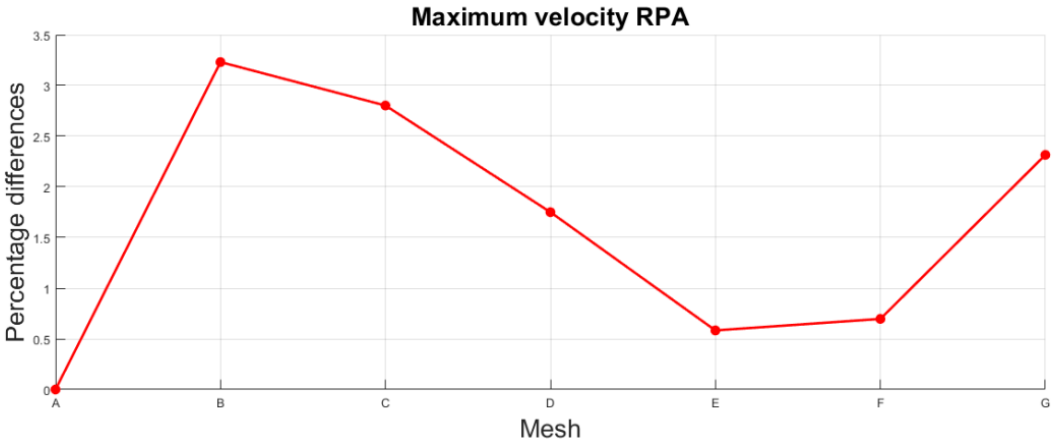

Chart 3.20 Maximum velocity RPA

- Average velocity in right pulmonary artery

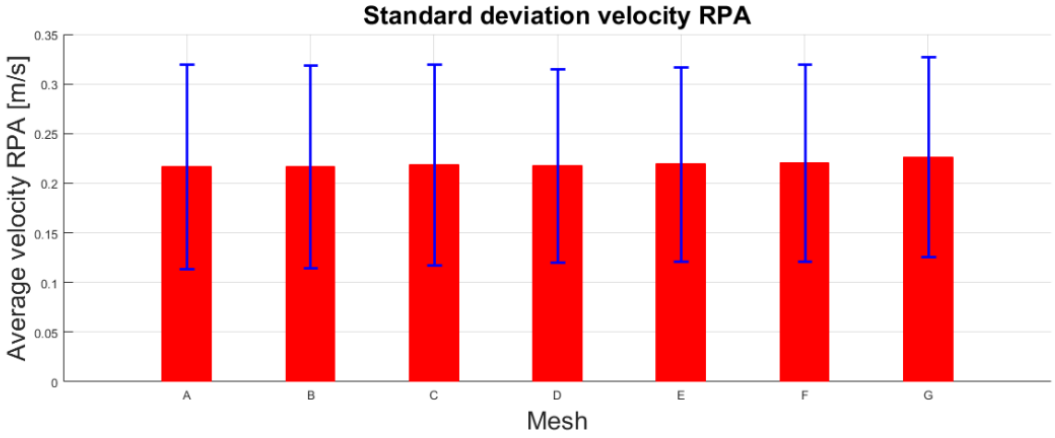

Chart 3.21 Standard deviation velocity RPA

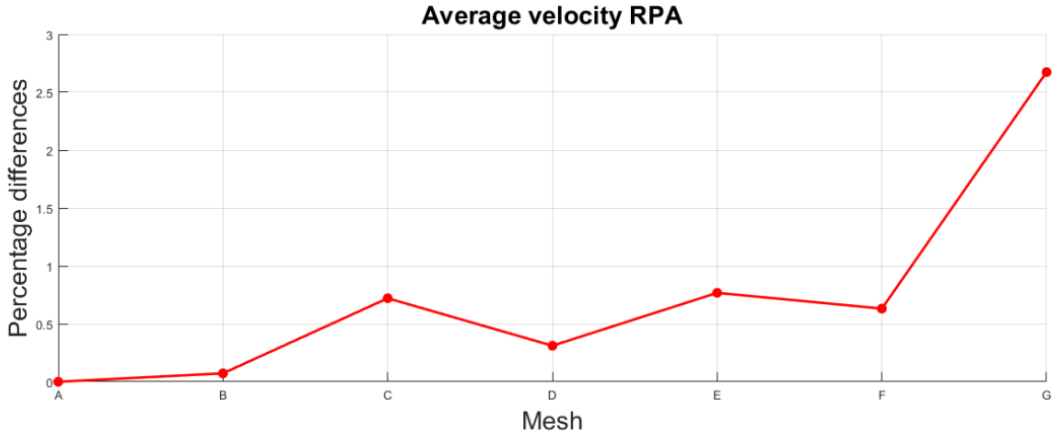

Chart 3.22 Average velocity RPA

- Maximum velocity in left pulmonary artery (LPA)

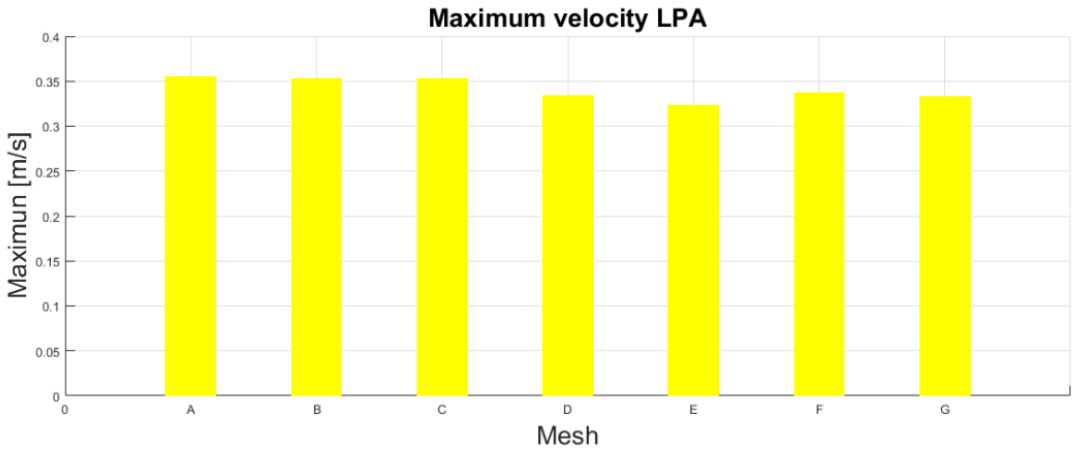

Chart 3.23 Maximum velocity LPA

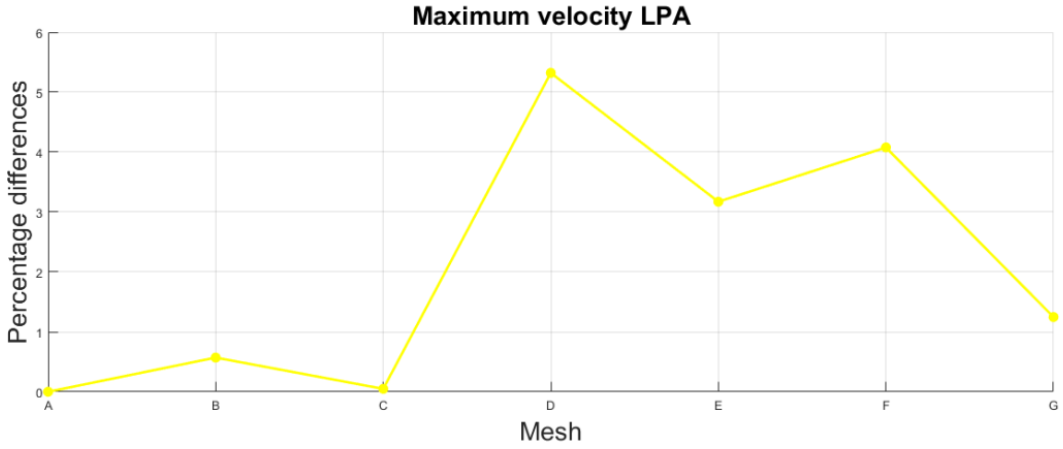

Chart 3.24 Maximum velocity LPA

- Average velocity in left pulmonary artery

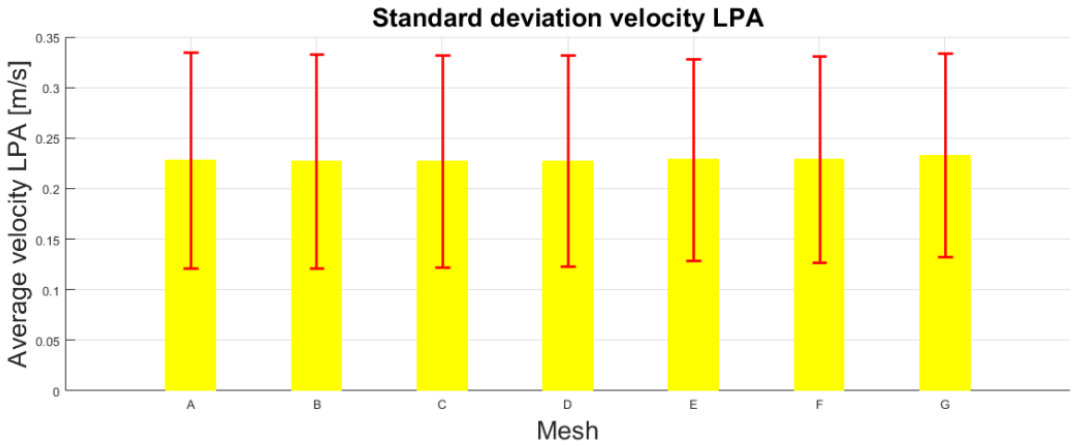

Chart 3.25 Standard deviation velocity LPA

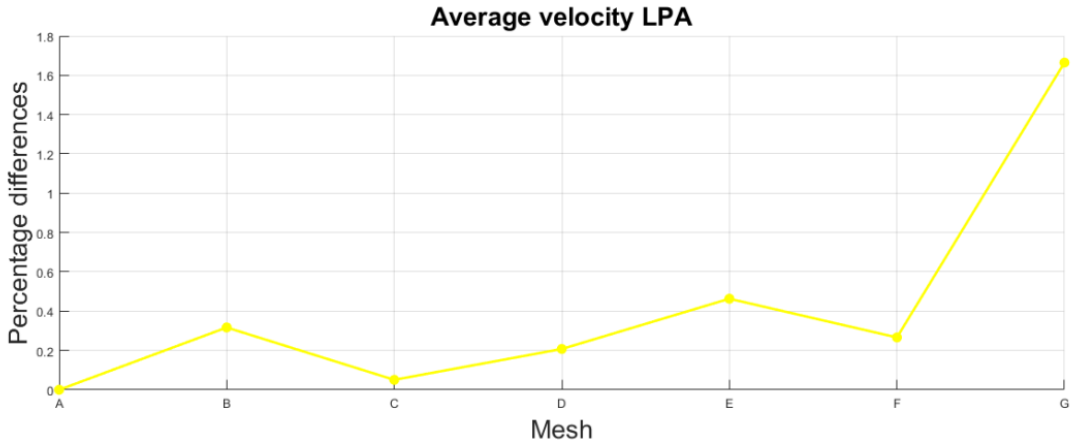

Chart 3.26 Average velocity LPA

In order to choose the best mesh, it is also necessary to proceed with the calculation of hydraulic losses which will be seen in the next section.

3.3 **Energy losses in steady simulation**

Increased energy loss in the circulation elicits genetic and biochemical changes in the myocardium that result in what is termed ventricular remodelling. As mechanical stresses and resultant energy loss increase, or as lesions persist over longer periods of time, the changes occurring in ventricular remodelling themselves can become detrimental to the heart, be it due to excess *hypertrophy*, *marked dilatation*, or *myocardial fibrosis*.

In our research, the main goal was precisely to assess the hydraulic losses through computational studies on our model, to understand how efficient our solution can be and to understand what are the points on which the researches can work on in the future to improve the connection between the vessels and thus improve the surgical technique.

The end result will be achieved when the surgery will allow the patient (child) to have a regular organic growth, will allow him to perform all normal activities at the physical level, and maintain a lifestyle as close as possible to the life of a patient without pathology.

By using this strategy, pediatric cardiologists and cardiac surgeons could simulate different TCPC surgical options and obtain an estimate of postoperative connection power losses.

This important parameter: 'hydraulic losses' that will be calculated below, have already been taken into account in the construction of the model and in the choice of parameters to be set, as can be seen in the chapter on geometry. In fact, the design of the TCPC plays an important role in the fluid patterns and the energetic efficiency of the anastomotic region.

Furthermore, turbulent losses were eliminated considering smoothing solid surfaces that remove sharp corners and bends from the flow geometry, as these can cause flow to destabilize at lower Reynolds numbers.

In the various studies that were made in the past, different methods to calculate energy loss within the TCPC were used, such as the control volume approach and

viscous dissipations methods. The viscous dissipation analysis is based on the velocity gradient, which is very sensitive to the grid size and shape.

In our research work the control volume approach was used, because as mentioned by Ryu et al. (2001) [**44**] comparing the kinetic energy loss term to the pressure loss term in the control volume energy loss calculation -shows that most of the energy loss is caused by the pressure drop. The kinetic energy loss is relatively small. As the pressure drives the blood through the TCPC model.

The follow equation shows the control volume for energy loss computation:

$$E_{loss} = -\int_{CS} [p_{static} + \frac{1}{2}\rho u_j u_j]\, u_i n_i dA \qquad \textbf{3.1}$$

Where:

- E_{loss} is the rate of energy consumption within the control volume,
- CS is the control surface,
- u_i defines the components of the velocity vector,
- n_i represents the components of the outward surface normal vector of the control surface,
- dA is the area of the differential control surface,
- p_{static} is the static pressure.

In vitro experiments provide only limited information about the pressure and velocity of the flow at the inlet and outlets of the TCPC domain. So a simplified version of equation 3.2 was introduced to calculate energy loss with this limited information:

$$E_{loss} = -\sum (p_{static} + \frac{1}{2}\rho u_j u_j) u_i n_i A_i =$$

$$= \sum P_{total} Q_{inlet} - \sum P_{total} Q_{outlet} \qquad \textbf{3.2}$$

Based on the following assumption:

$$P_{total} = p_{static} + \frac{1}{2}\rho u_i u_i\,, \quad u_i = \frac{Q_i}{A_i}$$

Where Q_i represents the flow rate at an inlet or an outlet. Thus, the equation reduces the information needed for the energy calculation of the total pressure values and flow rates at the inlets and outlets.

For simplicity, in our case the total energy losses was calculated adding the energy in the inlet section and subtracting the energy in the outlet section, through the equation 3.3:

$$E_{loss} = \left(\frac{1}{2}\rho v_{SVC}^2 + p_{SVC}\right) + \left(\frac{1}{2}\rho v_{IVC}^2 + p_{IVC}\right) - \left(\frac{1}{2}\rho v_{RPA}^2 + p_{RPA}\right) - \left(\frac{1}{2}\rho v_{LPA}^2 + p_{LPA}\right) \quad \textbf{3.3}$$

The two sections of inlet and the two sections of outlet were used, considering the iso-surface already used in the sensitivity analysis.

All the parameters, present in the equation 3.3 were obtained on the software Fluent, that permits to find the static pressure end the magnitude velocity of these surface.

The parameters were extracted through a file ASCII by Fluent and were read with a script of Matlab to implement the above equation.

In the steady condition, this work was made for all seven meshes, to analyze the change of the energy losses with the change of number of cells that makes up the mesh.

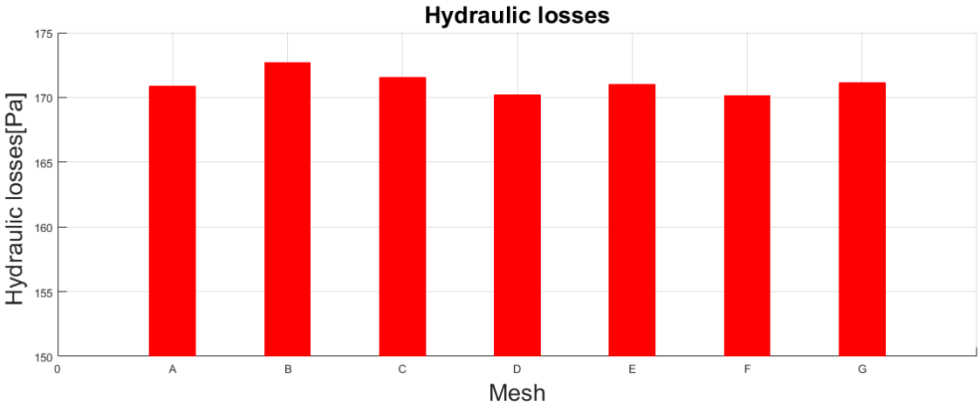

Chart 3.27 Hydraulic losses

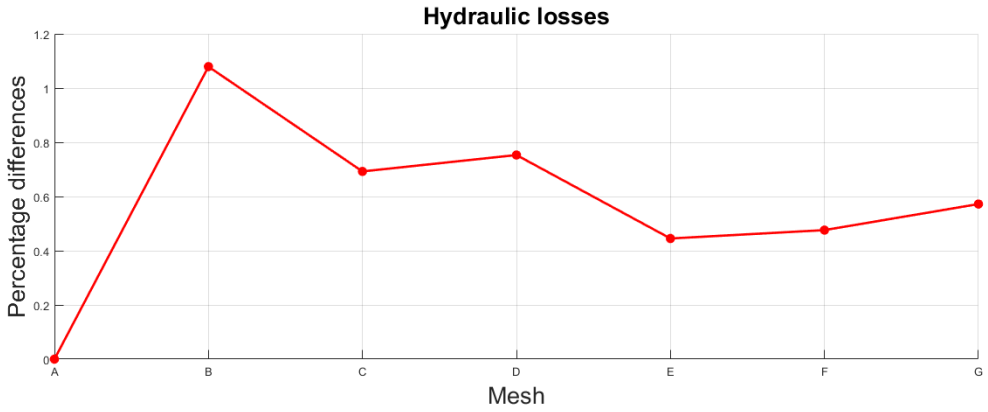

Chart 3.28 Percentage differences in hydraulic losses

3.4 **Conclusion**

According to the results, the mesh F with 3.076.423 elements was chosen. It is considered the 'best' of all because it allows to achieve the right balance between *accuracy solution*, *computational costs* and *hydraulic losses*. It has the necessary spatial resolution for this fluid dynamic application, that is this mesh, as it can be seen from the calculation of the percentage differences (plotted) that gives accurate results almost as much as the mesh G, that is composed of several elements (4.564.381), yet does takes less time during the simulations.

In regards to the hydraulic losses, it can be observed in the chart 3.27 that the mesh F gives the most efficient results because it produces, among all the meshes, the lowest hydraulic losses.

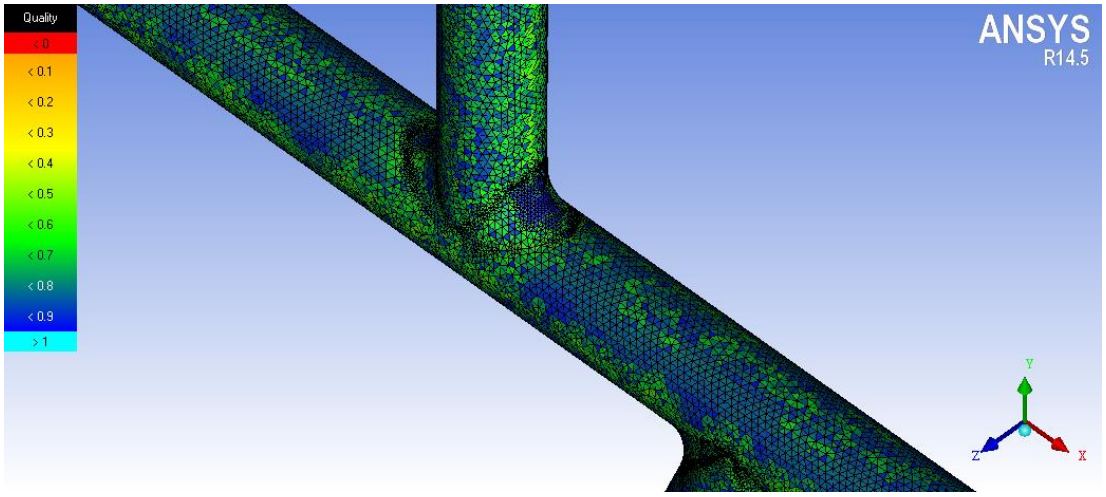

Figure 3.11 Central zone of mesh F

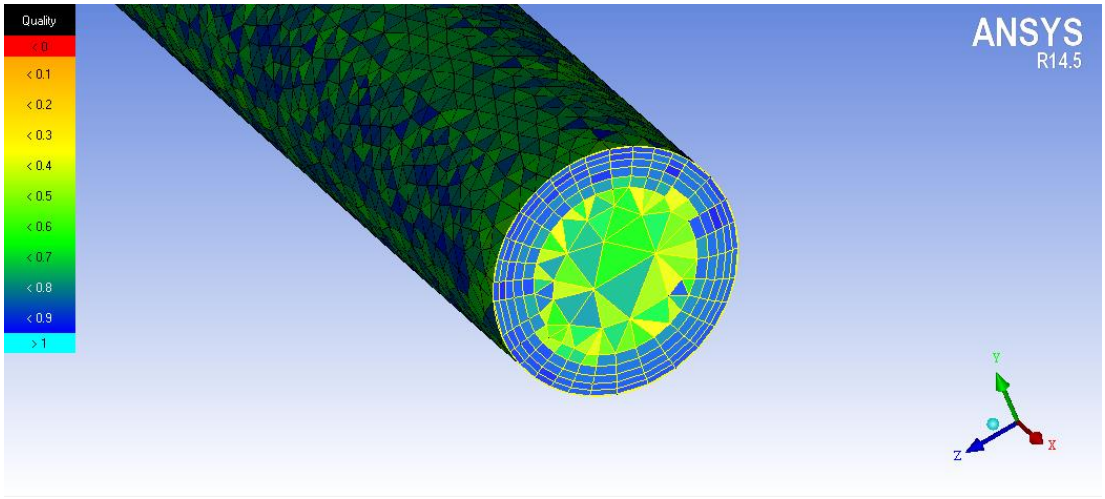

Figure 3.12 Outlet of mesh F

CHAPTER 4
COMPUTATIONAL FLUID DYNAMIC (CFD) ANALYSIS

This chapter is divided into four parts, in order to explain the steps before performing the unsteady simulation, and the role of some hemodynamic quantities of interest, in regards to the post-processing analysis. The first part briefly explains how the numeric algorithm based on the finite volume elements method (FVM) works,. The second section describes the boundary conditions set to perform the unsteady simulations. It demonstrated: the flow rate waveforms that were used to set the inlet of the model, the number of time steps, the duration of each one and last, the boundary conditions for the wall. The third paragraph concerns the transient cycles. It points out the number of transient cycles performed to initialize the flow and eliminate the influence of the initial conditions. Here, two different variables are considered: WSS, velocity magnitude and the percentage difference between a cycle and the previous one are calculated. The last part illustrates the hemodynamic descriptors of interest, which will be evaluated on our geometrical model in chapter 5, when analysing the post-processing results. These quantities can be divided into two main groups, similar to the results, we will see that: some are related to the wall analysis (*TAWSS*, *OSI*, *RRT*) and others are related to the bulk flow analysis (*LNH*). A variety of hemodynamic descriptors have been proposed to analyse CFD results. The results analysis was performed under two kinds of approach: the Eulerian one and the Lagrangian one.

4.1 **The CFD method**

After having performed the sensitivity analysis, the fluid domain was studied under *unsteady fluid conditions*, using the CFD solver Ansys Fluent 14.5.

Computational Fluid Dynamics provides a quantitative prediction of fluid flows by means of :

- mathematical modelling (partial differential equations),
- numerical methods (discretization and solution techniques),
- software tools (solvers, pre- and post-processing utilities).

Therefore, during pre-processing, CFD is based on a series of steps: the definition of the geometry of the problem, spatial discretization of the volume of interest into a finite set of control volumes, the definition of physical modelling (in fact numerical methods are applied to solve the equation) and the definition of boundary condition. Afterwards, the simulation is started and the equations are solved iteratively as a transient (in our case). Finally, a post-processor is used for the analysis and visualization of the resulting solution.

The CFD solver ANSYS Fluent is based on the finite volume methods (FVM) [**45**], whose process steps start with the substitution of the continuous domain with a discrete one, having a sufficient spatial resolution, which is the mesh size. Then, the centre of each cell of the grid is associated with discrete values for the variables of interest, expressing them as average values, because they are linked together in the two fundamental mechanical laws, which govern the fluid behaviour: the conservation of mass equation for a Newtonian incompressible fluid [**45**]:

$$\frac{\partial P}{\partial t}\,\nabla\,(\rho v) = 0 \qquad \textbf{4.1}$$

and the conservation of momentum equation:

$$\frac{\partial v}{\partial t} + v\,\cdot\nabla v = -\frac{1}{\rho}\nabla p + \upsilon\nabla^2 v \qquad \textbf{4.2}$$

These second orders, non-linear and partial derivatives equations are integrated and solved in each grid volume cell, which is a volume box of control, by the solver through several iterations. In sum, these equations are integrated over the fluid domain of interest, which is the central part of the model included between the choices coordinates in the previous chapter. These integral equations are then conversed into a system of algebraic equations, whose solutions are calculated through an iterative method, based on checking the convergence criteria: the residuals set to 10^{-4} for the continuity and the three velocity components (x-velocity, y-velocity and z-velocity) for each time step. Namely, a time step is the incremental change in time for which the equations have been solved. Residuals give a measure of the deviation from the correct solution: the lower the residual, the more accurate is the solution. However, this method does not lead to an analytical solution for the equations, but to an approximate computer-based solution. In general, convergence is reached when changes in the solution from one iteration towards the previous one are negligible, overall property conservation is guaranteed and quantities of interest have steady values, iteration after iteration. Values for all the variables at the end of a time step are the initial values for the following one, until the convergence is reached. This happens when the following expression is true:

$$\frac{x_{K+1} - x_K}{x_K} < \varepsilon \qquad \textbf{4.3}$$

Where ε is a reference value, which is set as the residual value. This expression enables to find a reasonable CFD solution. When the value for the k+1-th iteration differs from the one for the k-th iteration of a lower enough value, which is defined according to the necessary accuracy of the application, the solution is converged.

4.2 **Unsteady simulation: setting parameters**

To simulate the behaviour of blood flow under *unsteady conditions*, some boundary conditions have been imposed. A time dependent flow rate profile present in literature on the subject was imposed at the inlet. They are found in the article by Ajit P. Yoganathan e al (2012) [**46**].

These waveforms are related to the venas cave (IVC and SVC) and the pulmonary arteries (LPA and RPA), as can be seen below.

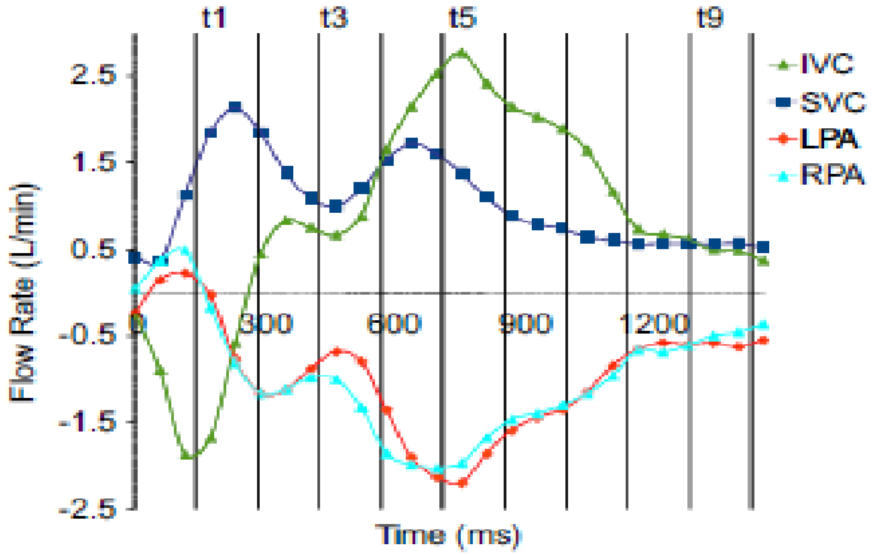

Figure 4.1 Pulsatile flow waveform

There is reverse flow in IVC and PAs at the beginning of the cardiac cycle.

The IVC flow then increases through the rest of the cycle and reaches its maximum flow in the middle of the cycle. SVC flow has less fluctuations through the cycle. At instant t1, reverse flow is observed in IVC and the pulmonary arteries. The SVC flow is dominant and has penetrated significantly into the IVC baffle.

At t3, the SVC flow rate is still higher than the IVC flow rate and most of the IVC flow is directed to RPA. At t5, both IVC and SVC flows are nearly at their peak and are distributed to the two Pas uniformly. At t9, IVC and SVC flow rates are equal, effective flow mixing is observed in the baffle, and a uniform flow distribution to PAs can be observed.

Boundary condition of unsteady simulation

The numerical algorithm is the same as in the steady state simulations for the sensitivity analysis, but a time dependent flow rate profile for the inlet was set as boundary conditions for the unsteady simulation.

Flow rate profile waveforms

These flow rate profile waveforms have been reconstructed through a script in Matlab. To reconstruct these waveforms the following parameters were set:

- 1500 *ms* as the maximum value for the x coordinate,
- 3 *l/min* as the maximum value for the y coordinate, (0.00005 $m^3/_s$).

In order to be comparable with the flow conditions in the article, the inlet flow waveforms SVC and IVC were scaled thought the coefficient to have a value of Reynolds numbers equal to 382 and 321, respectively. The values of this coefficient number are 0,6407 for the IVC waveform and 0,63926 for the SVC waveform. This was done thanks to the UDF (User-Defined-Function) that is reported in the appendix section and was obtained by an interpolation of some samples, given by [**47**]with a Fourier series:

$$f(t) = a_0 + \sum_{n=1}^{N} [a_n \cos(2\pi nt) + b_n \sin(2\pi nt)] \quad \textbf{4.4}$$

Where:

- a_0 is the mean value of velocity,
- a_n are the Fourier coefficients,
- N is the number of coefficients that are used to reconstruct the wave form.

The waveforms obtained are shown below:

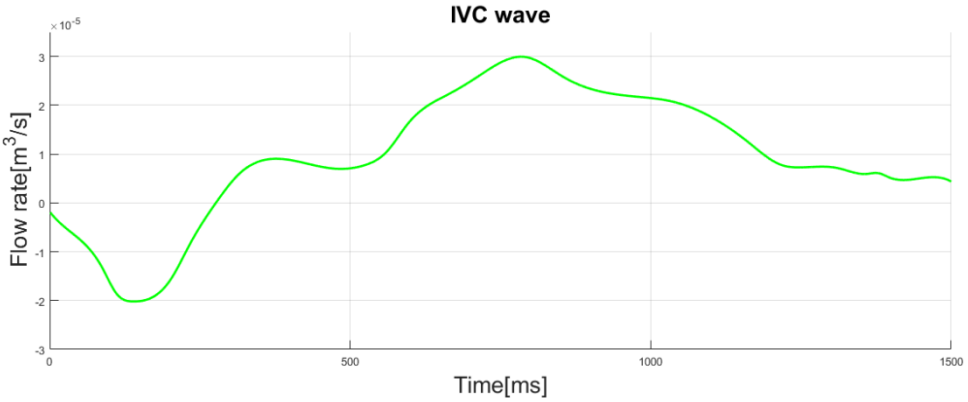

Chart 4.1 IVC wave

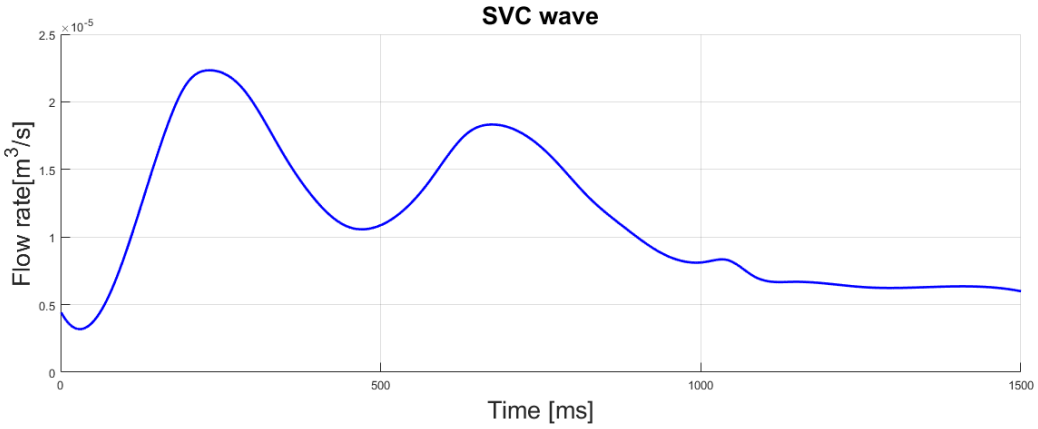

Chart 4.2 SVC wave

The cardiac cycle was subdivided into time steps in order to perform the unsteady simulation. It is a compromise between the need to reach the convergence of the simulation in a reasonable period of time, and the need for accuracy in the discretization of the flow rate. Therefore, 0.002 s long was chosen as the single time step, and the whole period was composed of 750 time steps. The arterial and pulmonary walls were assumed rigid and the shear condition was imposed no slip. Thus, the fluid will have zero velocity relative to the boundary.

For the outlet, in the right and left pulmonary artery is set a value of pressure equal to 0.

4.3 **Transient cycles**

Four cardiac cycles are simulated to initialize the flow field and to achieve a solution independent from the initial conditions. WSS of the central zone and velocity magnitude of the four iso-surface were evaluated at the end of each cycle to establish if a sufficient accuracy level was reached. These was deducted by calculating their percentage difference in one cycle towards the previous one. In particular, the cyclic convergence criterion, adopted, accepts a relative percentage error of less than 1%.

The tables below show the percentage differences of the considered parameters between the different cycles.

	WSS max [*Pa*]	**WSS mid [*Pa*]**	**WSS min [*Pa*]**
Cycle 1	0	0	0
Cycle 2	-0,123306885	0,010175076	-40,83282619
Cycle 3	0,070395746	0,018980819	-19,99242376
Cycle 4	-0,032351536	0,019989677	2,514774027

Table 4.1 Percentage difference of WSS maximum, minimum and mid between cycles

	Average velocity_SVC [m/s]	**Average velocity_IVC [m/s]**	**Average velocity_RPA [m/s]**	**Average velocity_LPA [m/s]**
Cycle 1	0	0	0	0
Cycle 2	0,00719334	0,04708824	-0,1769399	0,14071701
Cycle 3	-0,0098795	-0,0235387	-0,0327034	0,02618273
Cycle 4	-0,0017388	0,04530820	0,00205109	0,01744844

Table 4.2 Percentage difference of average velocity of the 4 iso-surfaces between cycles

	Maximum velocity_SVC $[m/s]$	Maximum velocity_IVC $[m/s]$	Maximum velocity_RPA $[m/s]$	Maximum velocity_LPA $[m/s]$
Cycle 1	0	0	0	0
Cycle 2	-0,0058754	0,11827437	-0,0024677	-0,39033547
Cycle 3	-0,0123483	-0,0110563	-0,0161439	0,13819643
Cycle 4	0,00812165	0,02300126	0,00184293	0,01883872

Table 4.3 Percentage difference of maximum velocity of the 4 iso-surfaces between cycles

The CFD solution was calculated with Fluent 6.3 solver.

The computational time for each cardiac cycle is of approximately 22 hours using 8 processors in parallel.

At the end of the four cardiac cycles, the differences between these variables proved to be low enough for this application. Furthermore, information for wall and energy analysis were collected from the fifth cardiac cycle because the effects of the transient were negligible.

4.4 **Hemodynamic descriptor**

The study of cardiovascular flow is of great interest because of the role of hemodynamics in cardiovascular diseases. Abnormal hemodynamic produces abnormal stresses on the endothelial cells. The unfavourable hemodynamic environment is referred to the expression ‘disturbed flow’, it is used to imply mechanisms such as: the modulation of the friction forces at the vascular luminal surface and the consequence on endothelial functions. In the past the majority of the researches were mainly focused on Wall Shear Stress (WSS) which is defined as the force per unit area exerted by flowing blood on the endothelial cells lining the vessel lumen. This because it was used as a quantitative indicator of disturbed flow. In fact sites exposed to low and/or oscillating WSS might be vulnerable to development of atherosclerosis, intimal thickening and hyperplasia. But, on the other hand, the onset and the evolution of helical patterns in the arterial bulk flow could elicit atheroprotective fluid-wall interaction process, thus avoiding the onset of atherogenesis. A variety of hemodynamic descriptors has been proposed over the years to [**48**]:

- Reduce the inherent complexity of the four-dimensional blood flow fields;
- Simplify the understanding of the flow dynamics;
- Quantify hemodynamic disturbances as potential indicators of vascular wall dysfunction.

Descriptors with the capability of quantifying phenomena depending on the complexity of the blood flow in the bulk are of great interest as they can offer insight, complement, integrate and extend the information given by the WSS-based descriptors.

Eulerian approach

Current in vivo imaging techniques, such as phase-contrast magnetic resonance imaging, PC MRI, in vitro imaging techniques, like particle image velocimetry, and computational methods, which are used for quantifying blood flow, typically produce Eulerian velocity data as output. The velocity field itself has limited clinical relevance. Generally, the interest lies in the transport of the fluid or in the forces produced by the fluid motion [**48**], which can influence the entire surrounding

environmen. The advantages of Eulerian specifications about bulk flow quantities are mainly linked to this kind of approach for clinical applications, because of its immediateness. Indeed, Eulerian quantities have a simpler definition, allowing for real-time analysis and can give a picture of the entire flow field. Although it is often reasonable to infer the bulk fluid motion from inspection of the velocity data, a quantification of the flow structures in unsteady flows, particularly when the time history of the velocity field has also been taken into account, could be difficult and could lead to misinterpretations [**48**].

Lagrangian approach

Hemodynamic quantities, such as residence times of single fluid particles, particle deposition, and particle shear exposure, are usually evaluated according to Lagrangian specifications, because they rely on the dynamical path history of a fluid element, and because the Lagrangian characterization identifies the element by its position at some initial time. Hence, they differ from other hemodynamic quantities such as WSS, which are usually described through Eulerian specifications. Because a picture of the spatial distribution of these quantities is known at each instant of time, as an instance they are functions of position and time [**48**]. However, the required concentration of particles to model the physiological situation would present extreme computational demands: the concentrations make the computational cost of the particle motion modeling impossible. In sum, these limitations force leave no other option but to employ alternative approaches for the computation of meaningful path-dependent hemodynamic quantities for arterial models of blood flow. Among them, the statistical approach, consisting in extracting the relevant quantities from ensemble averages over a sufficient set of particles [**48**], seems to be the most cost-effective one.

If the Lagrangian approach, that allows to extract path dependent quantities tracking the fluid particle, is combined with visualization techniques, it will be particularly useful both for characterizing unsteady flow patterns and for highlighting important hemodynamic features. Particle traces offer three-dimensional visualization of flow patterns which have proven to be useful tools in order to investigate complex flow fields in vessels and in general, to reveal global

organization of the flow, thereby making it easier to detect by visual inspection of the relevant flow features and to understand the true fluid motion [**48**]. The definition of path dependent quantities allows the investigation of dynamical path histories and could offer a practical way to divide particles into groups regardless of position. For example, by using a threshold for their visualization. On the other hand, the main disadvantages of a Lagrangian approach are high computational costs, the convectiveness of the particles, leading to poor control over the investigated zones, due to particle motion and accumulation [**48**]. Furthermore, the influence of both particle distributions and particle seeding on these quantities of interest is poorly investigated. Therefore, adopting a Lagrangian approach would lead to some difficulties in getting a complete picture of the flow at specific time instants [**48**].

4.4.1 *WSS-based descriptors*

The fluid forces acting on the vessels' walls are thought to be able to stimulate the endothelium, thereby producing several cellular factors which may either inhibit or promote inflammatory events [**48**].

The wall shear-stress vector, WSS, is defined [**49**] as:

$$WSS = \tau_w = n \cdot \tau_{ij} \tag{4.5}$$

Where $\boldsymbol{n}$ is the normal vector to a surface and τ_{ij} is the fluid viscous tensor, thus the WSS is a vector whose magnitude is equal to the viscous stress on the surface and whose direction is the direction of the viscous stress, acting on the surface [**49**].

Evidence from in vitro and in vivo studies suggests that both low WSS and highly oscillatory patterns of WSS could cause intimal wall thickening, as observed at sites with specific features, such as curvatures, bifurcations, tortuosity and branching. In fact, these sites are characterized by a reduced flow velocity, by lower shear stress magnitude, as well as by non-unidirectional flow patterns [**48**].

WSS can influence endothelial cells layer morphology and orientation: under laminar flow conditions and high levels of WSS, endothelial cells elongate and align in flow direction, whereas under low and oscillatory WSS, these cells have a polygonal shape, without a clear orientation, due to the lack of organization of both

the cytoskeleton and the intercellular junctional proteins. Nevertheless, it has also been hypothesized that low WSS could induce stagnation of blood, thereby giving rise to prolonged contact between the vessel wall and blood components, such as platelets. The heamodynamic wall parameter contain information about spatial gradients of WSS and its temporal variation.

Below the main hemodynamic descriptors WSS-based are shown.

TAWSS

One of the most widespread WSS-based descriptors is the Time Averaged WSS, TAWSS [**50**], which is defined as follows:

$$TAWSS = \frac{1}{T}\int_0^T | \boldsymbol{WSS}(\boldsymbol{s}, t) | \cdot dt \quad \textbf{4.6}$$

where T is the overall interval of the cardiac cycle; $\boldsymbol{s}$ is the position on the vessel wall; and t is the time instant.

This index gives information about the average WSS magnitude, which endothelial cells experience during the observation time. It was reported that [**48**] low TAWSS values, particularly lower than 0.4 $^{N}/_{m^2}$ are thought to stimulate a pro-atherogenic endothelial phenotype, likely to be associated with a intima/media complex thickening. Moderate TAWSS values, nearly greater than 1.5 $^{N}/_{m^2}$, are supposed to induce quiescence and an atheroprotective gene expression profile, whereas higher TAWSS values, greater than 10-15 N/m2 and 25-45 $^{N}/_{m^2}$, are found to lead to endothelial trauma and haemolysis [**48**].

OSI

Oscillatory shear index (OSI) is used to identify regions on the vessel wall subjected to highly oscillating WSS directions during the cardiac cycle. These regions are usually associated with bifurcating flows and vortex formation that are strictly related to atherosclerotic plaque formation and fibrointimal hyperplasia. It is defined as [**49**]:

$$OSI = \frac{1}{2}\left(1 - \left(\frac{|\int_0^T WSSdt|}{\int_0^T |WSS|}\right)\right)$$

4.7

Low OSI values occur at sites where flow disruption is minimal, whereas high OSI values occur at sites where the instantaneous WSS deviates from the main flow direction in a large fraction of the cardiac cycle, thus inducing a perturbation in endothelial cells alignment [48]. In addition, the maximum OSI value is 0.5.

However, OSI descriptor is insensitive to shear stress magnitude. That is why sites with low TAWSS values may be characterized by significant OSI values, but not necessarily, because low shear stress might result from flow expansion, due to the pulsating behaviour, without any local reversal flow [**48**]. Likewise, strong oscillatory flows can exhibit the same OSI as very slow flows with the same waveform [**48**]. Moreover, it seems unlikely that endothelial cells sense OSI per se: in fact some investigations pointed out that only the presence of low and oscillating WSS promotes the atherosclerosis plaque formation, whereas if TAWSS is nearly in the physiological range (1-2 $^{N}/_{m^2}$) the intimal thickness is normal, whatever the OSI value is [**48**]. In conclusion, OSI index would give more appropriate data if it were combined with other shear stress measures, instead of being used as a stand-alone index.

RRT

The information, which were collected from the previous indexes, are combined in another index, the Relative Residence Time: RRT [**49**] :

$$RRT = \frac{1}{(1 - 2OSI)TAWSS} = \frac{T}{|\int_0^T |\boldsymbol{WSS}(\boldsymbol{s}, t)| \cdot dt|}$$

4.8

This index is inversely proportional to the magnitude of the TAWSS vector and RRT values for particles near the wall are proportional to a combination of OSI and TAWSS. In any case, the RRT index is simply another type of time-averaged WSS, but with a more tangible connection to biological mechanisms, underlying

atherosclerosis. Hence this hemodynamic descriptor may be considered as a more robust single metric of "low and oscillatory" shear stress [**48**].

4.4.2 *Bulk flow analysis*

Most mechanisms promoting degenerative phenomena and pathologies affecting vascular districts deal with three- and four-dimensional phenomena. In addition, the bulk flow plays a key role in determining WSS patterns. Notwithstanding the focus of majority of the studies, the literature available is material almost exclusively WSS-based metrics as quantitative indicators of disturbed flow. In the past, the potential role of bulk flow in the development of arterial disease was scarcely investigated. This fact is partially due to the lack of robust quantitative descriptors of bulk flow, combined with the ability of operating a reduction of the inherent complexity associated to four-dimensional flow fields in realistic geometries [**48**]. Some studies reported quantitative results demonstrating the presumption that arterial bulk flow could explain the fluid-wall interaction processes leading to the onset of vessel wall pathologies. Furthermore after the observation of unfavourable effects, like alterations in mass transfer and particle residence times, strictly related to bulk flow effects, especially when blood flow is complex, it was suggested that WSS-based analysis should be integrated with a quantitative description of the bulk flow, because such a description would represent a potential source of information [**48**].

With the aim to investigate the relationship between particular blood flow patterns and pathological events, *helicity* has recently gained recognition as capable of describing the arrangement of blood streams in complex patterns. The use of helicity to analyse bulk flow features has been very widespread during the last years because it measures the alignment of the velocity and the vorticity vectors and also represents the potential for helical flow to evolve [**48**]. In addition, helical flow is the product of the composition of translational and rotational motion and its role in vascular hemodynamics has long been debated.

From a phenomenological viewpoint, an arrangement of bulk flow in complex helical patterns might play a significant role in the tuning of the cells mechano-transduction pathways. It is likely that for highly helical flows, the conservation laws, within the Navier–Stokes equation, inhibit the transfer of helicity down the

length scales, and therefore the process through which energy is transferred [**48**]. As a result of this inhibition, helical energy may affect the focal contact between endothelial cell and the monocytes within the flow. In fact, due to the complex three-dimensional flow pattern, helical structures could elicit the convective dispersion of monocytes within the vessel at all scales. Furthermore, the stability induced by helical flow and the decrease in laterally directed forces may reduce turbulence [**48**]. Recently, the existence of a relationship between helical flow patterns and transport phenomena has been emphasized, which affect blood–vessel wall interaction. Indeed, these processes are fundamental in order to trigger inflammatory responses, provoked by alterations in the residence time of atherogenic particles [**48**]. Moreover, bulk flow structures are primarily responsible for mass transfer, especially for those species within blood, whose processes are promoted by mixing induced by convection. For example, several studies identify the oxygen flux to the arterial wall to be another factor involved in the localization of atherogenesis, whereas recent studies have provided evidence for the existence of a relationship between shear-induced activation of platelets and metrics that give measurements regarding the alignment of the local velocity and vorticity vectors [**48**]. According to these observations, it is clear that helical flow represents a natural feature of arterial hemodynamics , hence thorough understanding of the generation and disappearance of helical structures in the streaming blood is of great interest. In addition, helical flow could be used as a fluid dynamic signature for the identification of sites prone to fibrointimal thickening and atherosclerotic plaque formation [**48**].

LNH

A useful indicator of how velocity field is oriented with respect to vorticity field is given by the local value of the cosine of the angle between the velocity and vorticity vectors. [**48**]:

$$LNH(\boldsymbol{x},t) = \frac{\boldsymbol{v}(\boldsymbol{x},t)\cdot\boldsymbol{w}(\boldsymbol{x},t)}{|\boldsymbol{v}(\boldsymbol{x},t)||\boldsymbol{w}(\boldsymbol{x},t)|} = \cos\varphi(\boldsymbol{x},t)$$

$$-1 \le LNH \le 1 \qquad \textbf{4.9}$$

Where v is the velocity vector, ω is the vorticity vector, x is the position and t the time instant. LNH is the local value of the cosine of the angle $\varphi(\boldsymbol{x}, t)$ between the velocity and the vorticity vectors: the absolute value of LNH can range between one, when the flow is purely helical, and zero, in presence of reflectional symmetry in the flow. The sign of LNH is a useful indicator of the direction of the rotation. Hence, LNH is a useful descriptor of changes in the direction of the rotation of flow into vessels during the cardiac cycle.

CHAPTER 5
RESULTS AND DISCUSSION

This chapter presents the post-processing results of the geometrical model. The chapter is divided into four sections. The first paragraph is about the new steady simulation of the mesh F that are launched with the average flow rate of unsteady simulation like boundary conditions to make the comparison. The second section compares the post-processing results of hydraulic losses in steady and unsteady simulation to evaluate the percentage of error that is made when a simplified steady model is used instead of the real unsteady model. The third paragraph show the results of the Eulerian analysis: *TAWSS*, *OSI* and *RRT*. The last section compares the results of the Lagrangian analysis: *LNH*.

5.1 **Introduction**

The blood flow in these anatomies is *unsteady*, but the pulsatility is often neglected when modelling TCPC hemodynamics. In fact, time-averaged flow boundary conditions have traditionally been used. But, recent studies have shown that pulsatility could have an effect on the hemodynamic predictions of TCPC when the pulsatility level is high [**51**]. DeGroff et al. and Dur et al. (2002) [**52, 53**] showed that pulsatility led to significant increase in power loss in idealized models.

Furthermore, De Zelicourt (2010) [**54**] showed that in a patient with high flow pulsatility, the non-pulsatile assumption failed to capture the global flow characteristics.

But no study to date has adequately considered the effects of pulsatile flow when determining the optimal total cavopulmonary connection offset.

In our work, we want to observe the differences in the bloodstream, comparing different parameters in steady simulation and in unsteady simulation of the same model. In order to make this comparison, a new steady simulation of the mesh F was launched, with the *average flow rate* of unsteady simulation.
This type of research is very important, because it allows us to evaluate the percentage of error that is made when a simplified steady model is used instead of the real unsteady model.

The parameters taken into account are:

- Hydraulic losses,
- WSS-based index (*TAWSS, OSI, RRT*),
- Bulk flow index (*LNH*).

5.2 **Hydraulic losses**

5.2.1 *Unsteady simulation*

To calculate the hydraulic losses in this unsteady simulation, the same equation used to steady simulation is applied (equation 3.3).

Therefore, the values of velocity magnitude and static pressure are exported during the simulation for each iso-surface (SVC, IVC, RPA, LPA). The values considered, in this calculation, are those which relate to a single cardiac cycle, that is, the fifth cycle in which the transition has been extinguished, that has a duration of 1500 *ms*. After having obtained all the necessary parameters, the E_{loss} is calculated for each time step in which the cardiac cycle is divided (that is 750 time step). At the end, the result can be seen in the graph below:

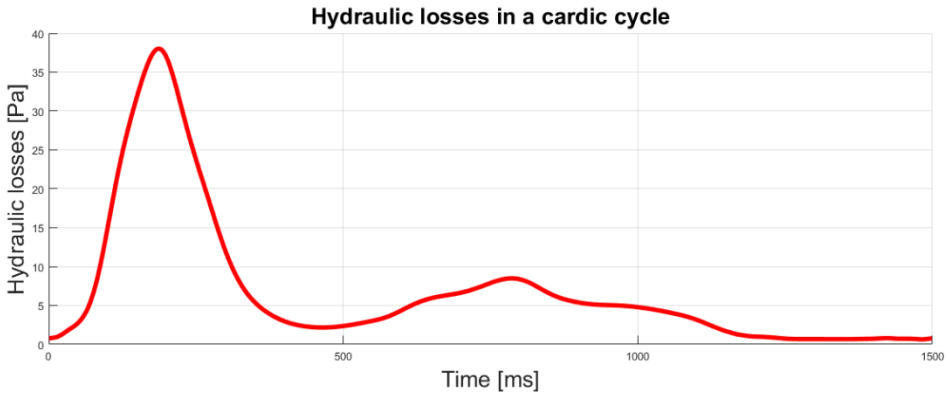

Chart 5.1 Hydraulic losses in cardiac cycle

On the graph one can observe a peak right at the beginning of the cardiac cycle. This is an indication that there is greater dissipation of energy during atrial

diastole, that is, when the left atrial is filling.

5.2.2 *Steady simulation*

To evaluate the difference in hydraulic losses in steady and unsteady simulation, the results have been put together in the chart below.

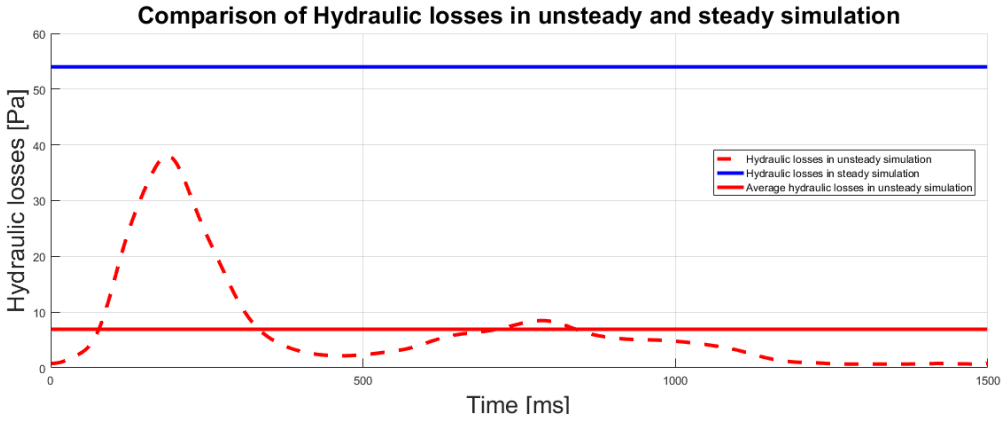

Chart 5.2 Comparison of hydraulic losses in steady and unsteady simulation

In the chart 5.2 one can observe that the difference of hydraulic losses between steady and unsteady model is significant. In fact, the value of hydraulic losses is 54.2679 Pa and 6.9173 Pa, respectively, with a percentage difference of 87.25%. of the steady compared to the unsteady simulation.

5.3 **WSS-based index**

The hemodynamic wall descriptors that were analysed are the Time-Average Wall Shear Stress (TAWSS), the Oscillatory Shear Index (OSI) and the Residence Relative Time (RRT). In this way it is possible to evaluate the average values for the WSS during the period of time of the simulation (a cardiac cycle), its oscillating pattern, as well as to estimate the residence time of blood components. As reported in chapter 4, these three quantities try to estimate and quantify important hemodynamic aspects of influence on blood flow.

The hemodynamic parameters were evaluated using the software Matlab and were presented with the aid of the software TecPlot.

5.3.1 *TAWSS*

TAWSS results are shown in the figure 5.1.

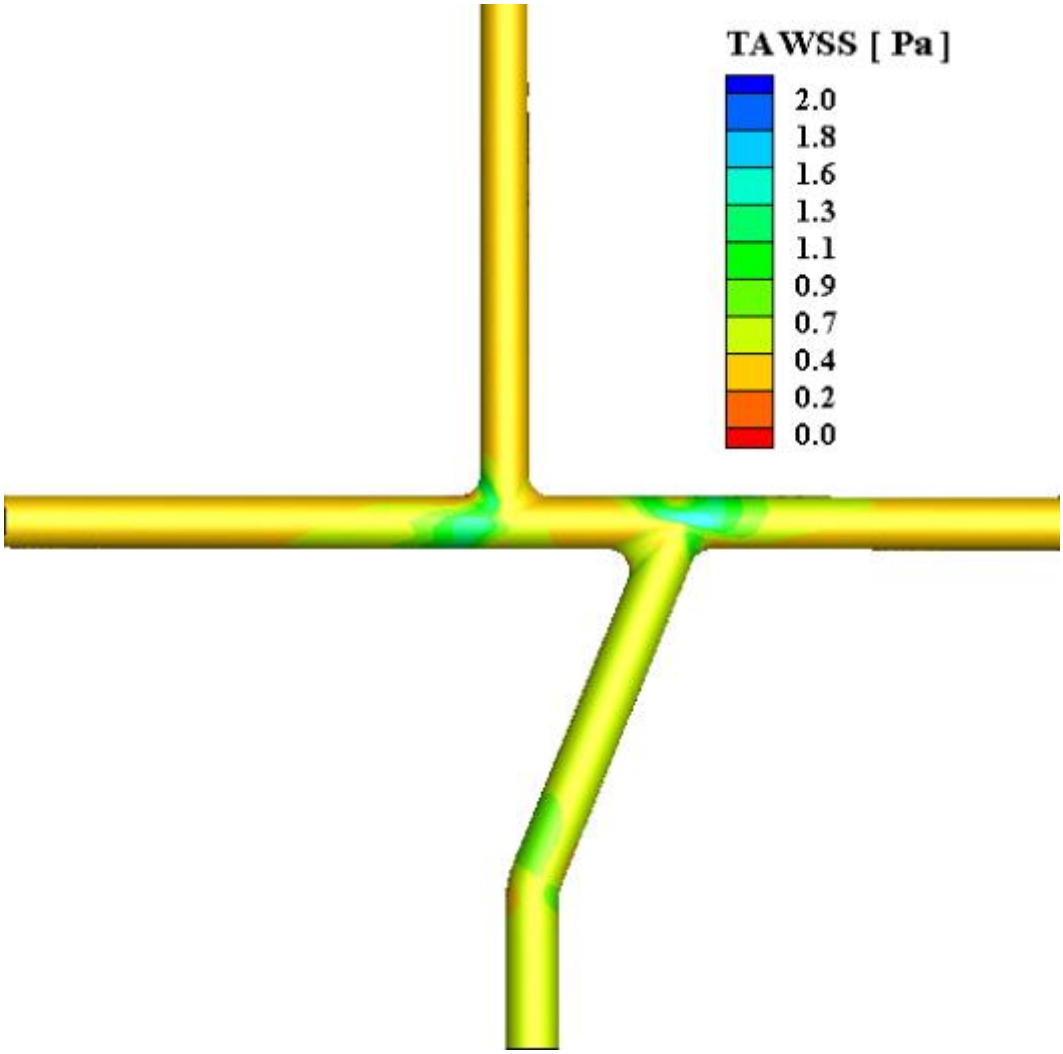

Figure 5.1 TAWSS distribution

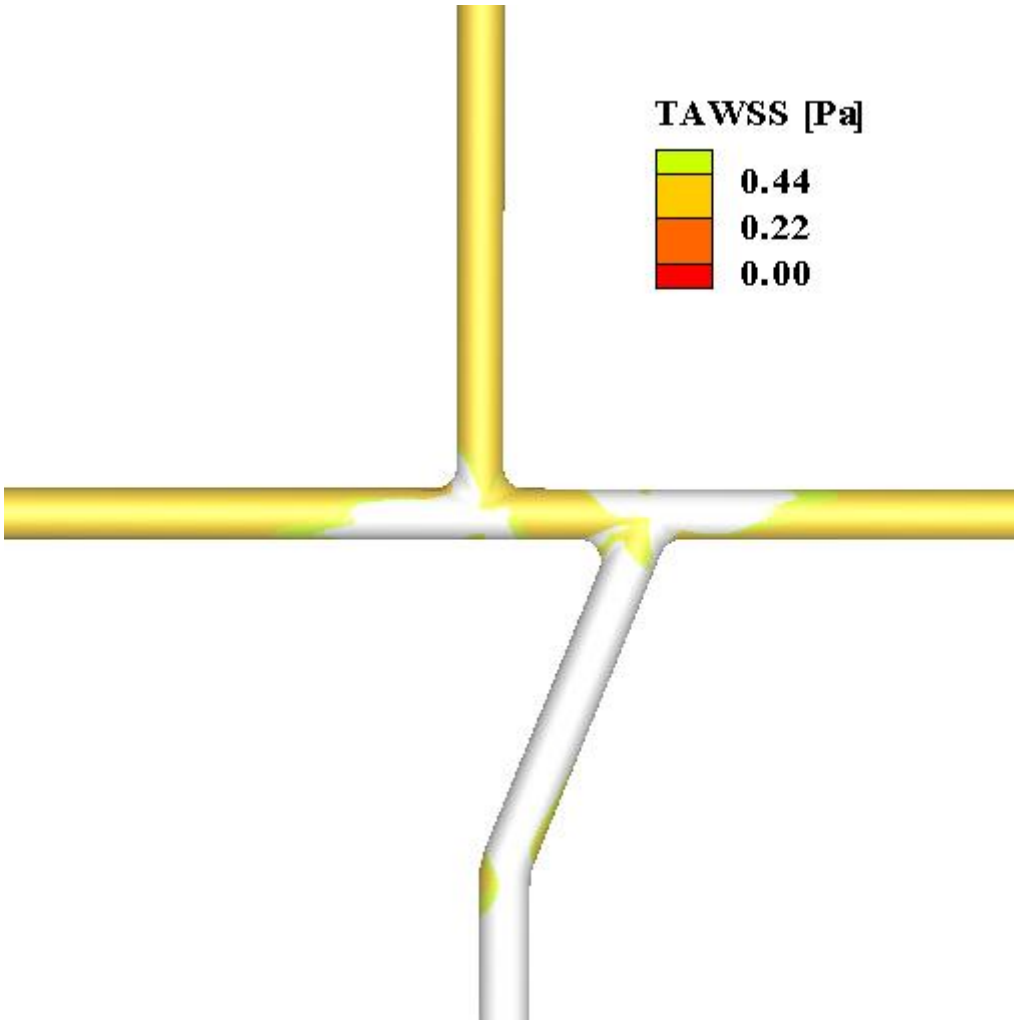

Figure 5.2 TAWSS of dangerous values

The colormap in the figure present the high values of TAWSS indicated with blue and low values shown with red. The TAWSS distribution has its higher values at the bifurcation site because the blood flows against the vessel wall (sky blue colour), thereby exerting a greater force, and also where there is the curvature of the inferior vena cava. In the rest of the model, the values of TAWSS are very low. Especially in the pulmonary arteries and in the superior vena cava, where the values are included in the range from 0.2 to 0.4 (orange colour). Previous studies have shown that this range of values is known to stimulate a proatherogenic endothelial phenotype and could lead to intimal thickening, making it dangerous.

In the figure 5.2 , the dangerous areas are putin relief.

5.3.2 *WSS in steady simulation*

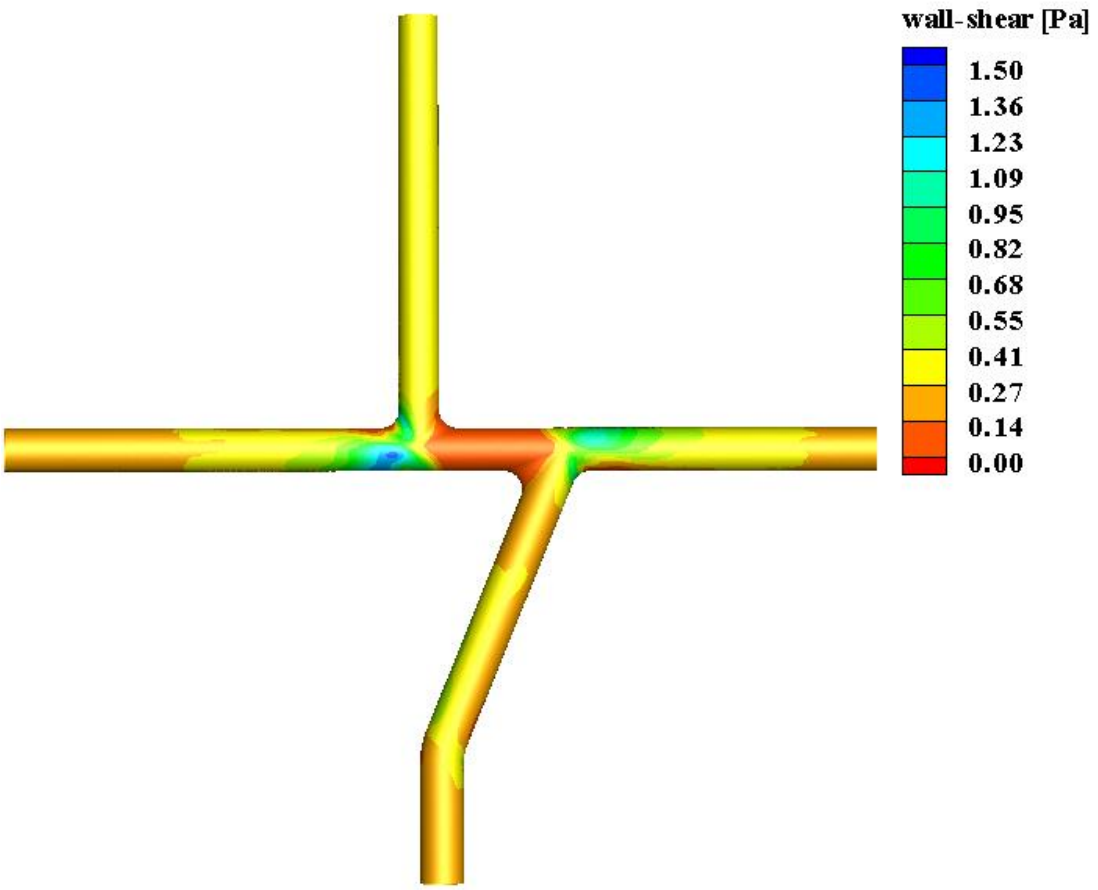

Figure 5.3 WSS in steady simulation

In the steady model, one can observe that, like in the unsteady case, the highest values of WSS are located in correspondence of the bifurcation, where the blood flow that arrives from the superior and inferior venas goes to slam on the arteries exerting a greater force. Whereas, when the blood flow move away from this central zone, that is when it develops its motion in the arteries and the WSS values become low.

5.3.3 *OSI*

The oscillating pattern of the WSS was observed after the simulations. Figure 5.3 shows its distribution.

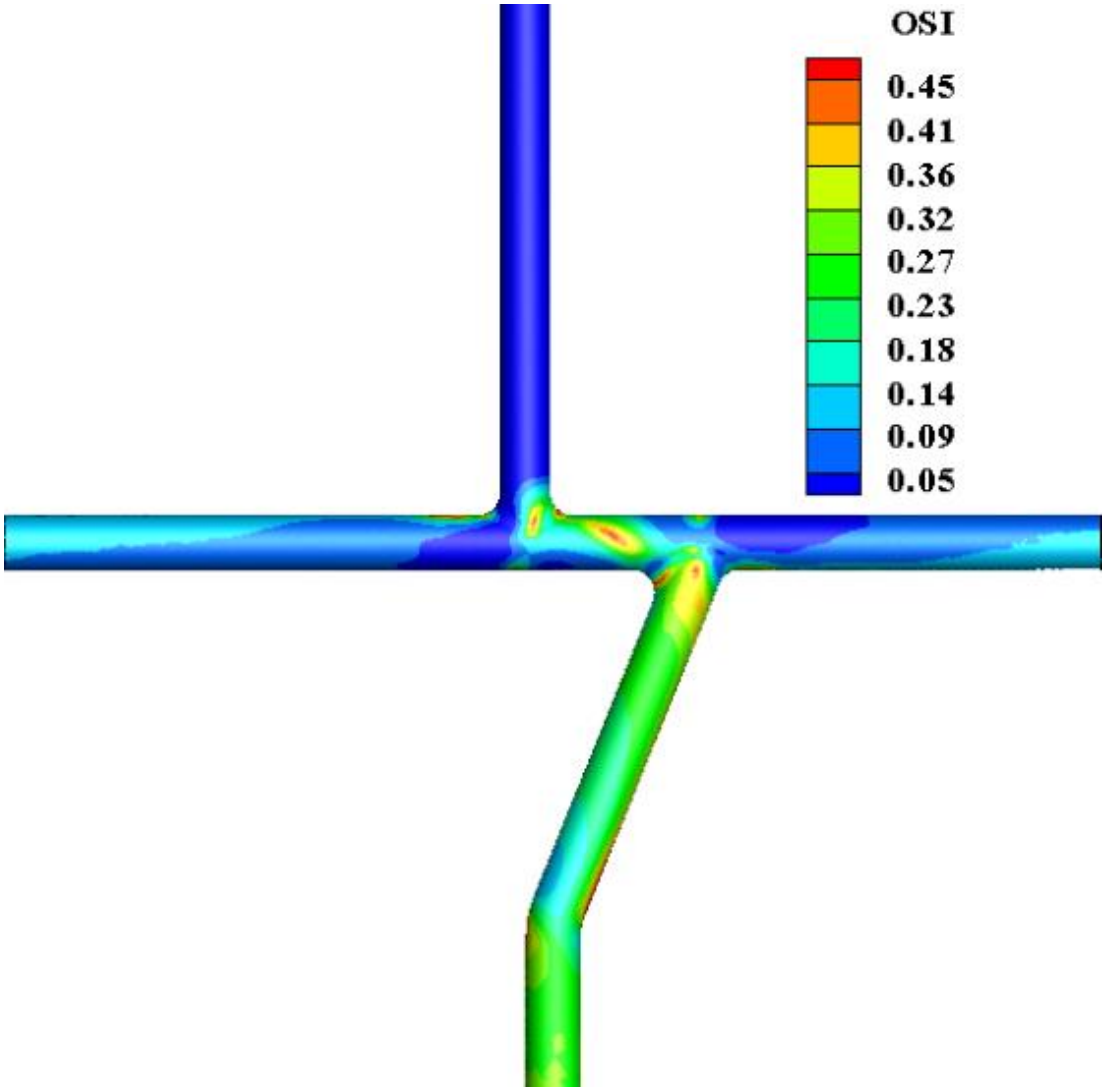

Figure 5.4 OSI distribution

Areas, with the highest oscillations, are found in correspondence with the bifurcation, indicated in red and yellow. The inferior vena cava presents high values of oscillations compared to the values in pulmonary arteries and the superior vena cava. In fact, the latter has low values, that is, values under the critical value of 0.1, indicated with blue colour.

5.3.4 *RRT*

The residence relative time distribution was estimated in the model. Figure 5.5 show the distribution.

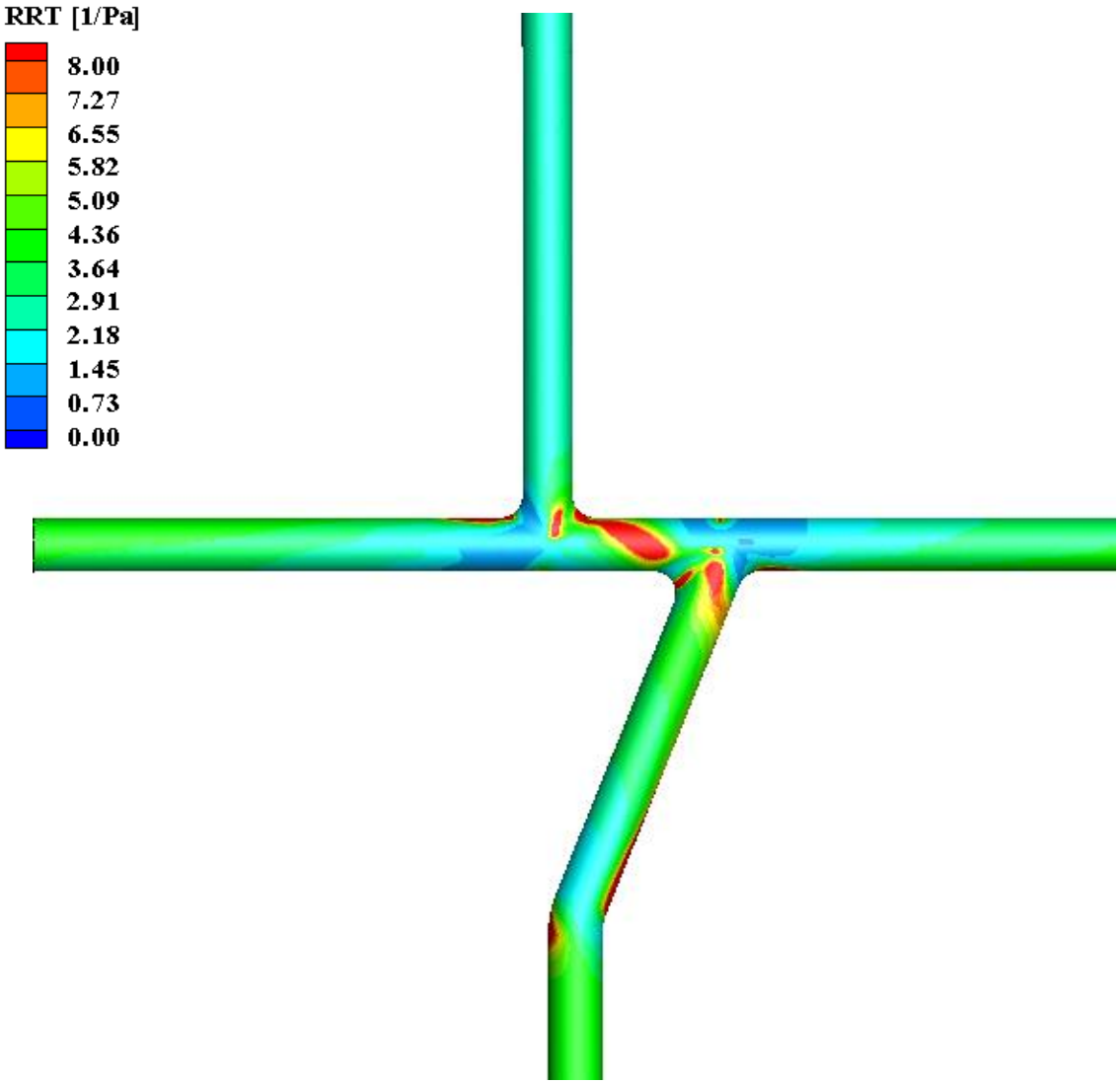

Figure 5.5 RRT distribution

The greatest values of RRT (indicated in red) are located in correspondence with the bifurcation, precisely in the arterial area found between the two veins. In this area, the blood flow that comes from the inferior vena collides with the flow that comes from the superior vena cava, creating a recirculation zone. But, in the bifurcation area, where the blood flow is oriented from the veins directly onto the wall of the arteries, the values of RRT are lowest (indicated in blue). Because the particles are not stationary for a long time in the vicinity of the wall, there is no platelet activation. When the flow moves away from the bifurcation (indicated with the green) the RRT values are raised.

5.4 **Bulk flow index**

For the bulk flow analysis one hemodynamic quantitative was chosen: the *helicity* (LNH).

5.4.1 *LNH*

The helicity pattern is reported in the pictures below for the model.

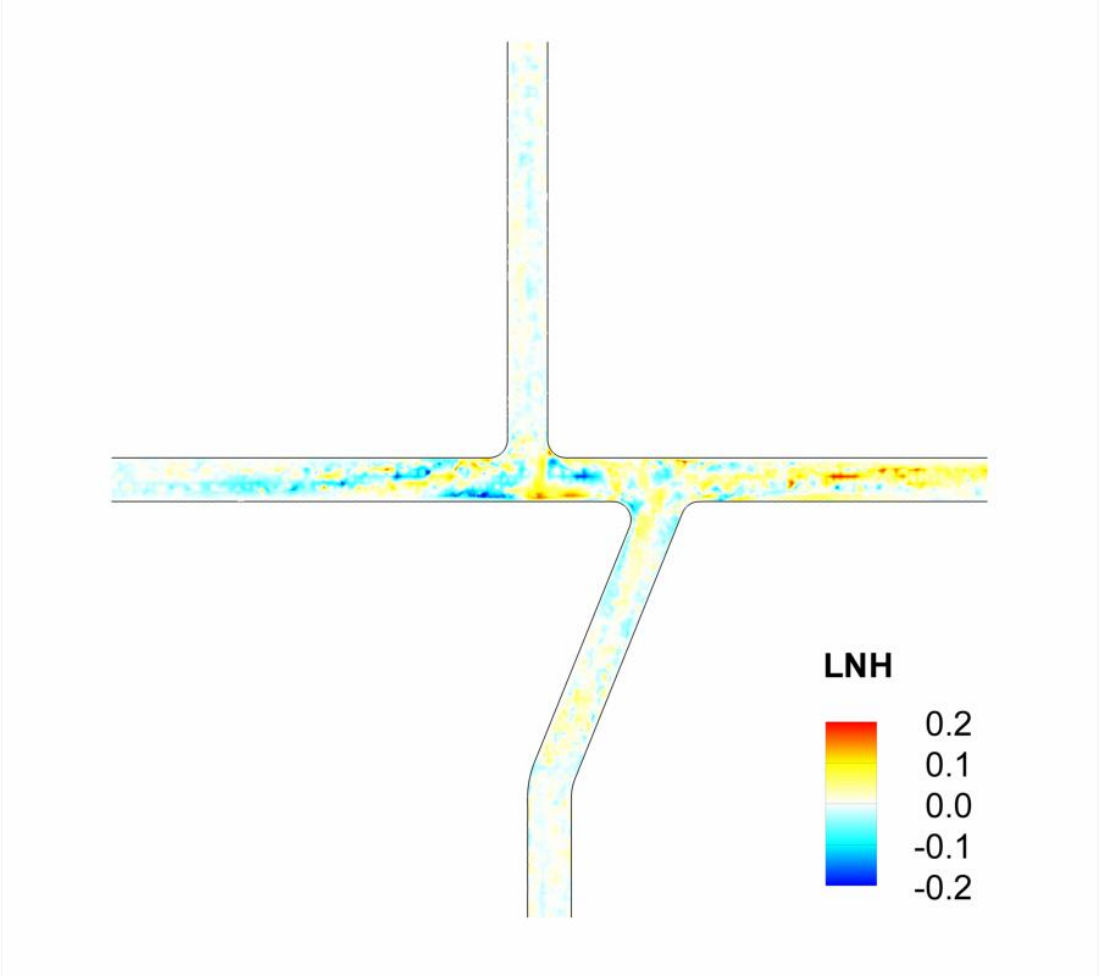

Figure 5.6 LNH distribution

The sign of LNH is a useful descriptor which indicates the formation of helical structures within the vascular district in exam. In fact, the value 0 in the inferior and superior venas cava suggests the presence of reflective symmetry in the flow, that is, a type of symmetry where one half is the reflection of the other half.

Diversely, in the pulmonary artery the particles in the flow experience complete rotations in both the clock-wise, indicated in red and the counter clock-wise, indicated in blue

The left artery sees the presence of particles which rotate in a clock-wise direction, whereas the most particles in the right artery rotate in counter clock-wise direction.

CHAPTER 6
CONCLUSION

The final aim of this master thesis work is to compare the hydraulic losses in the steady and unsteady model and to evaluate the hemodynamics in the TECPC model.

From the calculation of hydraulic losses, it can be observed that when a simplified model of reality is considered (as is the case of the steady model), one must take into account that the computed hydraulic losses, will be overestimated. Hence, this fact puts us in a safe condition. But, on the other hand, the approximation given by the steady model differs substantially from the physiological case, which is much more similar to the case given by the unsteady model. In fact, the waveforms used as inlet, are real data of the patients present in the article of Ajit P. Yoganathan e al (2012) [**46**]. It can thus be deduced that given the huge percentage difference between the two cases, it is much more convenient to use the unsteady model that is closer to physiological values, rather than using the steady model which entails saving on costs and computational times, but that will produce values that move away from reality.

Afterwards, in assessing the role of hemodynamic forces on the vessel wall, it is seen that the behaviour of WSS in the case of the steady model and the behaviour of TAWSS in the case of the unsteady model are very similar. They both have higher values in correspondence with the bifurcation and low values in the rest of the wall considered in the model. Therefore, the simplified steady model can be used to calculate the WSS, saving on costs and on computational time.

Evaluating the OSI descriptor, it can be observed that in general the model has low oscillation values of WSS. This is a positive factor, because the marked oscillations in the direction of WSS are associated with low mean shear stress (see in TAWSS) and may be critical factors in the localization and development of atherosclerotic plaques.

The RRT descriptor has demonstrated that the area in which is more probable the development of pathologies like atherosclerosis, because there are low values of WSS and marked oscillation of WSS, is the area of the artery found between the venas cava, because the blood flow collides, thereby creating a recirculation zone. Another region where pathologies could develop is the area distant from the bifurcation, where the blood flow has a low force because it is pushed only by the veins. In this area of disturbed flow, endothelial cells experience low or oscillatory WSS and appear more polygonal without a clear orientation, with a lack of organization of the cytoskeleton and intercellular junctional proteins.

WSS-based analysis is integrated with a quantitative description of the bulk flow. The LNH descriptor shows that in the pulmonary artery the particles in the flow experience complete rotations in both the clock-wise and the counter clock-wise. This helical flow could identify the presence of sites in which there is a ‘disturbed flow’, that is, the sites prone to fibrointimal thickening and atherosclerotic plaque formation.

It is clear from these studies that improvements to the geometrical model are necessary, moreso if the wide variety of patient anatomies makes it difficult to design a general “one-size-fits-all” procedure for Fontan patients.

Among the future developments could be considered a model in which a *fenestration* is applied, that is a connection between atrium and inferior vena cava, could be considered.

Another work could be the realization of a model obtained directly from the patient's clinical images in order to analyze a geometrical model that gives us the more physiological results.

APPENDIX

IVC.c

```
#include "udf.h"

DEFINE_PROFILE(vin_IVC, thread, nv)
{
face_t f;
real flow_time = RP_Get_Real("flow-time");
real tt=flow_time;
real area=0, A[ND_ND];
real vfr=0;
real T=1.500;
int i;
real pi=3.141592;
real a[21] = {9.5696574e-06,-1.5068789e-05,7.6380098e-07,-
2.5676927e-07,3.8744144e-06,1.1446709e-06,4.5543456e-
07,3.7478588e-07,1.2685626e-07,-7.9493674e-08,4.3715992e-09,-
1.9036613e-07,5.8339068e-08, 2.8343344e-08,-4.4472681e-
08,2.7264450e-09,-8.7590144e-08,2.2101809e-08,4.8826090e-
08,4.3088000e-08,6.1438637e-08};
real b[21] = {0,-7.5468748e-06,-2.5082914e-06,-4.2734714e-06,-
2.9406337e-06,2.3679627e-07,8.8239471e-07,-3.4442338e-
08,2.6932618e-07,-5.0293550e-07,-6.1302966e-08,-2.3856436e-
07,-1.8037997e-07,-1.5090809e-07, -2.7689735e-07,-2.4142096e-
07,-2.5395575e-07,-2.8230959e-07,-1.8626342e-07,-1.4970001e-
07,-8.6961443e-08};

/*La serie di Fourier approssima la portata in ingresso
(m^3/s)*/
for (i=0;i<21;i++)
     {
     vfr+=a[i]*cos(i*2*pi*tt/T)+b[i]*sin(i*2*pi*tt/T);
     }

begin_f_loop(f,thread)
                {
            F_AREA(A,f,thread);
            area+=NV_MAG(A);
           }
end_f_loop(f,thread);

begin_f_loop(f,thread)
           {
            F_PROFILE(f,thread,nv)=(vfr/area);
            /* /area: passo alla velocità*/
```

```
          }
end_f_loop(f,thread);

}
```

SVC.c

```
#include "udf.h"

DEFINE_PROFILE(vin_SVC, thread, nv)
{
face_t f;
real flow_time = RP_Get_Real("flow-time");
real tt=flow_time;
real area=0, A[ND_ND];
real vfr=0;
real T=1.500;
int i;
real pi=3.141592;
real a[21] = {1.1354094e-05,-2.5311291e-06,-9.1912357e-08,-
3.6814414e-06,-8.8580771e-07,-9.0210673e-08,1.2747088e-
07,2.5307880e-07,2.0395425e-08,1.2886431e-07,1.3034318e-07,-
3.3548176e-08,2.7272902e-08, 2.5481756e-08,3.1292148e-
08,2.1138064e-08,4.6368161e-08,3.0068160e-08,-4.5421730e-
09,1.3832088e-08,1.5213227e-08};
real b[21] = {0,4.9163541e-06,1.8445504e-06,7.7113506e-07,-
2.1193730e-06,-7.6258835e-07,-6.2874850e-07,-3.6275942e-07,-
1.7736000e-07,-8.3339982e-08,-9.4961776e-08,-1.1581760e-07,-
1.7012863e-08, -7.9943636e-08,-1.1090901e-07,-4.5839805e-08,-
2.7595338e-08,-4.2573702e-08,-3.4827547e-08,-2.6512556e-08,-
3.9021825e-08};

/*La serie di Fourier approssima la portata in ingresso
(m^3/s)*/
for (i=0;i<21;i++)
     {
     vfr+=a[i]*cos(i*2*pi*tt/T)+b[i]*sin(i*2*pi*tt/T);
     }

begin_f_loop(f,thread)
               {
            F_AREA(A,f,thread);
            area+=NV_MAG(A);
           }
end_f_loop(f,thread);

begin_f_loop(f,thread)
          {
           F_PROFILE(f,thread,nv)=(vfr/area);
           /* /area: passo alla velocità*/
          }
end_f_loop(f,thread);

}
```

BIBLIOGRAPHY

[1]. http://www.innerbody.com/image/card01.html#full-description

[2]. http://lsa.colorado.edu/essence/texts/heart.html

[3]. https://www.boundless.com/biology/textbooks/boundless-biology-textbook/the-circulatory-system-40/mammalian-heart-and-blood-vessels-226/arteries-veins-and-capillaries-853-12098/

[4]. https://en.wikipedia.org/wiki/Blood

[5]. Master thesis in Biomedical engineering: Computational hemodynamic models of abdominal aortic endovascular grafts of Veronica Gonella.

[6]. http://www.cvphysiology.com/Hemodynamics/H011.htm

[7]. https://en.wikipedia.org/wiki/Viscosity

[8]. https://www.ncbi.nlm.nih.gov/pubmed/2658951

[9]. http://hypertextbook.com/facts/2004/MichaelShmukler.shtml

[10]. Master thesis in Biomedical engineering: Computational hemodynamic models of abdominal aortic endovascular grafts of Veronica Gonella.

[11]. F.Fontan E.Baudet. Surgical repair of tricuspid atresia. Thorax 1971.

[12]. Ara K. Pridjian, Alan M. Mendelsohn, Flavian M. Lupinetti, Robert H. Beekman III, Macdonald Dick II, Gerald Serwer, Edward L. Bove. Usefulness of the bidirectional Glenn procedure as staged reconstruction for the functional single ventricle. The American Journal of Cardiology.

[13]. Jacqueline Kreutzer, John F. Keane, James E. Lock, Edward P. Walsh, Richard A. Jonas, Aldo R. Castafieda, John E. Mayer, Jr. Conversion Of Modified Fontan Procedure To Lateral Atrial Tunnel.

[14]. David Senft, Amelie Elsaesser, and Christoph Kampmann. Intra- or extracardiac Fontan operation? A simple strategy when to do what Wlodzimierz Kuroczynski.

[15]. Albert C. Lardo, Steven A. Webber, Ingeborg Friehs, Pedro J. del Nido, Edward G. Cape. Fluid Dynamic Comparison Of Intra-Atrial And Extracardiac Total Cavopulmonary Connections.

[16]. Jayakumar KA, Addonizio LJ, et al. Cardiac transplantation after the Fontan or Glenn procedure. J Am Coll Cardiol. 2004.

[17]. Marino BS. Outcomes after the Fontan procedure. Current Opinion in Pediatrics. 2002.

[18]. Rychik J, Cohen MI. Long-term outcome and complications of patients with single ventricle. Progress in Pediatric Cardiology, 2002.

[19]. Kiesewetter CH, Sheron N, et al. Hepatic changes in the failing Fontan circulation. Heart, 2007.

[20]. Guyton AC, Abernathy B, et al. Relative importance of venous and arterial resistances in controlling venous return and cardiac output. Am J Physiol, 1959.

[21]. Uemura H, Yagihara T, et al. Redirection of hepatic venous drainage after total cavopulmonary shunt in left isomerism. Ann Thorac Surg, 1999.

[22]. Orlando W, Hertzberg J, et al. Reverse flow in compliant vessels and its implications for the Fontan procedure: numerical studies. Biomed Sci Instrum, 2002.

[23]. Bazilevs Y, Hsu MC, et al. Computational fluid-structure interaction: methods and application to a total cavopulmonary connection. Computational Mechanics, 2009.

[24]. Marsden A, Reddy V, et al. A new multiparameter approach to computational simulation for Fontan assessment and redesign. Congenit Heart Dis, 2010.

[25]. Sankaran S, Marsden AL. A stochastic collocation method for uncertainty quantification in cardiovascular simulations. 2010 to appear in J. Biomechanical Eng.

[26]. Sundareswaran KS, Pekkan K, et al. The total cavopulmonary connection resistance: a significant impact on single ventricle hemodynamics at rest and exercise. Am J Physiol Heart Circ Physiol, 2008.

[27]. Lakshmi P. Dasi, Kerem Pekkan, Diane de Zelicourt, Kartik S. Sundareswaran, Resmi Krishnankutty, Pedro J. Delnido, and Ajit P. Yoganathan. Hemodynamic Energy Dissipation in the Cardiovascular System: Generalized Theoretical Analysis on Disease States.

[28]. https://it.wikipedia.org/wiki/Joule

[29]. https://www.dawsoncollege.qc.ca/public/72b18975-8251-444e-8af8-224b7df11fb7/programs/smse/biomed/10_gases.pdf

[30]. https://en.wikipedia.org/wiki/Bernoulli%27s_principle

[31]. Cary W. Akins and Ajit P. Yoganathan. Energy loss for evaluating heart valve performance.

[32]. Colan SD. Ventricular function in volume overload lesions. In: Fogel MA, ed. Ventricular function and blood flow in congenital heart disease. Philadelphia: Blackwell; 2005: 205-22.

[33]. Colan SD. Ventricular function in pressure overload lesions. In: Fogel MA, ed. Ventricular function and blood flow in congenital heart disease. Philadelphia: Blackwell; 2005:187-204.

[34]. Marsden AL, Bernstein AJ, et al. Evaluation of a novel Y-shaped extracardiac Fontan baffle using computational fluid dynamics. Journal of Thoracic and Cardiovascular Surgery; 2009.

[35]. Amodeo A, Grigioni M, Oppido G, Daniele C, D'Avenio G, Pedrizzetti G, Ginnico S, Filippelli S, Di Donato RM. The beneficial vortex and best spatial arrangement in total extracardiac cavopulmonary connection. J Thorac Cardiovasc Surg; 2002.

[36]. Sharma S, Goudy S, Walker P, Panchal S, Enseley A, Kanter K, Tam V, Fyfe D, Yoganathan A. *In vitro* flow experiments for determination of optimal geometry of total cavopulmonary connection for surgical repair of children with functional single ventricle. J Am Coll Cardiol; 1996.

[37]. Grigioni M , Daniele C , Del Gaudio C , Morbiducci U , Balducci A , D'Avenio G , Amodeo A , Barbaro V , Di Donato R. Numerical simulation of a realistic total cavo-pulmonary connection: effect of unbalanced pulmonary resistances on hydrodynamic performance. The International Journal of Artificial Organs; 2003.

[38]. http://www-mdp.eng.cam.ac.uk/web/library/enginfo/aerothermal_dvd_only/aero/fprops/pipeflow/node9.htmlhttp://www-mdp.eng.cam.ac.uk/web/library/enginfo/aerothermal_dvd_only/aero/fprops/pipeflow/node9.html

[39]. https://en.wikipedia.org/wiki/Entrance_length#Entry_Length

[40]. Falkovich, G. *Fluid Mechanics.* Cambridge : Cambridge University Press, 2011.

[41]. file:///D:/tesi%20Fontan/Pipeflow_intro.pdf

[42]. Andrea Saltelli, Marco Ratto, Terry Andres, Francesca Campolongo, Jessica Cariboni, Debora Gatelli, Michaela Saisana, Dr. Stefano Tarantola. Global Sensitivity Analysis: The Primer.

[43]. http://www.micheleramazza.com/documenti/M.%20Ramazza%20(2009)-%20Undular%20jump,%20numerical%20model%20and%20sensitivity%20analysis.pdf

[44]. Ryu, K., Healy, T. M., Ensley, A. E., Sharma, S., Lucas, C., and Yoganathan, A. P., 2001. Importance of Accurate Geometry in the Study of the Total Cavopulmonary Connection: Computational Simulations and In Vitro Experiments.

[45]. BMF 2013/2014

[46]. Reza H.Khiabani, Maria Restrepo, Elaine Tang, Diane De Zelicourt, Fotis Sotiropoulos, Mark Fogel, AjitP. Yoganathan. Effect of flow pulsatility on modelling the hemodynamics in the total cavopulmonary connection.

[47]. Gasbarro et al.; European Journal of Computational Mechanics (2007). Explicit finite element method for in-vivo mechanics of abdominal aortic aneurysm.

[48]. Gallo D. et al. A survey of quantitative descriptors of arterial flows.Springer 2014.

[49]. Chiastra et al. "Computational fluid dynamic simulations of image-based stented coronary bifurcation models", Journal of The Royal Society, 2013.

[50]. Massai D. et al. "Shear-induced platelet activation and its relationship with blood flow topology in a numerical model of stenosed carotid bifurcation", European Journal of Mechanics B/Fluids, 2012.

[51]. Marsden, Vignon-Clementel, Chan, Feinstein, Taylor. Effects of exercise and respiration on hemodynamic efficiency in CFD simulations of the total cavopulmonary connection, 2007.

[52]. DeGroff, Shandas. Designing the optimal total cavopulmonary connection: pulsatile versus steady flow experiments. Medical Science Monitor: International Medical Journal Of Experimental And Clinical Research, 2002.

[53]. Dur, DeGroff, Keller, Pekkan. Optimization of inflow waveform phase-difference for minimized total cavopulmonary power loss. Journal of Biomechanical Engineering, 2010.

[54]. De Ze´ licourt. Pulsatile Fontan Hemodynamics and Patient-Specific Surgical Planning: A Numerical Investigation. Ph.D.Thesis.GeorgiaInstitute of Technology,Atlanta,2010.

FIGURES

1.8 https://www.google.it/search?q=struttura+vene+arterie&biw=1366&bih=638&source=lnms&tbm=isch&sa=X&ved=0ahUKEwilyvi42vXPAhWH0xoKHapFAicQ_AUIBigB#tbm=isch&q=atresia+tricuspide&imgrc=ikd1wgmy4g8VOM%3A.

1.9 https://www.google.it/search?q=norwood+procedure&biw=1517&bih=708&source=lnms&tbm=isch&sa=X&sqi=2&ved=0ahUKEwjFrJTPocPPAhUpCcAKHQ5bDEUQ_AUIBigB&dpr=0.9#imgrc=F0yK9Z6h9W73dM%3A.

1.10 https://www.google.it/search?q=tcpc+heart+surgery&bih=654&biw=1517&source=lnms&tbm=isch&sa=X&ved=0ahUKEwipw_aGwMHPAhUMIcAKHb7qCqMQ_AUICCgB&dpr=0.9#tbm=isch&q=glenn+procedure&imgrc=wFEKU-eX-bbVIM%3A.

1.11 https://pedclerk.bsd.uchicago.edu/page/hypoplastic-left-heart-syndrome.

1.12 https://www.ncbi.nlm.nih.gov/pmc/articles/PMC3866802/figure/F3/.

1.13 https://www.google.it/search?q=struttura+vene+arterie&biw=1366&bih=638&source=lnms&tbm=isch&sa=X&ved=0ahUKEwilyvi42vXPAhWH0xoKHapFAicQ_AUIBigB#tbm=isch&q=fontan+completion&imgrc=8jMwfGlEt8gdwM%3A.

1.14 http://heartdefectsforeveryone.blogspot.it/2010/04/univentricular-heart-single-ventricle.html

1.15 Cary W. Akins and Ajit P. Yoganathan. Energy loss for evaluating heart valve performance.

1.16 Cary W. Akins and Ajit P. Yoganathan. Energy loss for evaluating heart valve performance.

2.1 http://www.cardiopatiascongenitas.net/tipos_cc_n_vutxt.htm

2.2 MANCANTE

2.3 http://www.slideshare.net/SandeshRajput/m-tech-project-26-june-2013-presentation

2.4 Keesuk Ryu, Timothy M. Healy, Ann E. Ensley, Shiva Sharma, Carol Lucas, and Ajit P. Yoganathan. Importance of Accurate Geometry in the

Study of the Total Cavopulmonary Connection: Computational Simulationsand *In Vitro* Experiments; 2001.

2.5 Grigioni M , Daniele C , Del Gaudio C , Morbiducci U , Balducci A , D'Avenio G , Amodeo A , Barbaro V , Di Donato R. Numerical simulation of a realistic total cavo-pulmonary connection: effect of unbalanced pulmonary resistances on hydrodynamic performance. The International Journal of Artificial Organs; 2003.

2.6 http://www.learneasy.info/MDME/MEMmods/MEM23006A/fluid_mech/lab-windtunnel.html

2.7 http://www.efm.leeds.ac.uk/CIVE/CIVE1400/Section4/boundary_layer.htm

RINGRAZIAMENTI

Voglio ringraziare prima di tutti il Professore Luca Ridolfi, il Professore Umberto Morbiducci, la professoressa Stefania Scarsoglio e il professore Gallo che mi hanno dato la possibilità di lavorare ad un tema che da sempre ha catturato la mia attenzione. Voglio inoltre ringraziare i dottorandi Paola e Giuseppe che mi hanno seguita costantemente in questi mesi e da cui ho imparato molto.

Ringrazio la mia mamma e il mio papà per la loro essenziale presenza, per avermi dato il sostegno, il coraggio e la forza; per avermi fatto sentire sempre amata, per essere il mio modello in ogni campo della vita, ed è a loro che dedico questa mia piccola, grande vittoria. Ringrazio i miei fratelli: Joy e Giuseppe per aver reso sempre colorita e vivace la mia infanzia e la mia adolescenza, per essere cresciuti insieme e per essere il tassello fondamentale della mia vita.

Voglio inoltre ringraziare la mia collega e coinquilina Cristina per aver condiviso insieme praticamente tutto durante questi cinque anni, per la sua costante presenza, per il suo sostegno e per l'incondizionato e meraviglioso rapporto di amicizia che abbiamo costruito. Voglio ringraziare i miei colleghi Leonardo, Claudia, Francesco ed Eleonora con cui ho condiviso 5 anni pieni di studio intenso, notti insonni ma anche tante soddisfazioni, e senza la quale nulla sarebbe stato uguale.

Ringrazio le mie amiche di sempre: Francesca, Francesca, Sofia, Eliana e Cristina per essermi sempre state vicine in qualsiasi momento della mia vita, nonostante la distanza che ci separava e per avermi fatto vivere il vero valore dell'amicizia, della lealtà e della sincerità.

Ringrazio i miei nonni, i miei zie, i miei cugini, le mie cognatine e tutte le persone che hanno creduto in me. Ringrazio ogni singola persona che in questi anni ho incontrato e mi ha regalato un sorriso. Ringrazio Francesco per aver trasformato le montagne della mia vita in pianure con un abbraccio.

Ringrazio Torino per essere stata la mia casa.

Ringrazio Parigi per avermi regalato un nuova visione del mondo e tantissime amicizie che per sempre porterò nel cuore.

INDEX